PONTIFÍCIA UNIVERSIDADE CATÓLICA
DO RIO DE JANEIRO

Henrique Von Pressentin Hollauer

Magnetic and photoluminescence studies of coordination compounds containing carboxylato and/or N-donor ligands complexed to transition or lanthanide metal ions

Dissertação de Mestrado

This dissertation was Presented to the Programa de Pós-graduação em Química of PUC-Rio in partial fulfillment of the requirements for the degree of Mestre em Química.

Advisor: Dr. Livia Batista Lopes Escobar

Rio de Janeiro,
August 2024

PONTIFÍCIA UNIVERSIDADE CATÓLICA
DO RIO DE JANEIRO

Henrique Von Pressentin Hollauer

Magnetic and photoluminescence studies of coordination compounds containing carboxylato and/or N-donor ligands complexed to transition or lanthanide metal ions

Dissertação de Mestrado

This dissertation was Presented to the Programa de Pós-graduação em Química of PUC-Rio in partial fulfillment of the requirements for the degree of Mestre em Química.

Advisor: **Dr. Livia Batista Lopes Escobar**
Departamento de Química – PUC-Rio

Dr. Nicolás Adrián Rey
Departamento de Química – PUC-Rio

Dr. Ricardo Queiroz Aucélio
Departamento de Química – PUC-Rio

Dr. Rafael Alves Allão Cassaro
Departamento de Química Inorgânica– UFRJ

Rio de Janeiro,
August 21st, 2024

Henrique Von Pressentin Hollauer

Graduated in Chemistry at the Universidade Federal Fluminense (UFF) in 2021. Interested in the field of magnetism. Received CAPES scholarship from 2023 to 2024.

Bibliographic data

Hollauer, Henrique Von Pressentin

Magnetic and photoluminescence studies of coordination compounds containing carboxylato and/or N-donor ligands complexed to transition or lanthanide metal ions / Henrique Von Pressentin Hollauer ; advisor: Livia Batista Lopes Escobar. – 2024.
159 f. : il. color. ; 30 cm

Dissertação (mestrado)–Pontifícia Universidade Católica do Rio de Janeiro, Departamento de Química, 2024.
Inclui bibliografia

1. Química – Teses. 2. Polímeros. 3. Magnetismo molecular. 4. Complexos. 5. Fotoluminescência. I. Escobar, Livia Batista Lopes. II. Pontifícia Universidade Católica do Rio de Janeiro. Departamento de Química. III. Título.

CDD: 540

Acknowledgments

Firstly, I would like to thank my entire family for giving me the foundation to complete this work: my mother Sheila and my father Eduardo, both doctors in Chemistry who guided me into this area by showing me the beauties and wonders of science and my brother Leonardo for the many years of companionship and friendship.

To all my friends involved in many different periods of my life. Those who grew up in the same condominium as me are still some of my closest friends even after almost 19 years. To my companions at the school where I spent most of my life, many of whom are still in contact. To all of those, I became friends with at UFF, who have always helped me through all the struggles and have always been part of the many happy moments over these 4 years. And at least all my friends at PUC-Rio who have been part of the last two years have contributed to this project in ways they can't even imagine.

I am grateful to the many professors I have encountered through this journey, but especially to my advisor, Livia, who has helped me understand an entirely new world of molecular magnetism since day one and has always trusted me to not only conduct this project but also help with the day-to-day life in the laboratory with scientific initiation students.

Finally, I would like to thank all the collaborators that made this project possible, Stephane, Ghivelder, Henrique e Alberto for magnetic measurement and interpretation, Guilherme, Sônia, Adriano, Jörg and Renata for single and polycrystalline X-ray diffraction measurements, Bruno, Renan and Sidney for the photoluminescent studies and both Gabriel and Georges that were graduation students that helped me in the synthesis processes. Finally, the institutions, PUC-

Rio, FAPERJ, CNPq, and CAPES, who made this project possible by providing workspace and financing.

This study was financed in part by the Coordenação de Aperfeiçoamento de Pessoal de Nível Superior - Brasil (CAPES) - Finance Code 001.

Abstract

Hollauer, Henrique Von Pressentin; Escobar, Lívia Lopes Batista (Advisor). **Magnetic and photoluminescence studies of coordination compounds containing carboxylato and/or N-donor ligands complexed to transition or lanthanide metal ions**. Rio de Janeiro, 2024. 159 p. Dissertação de Mestrado – Departamento de Química, Pontifícia Universidade Católica do Rio de Janeiro

Molecular magnetism has created a lot of interest due to its possible application in components of electronic materials. These types of materials can be created through coordination compounds such as coordination polymers, which have the capacity to be multifunctional materials. In this work, we synthesized a total of 11 new complexes organized in two systems that differ according to the composition of materials. The first system utilized the mixture of polycarboxylate ligand BTB and N-donor ligand such as phen and dmdpy to evaluate the influence of these auxiliary ligands in the complexes structure and properties. The family utilizing phen as auxiliary ligand generated two isomorph 1D coordination polymers with Cu^{2+} and Co^{2+} as metal ions. EPR measurements for Cu^{2+} polymer showed almost no magnetic interactions between metal ions. Due to both CPs being isomorph, the same small magnetic interactions were expected for Co^{2+} CP, which is an indicative of possible magnetic molecule behavior due to cobalt strong ZFS. Out-of-Phase magnetic susceptibility measurement showed the nanomagnet behavior. A relaxation time of $\tau_0 = 5.52(4) \times 10^{-7}$ s and energy barrier of 12.1(3) K were determined for this complex. The change of N-donor ligand from phen to dmdpy resulted in a pentacoordinated Cu^{2+} dimer, however, since the divergent ligand for both families was the same, the small interaction between the copper(II) ions was obtained, as evidenced by EPR and magnetization measurements.

The second system presents Ln^{3+} ions with Coumarin-3-carboxylic acid as the organic ligand, where two different families were obtained by changing the proportion of Ln ions and ligand. First family 1D CP were obtained with both components with the same proportion. Magnetocaloric studies were conducted for the Gd^{3+} and the obtained ΔS_M^{Max} value was smaller than the expected value. For the Tb^{3+} and Dy^{3+} CPs displayed potential as nanomagnets due to the signal obtained in dynamic magnetic measurements. Photoluminescent studies for Eu^{3+} and Tb^{3+} CPs were conducted, where 0.30 ± 0.05 ms and 0.13 0.05 ms emission lifetime was estimated. The second family obtained had a Ln^{3+} and 3-HCCA proportion of 1:3, and resulted in a 1D coordination polymer, where the extension of the polymeric chain had the same mechanism. Photoluminescent studies for Eu^{3+} and Tb^{3+} CPs were conducted, where an increase in the emission lifetime from 0.30 ± 0.05 ms to 0.45 0.05 ms for Eu^{3+} derivate was observed due to the removal of one H_2O molecule coordinated to the europium ion.

This work resulted, at the time of this dissertation, in the publication of two scientific papers, as well as a submitted paper that is currently under review.

Keywords

Coordination polymers, magnetic properties, lanthanides, polycarboxylates, auxiliary ligands

Resumo

Hollauer, Henrique Von Pressentin; Escobar, Lívia Lopes Batista (Orientador). **Estudos magnéticos e fotoluminescentes de compostos de coordenação contendo ligantes carboxilato e/ou doadores nitrogenados complexados a íons metálicos de transição ou lantanídeos**. Rio de Janeiro, 2024. 159 p. Dissertação de Mestrado – Departamento de Química, Pontifícia Universidade Católica do Rio de Janeiro

O magnetismo molecular tem despertado muito interesse devido a possível aplicação em componentes de materiais eletrônicos. Esses tipos de materiais podem ser criados através de compostos de coordenação, como os polímeros de coordenação, que têm a capacidade de serem materiais multifuncionais. Neste trabalho foram sintetizados 11 compostos inéditos, divididos em dois sistemas que diferem conforme a composição dos materiais. O primeiro sistema utilizou a mistura do ligante policarboxilato BTB e do ligante N-doador como phen e dmdpy para avaliar a influência desses ligantes auxiliares na estrutura e propriedades dos complexos. A família que utiliza fen como ligante auxiliar gerou dois polímeros de coordenação isomorfos 1D com Cu^{2+} e Co^{2+} como íons metálicos. Medições de EPR para o polímero Cu^{2+} não mostraram quase nenhuma interação magnética entre íons metálicos. Devido ao fato de ambos os CPs serem isomorfos, as mesmas pequenas interações magnéticas eram esperadas para o Co^{2+} CP, o que é um indicativo do possível comportamento da molécula magnética devido ao forte ZFS de cobalto. A medição da suscetibilidade magnética fora de fase mostrou o comportamento do nanoímã. Um tempo de relaxação de $\tau 0 = 5{,}52(4) \times 10^{-7}$s e barreira de energia de 12,1(3) K foram determinados para este complexo. A mudança do ligante doador de N de phen para dmdpy resultou em um dímero de Cu^{2+} pentacoordenado, porém, como o ligante divergente para ambas as famílias era

o mesmo, a pequena interação entre os íons cobre(II) foi obtida, como evidenciado por EPR e magnetização medições.

O segundo sistema apresenta íons Ln^{3+} com ácido cumarínico-3-carboxílico como ligante orgânico, onde duas famílias diferentes foram obtidas alterando a proporção de íons Ln e ligante. A primeira família 1D CP foi obtida com ambos os componentes na mesma proporção. Estudos magnetocalóricos foram realizados para o Gd^{3+} e o valor de ΔS_M^{Max} obtido foi menor que o valor esperado. Para os CPs Tb^{3+} e Dy^{3+} apresentaram potencial como nanoímãs devido ao sinal obtido nas medidas magnéticas dinâmicas. Foram realizados estudos fotoluminescentes para CPs Eu^{3+} e Tb^{3+}, onde foram estimados tempos de vida de emissão de 0,30 ± 0,05 ms e 0,13 ± 0,05 ms. A segunda família obtida apresentou proporção de Ln^{3+} e 3-HCCA de 1:3, e resultou em um polímero de coordenação 1D, onde a extensão da cadeia polimérica teve o mesmo mecanismo. Foram realizados estudos fotoluminescentes para CPs Eu^{3+} e Tb^{3+}, onde foi observado um aumento no tempo de vida da emissão de 0,30 ± 0,05 ms para 0,45 ± 0,05 ms para o derivado Eu^{3+} devido à remoção de uma molécula de H_2O coordenada ao íon európio.

Este trabalho resultou, até o momento desta dissertação, na publicação de dois artigos científicos, além de outro adicional que está em processo de review.

Palavras-chave

Polímeros de coordenação, propriedades magnéticas, lantanídeos, policarboxilatos, ligantes auxiliares

Summary

List of Figures

List of Tables

List of Abbreviations

SMM – Single-Molecule Magnet

SIM – Single-Ion Magnet

SCM – Single-chain Magnet

ZFS – Zero-Field Splitting

***Ac*–** Alternate current

***Dc* –** Direct current

QTM – Quantum tunneling of magnetization

TA-QTM – Thermally-assisted Quantum tunneling of magnetization

EPR – Electron Paramagnetic Resonance

CP – Coordination Polymer

BTB – 1,3,5-tris(4-carboxyphenyl)benzene

3-HCCA – Coumarin-3-Carboxylic acid

Phen – 1,10-Phenanthroline

Dmdpy – 5,5'-dimethyl-2,2'-dipyridyl

MOF – Metal Organic Framework

DMF – Dimethylformamide

1
General Introduction

Developing new technologies has been one of the many catalysts for new research fields in physics and chemistry. In that regard, magnetism is an area that has been interesting to society due to its exciting and unique properties. The use of magnetic materials has been dated back to 206 BC, with recordings found about the use of compass in early China [1]

In modern society, magnetic materials have been used in many different areas, mainly being applied to construct electronic devices. This type of device tends to decrease in size while increasing in efficiency. In that regard, nanotechnology has played a significant role in the development of these materials, such as in hard disk drives, where the memory system is based on magnetic materials and their magnetization orientation.

Coordination compounds, such as coordination polymers, have received significant amount of interest in possible application in electronic devices due to the possibility of engineering the desired properties of the materials with the choice of organic molecules since they directly impact the structure of the compound. For instance, these types of materials can develop the so-called molecular nanomagnets, coordination compounds that have superparamagnetic properties and, at low temperatures, behave as tiny magnets that can be used for magnetic memory systems. Another interesting possibility regarding these coordination compounds is that they can behave as multifunctional materials, displaying magnetic properties and luminescent, conductive, adsorptive, and others [2].

This field related to the synthesis and design of molecular systems for magnetic study is called molecular magnetism. In this section, we will discuss many topics related to these types of materials, ranging from historical markers in this field to the structural, magnetic, and luminescence characteristics observed on this subject.

1.1
Magnetic properties

When a magnetic measurement is made, we are interested in studying the magnetic moment of the sample, called magnetization, in relation to temperature. Considering an isotropic (no preference in magnetization orientation) sample containing 1 mol of a molecular sample in the presence of an external magnetic field, the molar magnetization (M) is given through Eq. 1 [3][4]:

$$\frac{\partial M}{\partial H} = \chi \text{ (Eq. 1)}$$

Where χ is molar magnetic susceptibility, M is a vector related to molar magnetic moment and H is a vector related to the magnetic field applied.

Magnetic susceptibility is the response of a sample under an external magnetic field, and is given by the sum of components related to paramagnetism (χ_p) and diamagnetism (χ_d):

$$\chi = \chi_p + \chi_d \text{ (Eq. 2)}$$

Diamagnetism is related to the presence of paired electrons in a material. Therefore, it is considered a universal property of matter. When a diamagnetic material is under an external magnetic field, it will be repelled since the spin magnetic moment (S) will align contrary to the applied magnetic field. However,

the presence of unpaired electrons in a material creates different magnetic properties (despite still presenting diamagnetism due to its pair electrons). The presence of unpaired electrons is called paramagnetism. When a paramagnetic material is under an external magnetic field, it will be attracted to it since its spin magnetic moment will align towards the applied field. Paramagnetic behavior is observed only in the presence of a magnetic field (but it is usually dependent of the magnetic field's intensity) and is temperature-related since there is a competition between the tendency of randomizing spins due to thermal agitation and the alignment of spins with the magnetic field applied. Paramagnetic susceptibility magnitude is given by Curie law [3][4](Eq. 3):

$$\chi_p = \frac{N\mu_b^2 g^2}{3k_b T} S(S+1) = \frac{C}{T} \text{ (Eq. 3)}$$

$$\chi_p = 0.125 g^2 \frac{S(S+1)}{T} = \frac{C}{T}$$

Where N = Avogadro's number, g = Landé's fator, μ_b = Bohr's magneton, S = Spin magnetic moment, k_b = Boltzmann's constant, T = Temperature and C = Curie's constant.

Both diamagnetic and paramagnetic properties are characteristic of single atoms. However, when paramagnetic atoms are close enough, they start interacting with themselves, creating a cooperative effect and producing new properties. These properties are ferromagnetism and antiferromagnetism. Ferromagnetism is when the interactions between the magnetic dipoles of close atoms point in the same direction, forming a parallel alignment. This alignment occurs only below a critical temperature called Curie's Temperature (T_C), and above T_C, its susceptibility will obey Curie-Weiss (Eq. 4). Antiferromagnetism occurs when magnetic dipoles with the same intensity form an antiparallel alignment, resulting in a null resultant vector. The critical temperature where the

sample goes from antiferromagnet to paramagnet is called Néel's Temperature (T_N). An extension of ferromagnetism is ferrimagnetism; this happens when the antiparallel vector does not have the same magnitude (in the case of systems with a block d metal with a lanthanide, for example). Therefore, these vectors do not cancel each other, resulting in an arrangement like ferromagnetism. These interactions are well represented in Figure 1.

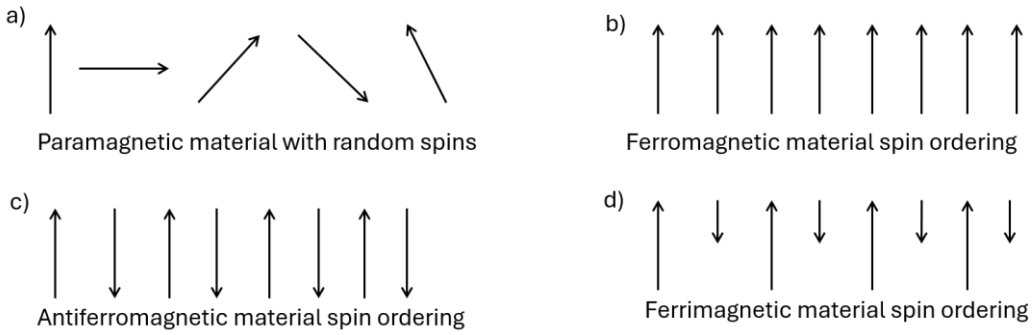

Figure 1: Schematic illustration of spin interactions for several magnetic behaviors (adapted from [5]).

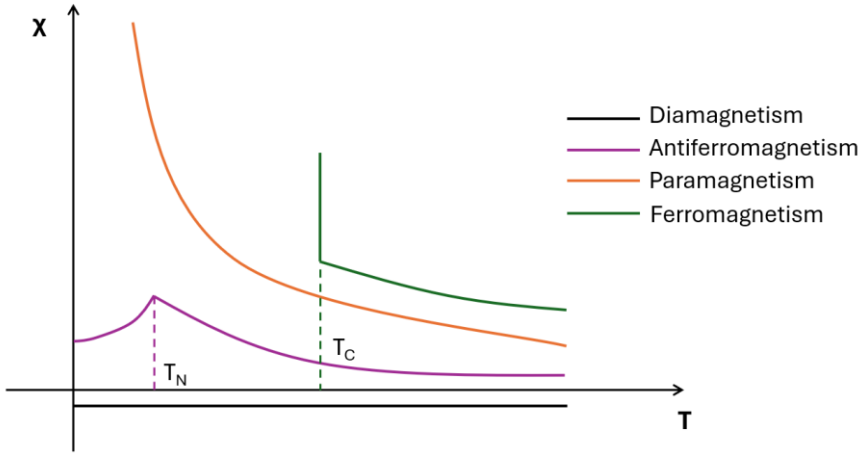

Figure 2: Magnetic behavior as a function of temperature (adapted from [6]).

Magnetic behavior can be analyzed applying Curie-Weiss law (Eq. 4)

$$\chi_{CW} = \frac{C}{(T-\theta)} \quad \text{(Eq. 4)}$$

Curie-Weiss law can also be rewritten as:

$$\chi_{CW} = \frac{N\mu_B^2 g^2 S(S+1)}{(3K_B T - zJS(S+1))} \text{ (Eq. 5)}$$

J is the coupling constant of the two closest magnetic species, and z is the number of close species around a given magnetic molecule in the crystal lattice. A common convention is that a positive value of J characterizes an intermolecular ferromagnetic interaction, and a negative value of J characterizes an intermolecular antiferromagnetic interaction.

θ is called the Weiss constant. We can identify the presence of ferromagnetic and antiferromagnetic interactions through the inverse of χ vs T. If the system obeys the Curie-Weiss law, a straight line with a slope of C^{-1} is formed, and the intercession with the temperature axis is used to estimate the value of θ. If θ is positive, ferromagnetic behavior is present, and if θ is negative, antiferromagnetic interactions are present (Fig. 3).

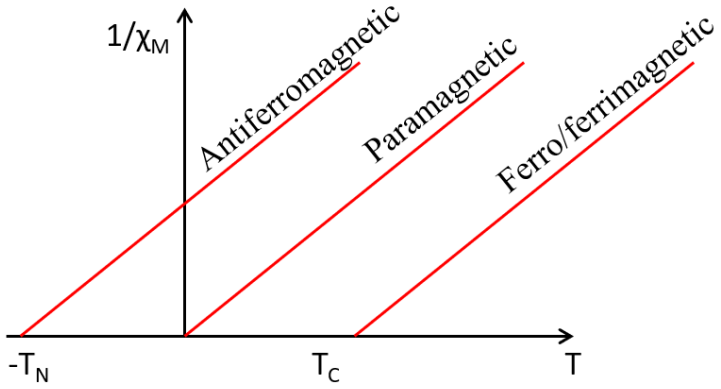

Figure 3: χ^{-1} versus T for a sample that obeys Curie and Curie-Weiss law.

Magnetic interactions can also be related to the structure of a compound (angles and bond distances) since the type of coupling can be predicted through the overlap of magnetic orbitals (Figure 4). A strong orbital overlap contains an angle between orbitals bigger than 90°, and this type of overlap favors antiferromagnetic interactions. If the overlap is orthogonal, it favors ferromagnetic interactions.

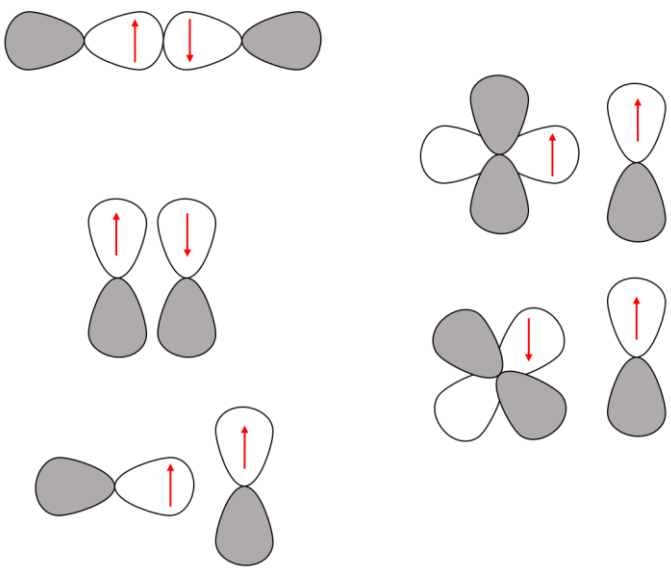

Figure 4: Magnetic orbital overlapping.

1.1.1

Molecular nanomagnets

Molecular nanomagnets are a recent class of materials that have received great interest in magnetic studies due to their unique property of slow magnetization relaxation. The first ever molecular nanomagnet was synthesized in 1980 when Lis obtained a dodecanuclear manganese cluster containing Mn^{3+} and Mn^{4+} with the formula $[Mn_{12}O_{12}(CH_3COO)_{16}(H_2O)_4].4H_2O.2CH_3COOH$ (Fig. 5). In the original paper, there was no interpretation of magnetic properties; that only came in 1993 , where it was reported that the relaxation time of magnetization followed an exponential law (Eq. 6), where at 2K, the relaxation time becomes the order of a few months, and at 1.5K, at the order of 50 years [7][8].

$$\tau = \tau_0 \exp\left(\Delta/_{kT}\right)$$ (Eq. 6), where Δ = energy barrier

This study showed that a single molecule could become and behave like a tiny magnet, and the term Single-Molecule Magnet was suggested [9]. This term was later applied to varied materials. When the structure that behaves as a

nanomagnet contains only one metal ion, it is called a Single Ion Magnet [10], and when an entire chain behaves like a magnet with small magnetic interactions between different chains, the material is called Single Chain Magnet [11].

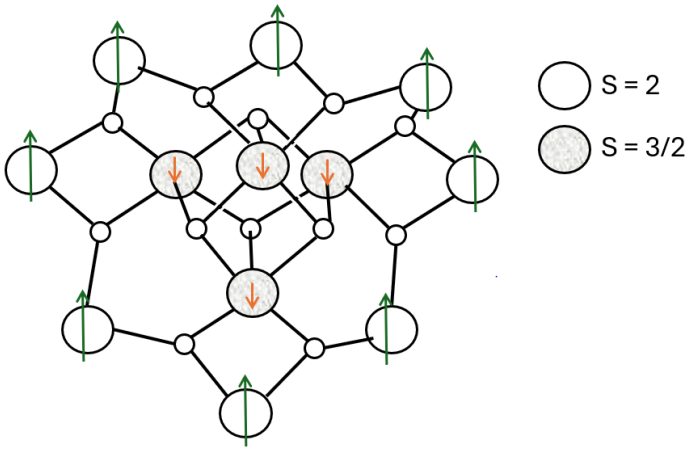

Figure 5: Sketch of the structure of $Mn_{12}Ac$ (adapted from [8]).

Single-molecule magnets and structures alike present magnetic anisotropy. This phenomenon is described as a preferential orientation of the magnetization, which originates from symmetry distortions (such as octahedral distortion) and the Zero-Field Splitting effect (ZFS). ZFS happens due to the interactions between unparallel electrons and spin-orbit coupling present in the sample and is exclusive to systems with a spin magnetic moment $S \geq 1$.

To be classified as SMM, the compound must be magnetic bistable and present an energy barrier for the magnetic spin reversal, resulting in a slow relaxation of magnetization. This can be explained through a double pit diagram, as shown in Figure 6. The value of the energy barrier is given as $U_{eff}=S^2|D|$, where S is the magnetic spin moment and D is the ZFS representation. It can either be a negative or positive value.

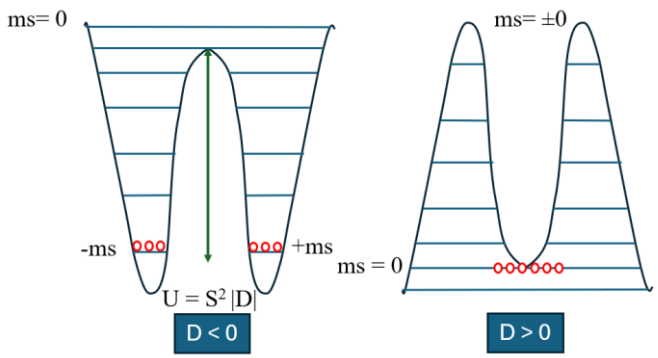

Figure 6: Double pit potential energy diagram, where both pits represent the lowest m_s energy states. U = energy barrier, S = spin magnetic moment, and D = ZFS parameter (adapted from [12]**).**

As discussed previously, SMMs behave like tiny, isolated magnets. This property is like the magnetic behavior of superparamagnetic nanoparticles, which is associated with the formation of monodomains. Domains are regions of a ferromagnetic substance that, when demagnetized, have their magnetic moment, as represented in Figure 7, where the separation of different domains is called Bloch wall.

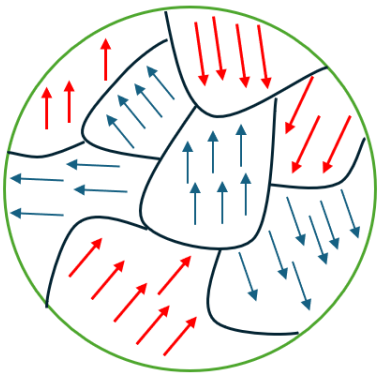

Figure 7: Representation of magnetic domains and the Bloch walls (adapted from [13]).

With the reduction of particle size, the multidomain state of the matter reduces until it reaches a single domain, followed by the state of superparamagnetism. In this state, particles are extremely sensitive to thermal fluctuation, and their magnetic moment changes rapidly if their volume are small

enough so the energy barrier for magnetic reversal is smaller than k_BT (k_B = Boltzman constant, T = Temperature), resulting in hysteresis loss. As the Superparamagnetic behavior depends on temperature, when a SMM system's temperature is lowered enough, it will reach a point where the magnetic moments will be blocked due to the energy barrier caused by anisotropy, acquiring slow relaxation of magnetization [3].

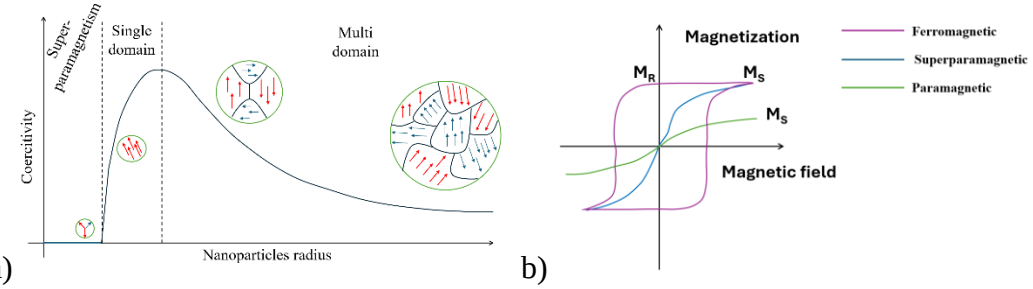

a) b)

Figure 8: a) Coercitivity related to the reduction of nanoparticle sizes leading to monodomain and superparamagnetism (adapted from [14]). b) Magnetic hysteresis of different types of magnetism (adapted from [15]).

Molecular nanomagnets exhibit properties such as slow relaxation of magnetization. AC magnetic susceptibility studies are needed to analyze these characteristics.

In *ac* magnetic susceptibility experiments, an oscillating magnetic field is applied, and this field has an angular frequency ω. At high temperatures and low frequencies, the magnetic moment of the material can follow the magnetic field due to its high internal energy. However, when temperature decreases and frequency increases, the magnetic moments of the sample cannot follow the external field, and its magnetization fades according to the equation below.

$$M(t) = H_{ac}(\chi' \cos(\omega t) + \chi'' \sin(\omega t)) \quad \text{(Eq. 7)}$$

Where χ' represents the real or in-phase component, that is, the magnetic moments that can follow the external field, and χ'' represents the imaginary or out-of-phase components, that is, those moments detected at a 90° angle from the

applied external field. The total *ac* susceptibility can be written as Eq 8., with each individual term being described as shown in Eq 9:

$$\chi = \chi' + \chi'' \text{ (Eq. 8)}$$

$$\chi' = \left(\frac{M_{ac}}{H_{ac}}\right)\cos(\omega) \text{ and } \chi'' = \left(\frac{M_{ac}}{H_{ac}}\right)\sin(\omega) \text{ (Eq. 9)}$$

Since the *ac* susceptibility depends on the frequency of the external field applied, in the limits such as $\omega \rightarrow 0$ and $\omega \rightarrow \infty$, *ac* susceptibility is called isotherm (χ_T) and adiabatic(χ_S). When applying these limits, *ac* susceptibility can be rewritten as:

$$\chi = \chi_S + \frac{\chi_T + \chi_S}{1 + i\omega\tau} \text{ (Eq. 10)}$$

The slow relaxation of the magnetization manifests itself as signals of both in-phase and out-of-phase magnetic susceptibility components that depend on the frequency of the applied oscillating magnetic field. In real systems, a relaxation time distribution will always exist, meaning Eq. 10 can be rewritten by generalizing Debye's model:

$$\chi = \chi_S + \frac{(\chi_T - \chi_S)}{1 + (i\omega\tau)^{1-\alpha}} \text{ (Eq. 11)}$$

The α phenomenological parameter introduced is obtained through a Cole-Cole plot, that is χ,'' vs χ' maximum values for a specific frequency at a fixed temperature. A small α value is expected for SMM behavior since higher α values indicate wide distribution of relaxation times.

χ'' maximum peaks correspond to a temperature in which ω in the oscillating magnetic field equals the spin reversal rate ($1/\tau$). Therefore, this experiment gives kinetic data, and a graph based on Arrhenius law ($\tau = \tau_0 \exp(^{\Delta E}/_{k_B T})$ can be constructed. In a thermally activated process of a single

energy barrier, a graph of ln (1/τ) vs. (1/T) must be linear according to the following equation, where τ_0 is related to the relaxation rate.

$$\frac{1}{\tau} = \frac{1}{\tau_0} exp^{\left(-Ueff/k_BT\right)} \quad \text{(Eq. 12)}$$

The relaxation process can happen through several different mechanisms and are diverse, complex, and extremely sensitive to numerous factors such as temperature, magnetic field, and intermolecular interactions [16]. Magnetic moment relaxation can be separated into two categories: those that occur through Spin-phonon couplings, such as Orbach, Raman, and direct processes, and those that occur through the quantum nature of the objects, such as Quantum Tunnelling (QTM) and Thermally Assisted (TA-QTM) (Fig. 9.)

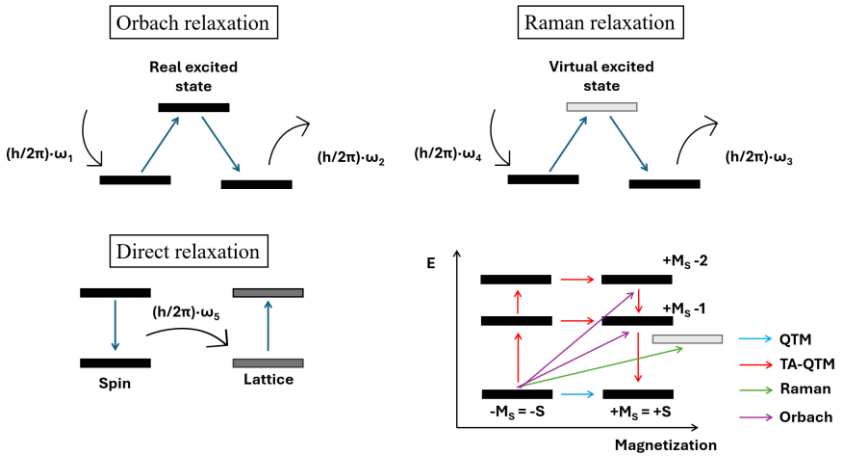

Figure 9: Representation of the most common relaxations of the magnetization processes (adapted from [16]).

Orbach relaxation occurs when the system absorbs phonons from the crystal network to the higher excited sublevel (M_S= 0) and then relaxes to either of the ground M_S = ± S, emitting new phonons. However, this process demands thermal assistance and for cobalt-based systems is not present with energy barriers lower than 150 cm^{-1} [17]. Raman relaxation has a similar process to Orbach's; however, when a photon is absorbed, it goes to a virtual excited state, releasing another

phonon and relaxing to a ground $M_S = \pm S$ state. Direct relaxation is when a single phonon directly emits a phonon with the energy difference of the $\pm M_S$ sublevels in the ground state.

Few phonons are available at low temperatures for the spin to jump over the potential barrier. In these conditions, the phenomenon related to the quantum nature of the materials is more predominant. Quantum mechanics tell us that a particle in symmetric double potential (analogous to Fig. 6) undergoes tunnel effect, called quantum tunneling. This means that if a particle is put into an MS = - S state, it goes to an $M_S = + S$ state if the ground energy of both ground states has similar energy [18]. If both energy levels associated with this spin switch are not at the ground level, the relaxation process is called TA-QTM.

1.1.2

Electron paramagnetic resonance

Electron paramagnetic resonance (EPR) is a technique discovered in 1944 by the Russian physicist Zavoisky and is widely used for magnetic research. Based on the principle that an electron put through an external magnetic field loses its energy levels degeneracy, splitting in two due to the so-called Zeeman Effect. The value of this loss of degeneracy is described through Eq. 12, where μ_b = Bohr's magneton, g_e = g-factor for the free electron (2.00), and H = magnetic field applied [19].

$$\Delta E = g_e \mu_b H \quad \text{(Eq. 12)}$$

The standard in EPR studies is to fix the radiation source is in the gigahertz range (GHz), which lies in the microwave region, and vary the magnetic field intensity. When the energy gap caused by the degeneracy from Zeeman effect reaches the same value as the microwave radiation emitted, an

absorption signal is obtained. This radiation absorption is called the H_{res} resonance field (Fig 10). The EPR signal form is usually described with a Lorentzian or Gaussian function that can be calculated as a function of the resonance field and signal width.

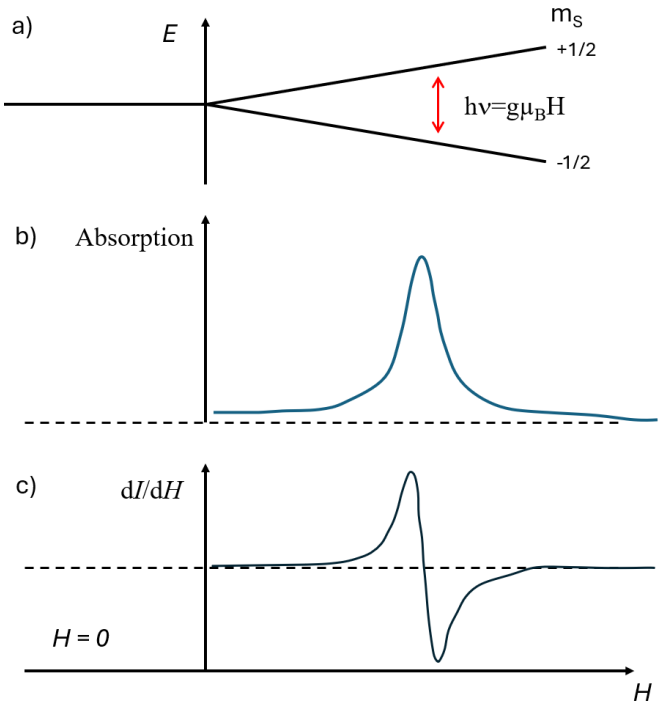

Figure 10: a) Energy levels for a free electron with an applied magnetic field; b) Absorption sign; c) First derivative of an EPR signal. (adapted from [20])

When an electron is placed in a molecule, its angular momentum changes due to the added orbital angular momentum. This effect, called Spin-Orbit interaction, changes the energy gap value.

Since μB is a constant, the H value can be measured, the g-factor value is one of the parameters that can be obtained with this measurement, which gives important information on the sample structure. The deviation on the measured *g*-factor is anisotropic due to the orientation of the orbitals in the molecule. There is a principal axis system for every paramagnetic molecule, and the g-factors measured along this axis can present different values and are labeled gx, gy, and g_z [21].

Different classes emerge due to the relation between the different g-factor values. Fig. 11 demonstrates these different classes and their respective EPR signals. When all g -factors have the same value, an Isotropic system is present, and only a signal is observed. The axial class happens when one value differs from the other ($g_z \neq g_x$ and g_y), and two signals are present in EPR measurements. The last scenario is when all g-factor values are different. This is called a Rhombic class, and it presents three different signals.

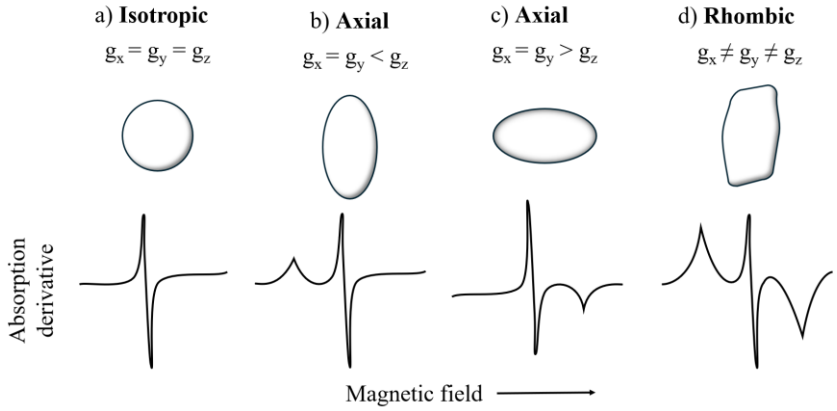

Figure 11: Schematic representation of *g* tensor and the consequential EPR spectra [21].

1.1.3

Magnetocaloric effect

The magnetocaloric effect, discovered in 1881 by Walburg, is based on the heat exchange of the magnetic sample with its surroundings when put through an external magnetic field. This process can be either adiabatic or isothermal. When it's an adiabatic process, the magnetic material changes its temperature; however, when it's isothermal, the sample exchanges heat with a thermal reservoir [22].

The total entropy of the magnetic material is the sum of three contributions related to the solid's lattice, electronic system and magnetic part. When applying an external magnetic field, the entropy's magnetic and electronic parts decrease;

therefore, the lattice entropy must increase to counter-react this effect. However, a higher lattice entropy contribution (lattice vibrations) equals a higher material temperature. Therefore, an increase in the magnetic field results in an increase in temperature, and a decrease in the magnetic field results in a cooling process, which makes this type of material a great candidate for cooling mechanisms [23].

This effect is therefore monitored by measuring the magnetic entropy change $\Delta S = \Delta Q/T$ (ΔQ = heat exchange with the environment). However, the adiabatic temperature change ΔT characterizes the effect when the adiabatic process is considered. One way to obtain the magnetic entropy change is to measure magnetization as a function of magnetic field and temperature, M (H,T), and apply the data to the equation below [22].

$$\Delta S_M(T, \Delta S) = \int_0^{H'} \left(\frac{\partial M}{\partial T}\right)_H dH \text{ (Eq. 13)}$$

$$\Delta S_M \approx \frac{1}{\Delta T}\left[\int_0^{H'} M(T + \Delta T, H)dH - \int_0^{H'} M(T, H)dH\right] \text{ (Eq. 14)}$$

An ideal MCE material should have a negligible magnetic hysteresis to avoid work losses due to rotating domains in the process, thus maximizing the change in temperature [24]. In conventional magnetocaloric materials, materials containing elements with large atomic moments are used to maximize the ΔS_M [25]. Uniting both characteristics, Gadolinium-based materials are excellent for this application due to their having a $4f^7$ configuration, which not only gives a great magnetization signal, but its half-filled configuration exhibits a spherically symmetric charge density, giving no magnetic anisotropy, resulting then in thin hysteresis loop [26].

1.2

Phenomena of Photoluminescence

Eilhard Wiedemann first introduced the term luminescence in 1888, referring to all light phenomena not conditioned by the rise in temperature. Nowadays, the most accepted definition of luminescence is the emission of light that occurs when an entity (atom or molecule) goes from an electronically excited state to a ground state [27].

G.G. Stokes's pioneer studies in the middle of the 19th century formed the basis of spectroscopy. The concept of light emission was introduced, and the process of luminescence was divided into two categories depending on the nature of the excited state—fluorescence and phosphorescence [27].

Fluorescence is when the transition involves a singlet excited state. In this singlet state the electron is paired by opposite spin to the second electron in the ground state, therefore the return is spin allowed and occurs rapidly. On the other hand, phosphorescence is the emission of light from the triplet excited state, where the electron has the same spin orientation as the ground state electron, causing the return to be forbidden, resulting in a slow emission rate. This characteristic is portrayed in day-to-day objects that “glow in the dark”. After being exposed to light, these objects can glow for long periods due to the slow return rate [28].

These light absorption and emission processes can be well visualized by the Jablonski diagram (Figure 12), considered the father of fluorescence spectroscopy. The diagram shows the singlet ground, first and second excited energy states represented as S_0, S_1, and S_2, respectively, and the triplet energy state depicted as T_1. Some subdivisions in each energy state are the vibrational energy levels. In Figure 12, a few possible interactions were excluded to focus on the main transitions in fluorescence studies.

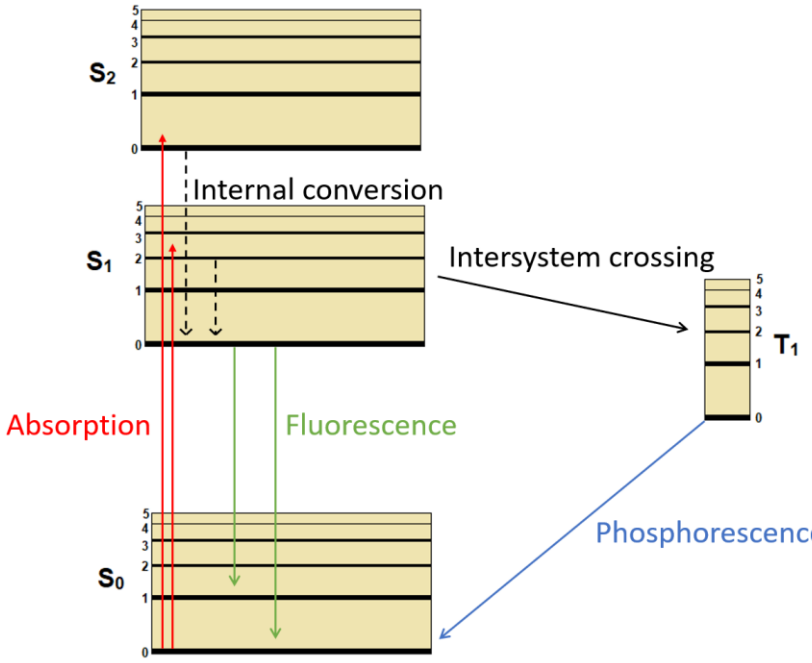

Figure 12: Simplified representation of the Jablonski diagram [28].

Absorption and emission typically occur through the lowest vibration energy levels of the molecule due to an effect called internal conversion. Within 10^{-12} s, the fluorophore relaxes to the ground vibration energy state, releasing heat to the environment.

Following energy absorption, the electron goes from ground S_0 to the excited state S1, and various processes can happen. Firstly, the electron can return to the ground S_0 state, emitting light through the process previously described as fluorescence. Another alternative is the relaxation process to a high vibrational state of S_0 without the light emission, where the energy is dissipated through heat (Internal conversion). The molecules can also undergo a spin conversation to the first triplet state T_1, a phenomenon called Intersystem Crossing. From the T_1 state, another Intersystem Crossing can occur back to the S_0 state, resulting in phosphorescence. This transition is of lower energy; therefore, phosphorescence emission is shifted to longer wavelengths than fluorescence.

Fluorescence spectroscopy is a topic of much research that has grown remarkably in the last twenty years due to its immense applications in different fields, such as biotechnology, medical diagnostics, and forensics [28].

1.3

General concepts of lanthanides

Lanthanides are 15 elements with atomic numbers between 57 and 71 and are part of a slightly bigger group of rare earths, which also contain scandium and yttrium.

Lanthanide ions have only been discovered entirely around 1907 due to the difficulty of separating and obtaining these elements with high purity. This happens because, in a general way, they possess very similar chemical and physical properties, greatly in part due to the graduate reduction of the ionic radius with the gradual filling of 4*f* orbital, a phenomenon called “lanthanide contraction”. Typical examples of this similarity of properties include the constant trivalent oxidation state, various examples of isomorphism, and the predominant formation of ionic compounds with high affinity for hard Pearson ligands [29].

The electronic distribution of lanthanides in their fundamental state assumes the form of [Xe] $4f^{n}\,5d^{0}\,6s^{2}$, except for La, Ce, Gd, and Lu, which assumes a configuration of [Xe] 4f n-1 5d 1 6s2. The most common oxidation state found is +3, where the loss of electrons occurs in $4f^{n}$ and $6s^{2}$ for all except La, Ce, Gd, and Lu since the loss occurs for the $5d^{1}$ and $6s^{2}$ orbitals.

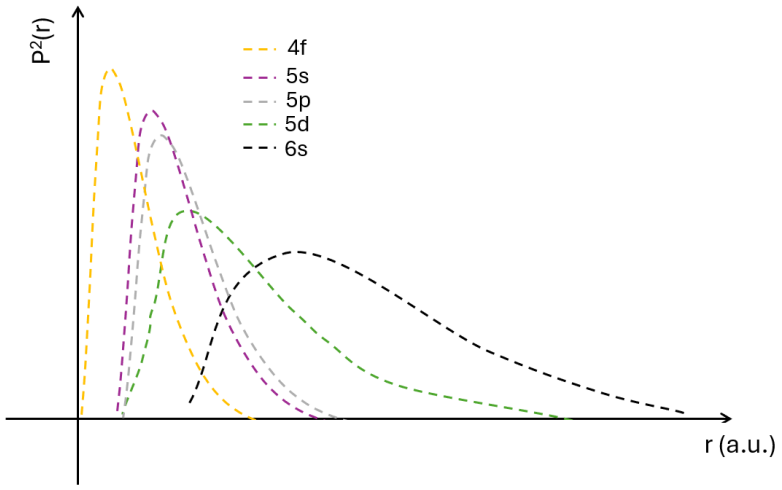

Figure 13: Radial distribution function for Gadolinium (adapted from [30]**).**

The fact that the 5s and 5p orbitals are filled to protect the 4f orbitals (Fig. 13) causes the ion's behavior to be like a free Ln^{III} since the coordination environment does not have a big influence on the lanthanide's properties, a behavior different from that of the block d transition metals. This gives the lanthanides unique magnetic and spectroscopy properties, which have received great interest in developing Ln-based materials.

1.3.1

Magnetic properties of the lanthanides

All but La^{3+} and Lu^{3+} rare earth elements have unparalleled electrons and possess a non-zero magnetic moment. The unparallel electrons spin in the 4*f* orbitals, present a strong spin-orbit coupling, but weakly interact with the ligand ambient. Two consequences emerge. First, the magnetic properties depend almost exclusively on the fundamental state since the excited states are thermally inaccessible. Second, magnetic characteristics are close to those predicted for the free ion since they are independent of the chemical ambiance [29].

Lanthanide-based complexes' magnetic responses are commonly difficult to interpret due to the deviation from Curie's law caused by the depopulation of the energy sublevels at lower temperatures. Therefore, a deep analysis of their electronic structures is needed to understand their magnetic properties better. Figure 14 shows the main factors that influence the energy levels of a free Ln^{III} ion, where the first observed break of degeneracy is the interelectronic repulsion, resulting in a ^{2S+1}L ground state term.

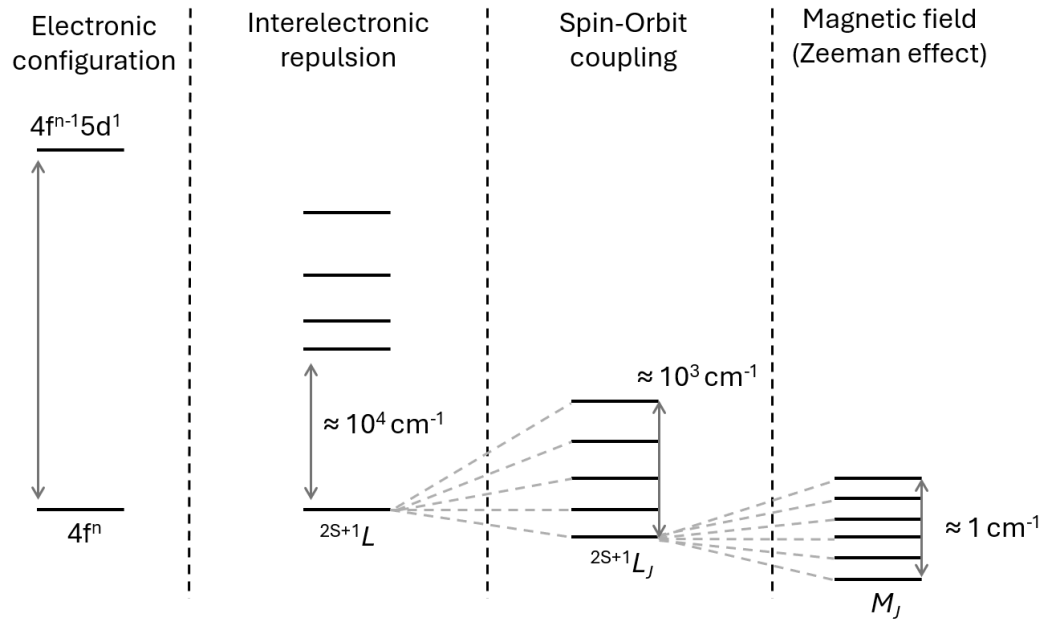

Figure 14: The effect of interelectronic repulsion, Spin-Orbit coupling and Zeeman effect (H = 1T) for a $4f^n$ of a free Ln(III) ion (adapted from [31]).

Spin-orbit coupling is a strong factor in lanthanides-based materials. It is usually represented as $\lambda \boldsymbol{L}.\boldsymbol{S}$, where λ is an energy unit, **L** is the total orbital angular momentum, and **S** is spin momentum. It is also related to a parameter of spin-orbit coupling ζ through the equation $\lambda = \pm {}^{\zeta}/_{2S}$, where the positive sign is used for an electronic shell half full ($n < 7$ for lanthanides, n being the number of electrons) and a negative sign is used for a more than half full orbital ($n > 7$) [3].

Spin-orbit coupling splits the ground term ^{2S+1}L into $^{2S+1}L_J$ multiplets that have the same L, S but with different values of J in a way that the fundamental state is J = L – S in a case of a half-full orbital and J = L + S in a more than half full orbital.

The remaining $^{2S+1}L_J$ degeneracy can then be split by Zeeman effect into 2J+1 components represented by the term M_J, where its value varies by an integer value from -J to +J. In that regard, Landé's factor can be described in terms of J, L, and S, as shows the equation below:

$$g_J = \frac{3}{2} + \frac{S(S+1)-L(L+1)}{2J(J+1)} \quad \text{(Eq. 15)}$$

With that, the magnetic susceptibility of the the free Ln(III) ions will follow Curie's law:

$$\chi_M = \frac{N_A g_J^2 \mu_B^2}{3kT} J(J+1) \quad \text{(Eq. 16)}$$

The values of g_J and χT calculated from Eq X for various rare earths ions are shown in Table 1.

Table 1: Values of gJ and χT for Rare Earth Ions in the Free-ion approximation [3].

Ion	Configuration $4f^n$, n=	g_J	$\chi_M T$ (cm^3Kmol^{-1})
Ce(III)	1	6/7	0.80
Pr(III)	2	4/5	1.60
Nd(III)	3	8/11	1.64
Pm(III)	4	3/5	0.90
Sm(III)	5	2/7	0.09
Eu(III), Sm(II)	6	5	0.00
Gd(III), Eu(II)	7	2	7.88
Tb(III)	8	3/2	11.82
Dy(III)	9	4/3	14.17
Ho(III)	10	5/4	14.07
Er(III)	11	6/5	11.48
Tm(III)	12	7/6	7.15
Yb(III)	13	8/7	2.57

Even though the ligands have a small influence in lanthanide-based complexes, it is not completely negligible, as the Stark effect shows. This effect is the interaction of non-spheric symmetry ligands with $4f^n$ orbitals, which results in a break of degeneracy of the $^{2S+1}L_J$ state, resulting in the origin of the so-called Stark sublevels (Figure 15).

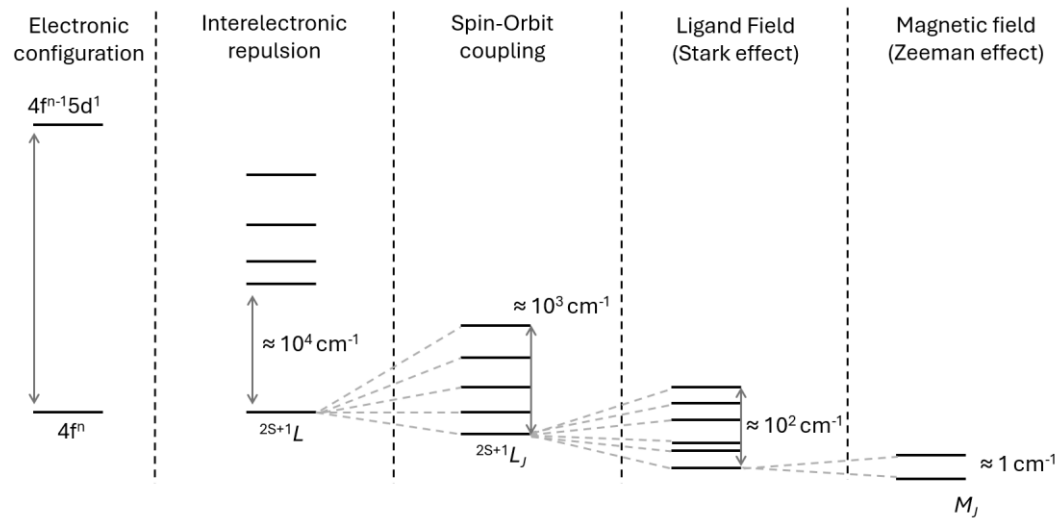

Figure 15: Energetic structure of a Kramers ion (half-integer spin) in a ligand field (Stark effect) (adapted from [31]).

1.3.2

Spectroscopic properties of the lanthanides

The *f-f* transition for lanthanide ions is prohibited, resulting in low absorption spectra and luminescence intensity. In 1942, Weissman studied the energy transition in Eu^{3+} complexes with β-diketones and observed a higher luminescence intensity when the complexes were excited in the absorption range for the organic ligand. This study culminated in the now-known phenomenon called the antenna effect.

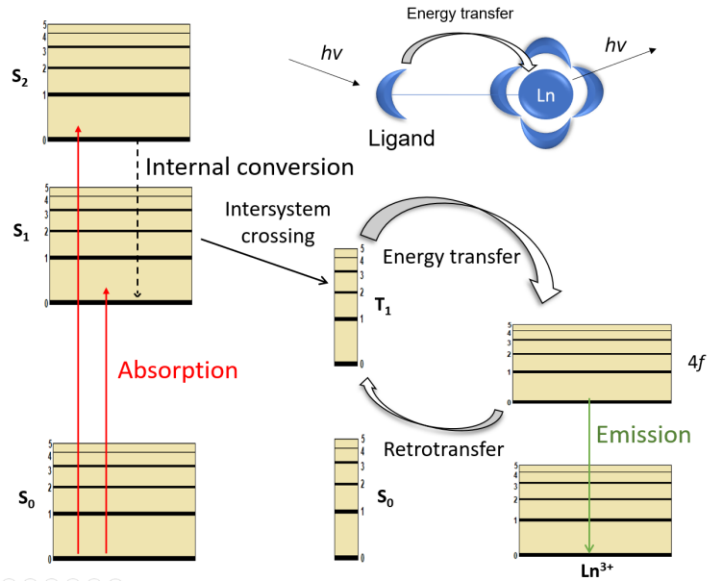

Figure 16: Representation of the antenna effect [27].

There are three different mechanisms by which the antenna effect can occur. However, the one displayed in Figure 16 is the most commonly observed in Eu^{3+} and Tb^{3+} ions [32]. In summary, the ligand's S_1 singlet excited state transfers energy through a non-radiative intersystem crossing to the lowest energy triplet state T_1. Later, an energy transfer occurs to the excited state of the Ln^{3+}, decaying radiatively to the fundamental state [28].

A few aspects must be considered to guarantee the most efficient luminescent effect. First, it is important that the energy of the triplet energy state of the organic ligand needs to be close but slightly above related to the emission state of the lanthanide ion. If these energy states are resonant and have the same energy, a retro-transfer effect occurs (Fig. 16), resulting in both phosphorescence and delayed fluorescence. The luminescence effect can present a quenching effect with the presence of H_2O molecules coordinated with the Ln^{3+} ion due to the vibrational coupling with O-H stretching frequency. In this regard, one of the strategies for better luminescence efficiency is the substitution of H_2O molecules with other ligands, such as carboxylates or chelates N-donor ligands [28].

As previously discussed, the Ln^{3+} $4f^n$ orbitals are strongly shielded by full $5s^2$ and $5p^6$ orbitals. Therefore, their properties are similar to free Ln^{3+} ions. Because of this, their emissions are characteristic of each lanthanide. Therefore, these transitions can be tabled. Table 2 shows all transitions found for Eu^{3+}-based compounds, and Table 3 shows all transitions found for Tb^{3+}-based compounds [33].

Table 2: Overview of the transitions observed in luminescence spectra of Eu^{3+} compounds

Transition	Dipole character	Wavelength range (nm)	Relative intensity	Remarks
$^5D_0 \rightarrow {}^7F_0$	ED	570-585	vw to s	Only in C_n, C_{nv} and C_s symmetry
$^5D_0 \rightarrow {}^7F_1$	MD	585-600	s	Intensity independent of the environment
$^5D_0 \rightarrow {}^7F_2$	ED	610-630	s to vs	Hypersensitive transition
$^5D_0 \rightarrow {}^7F_3$	ED	640-660	vw to w	Forbidden transition
$^5D_0 \rightarrow {}^7F_4$	ED	680-710	m to s	Dependent on environment
$^5D_0 \rightarrow {}^7F_5$	ED	740-770	vw	Forbidden transition
$^5D_0 \rightarrow {}^7F_6$	ED	810-840	vw to m	Rarely observed

ED = induced magnetic dipole transition, MD = Magnetic dipole transition

vw = very weak, w = weak, m = medium, s = strong, vs = very strong.

Table 3: Overview of the transitions observed in luminescence spectra of Tb^{3+} compounds

Transition	Wavelength range (nm)	Relative intensity	Remarks

$^5D_4 \rightarrow {}^7F_6$	480-505	m to s	Dependent on environment
$^5D_4 \rightarrow {}^7F_5$	545-555	s to vs	High optical activity, monitored in probe applications
$^5D_4 \rightarrow {}^7F_4$	580-600	w to m	Dependent on environment, modest optical activity
$^5D_4 \rightarrow {}^7F_3$	615-625	m to s	High optical activity
$^5D_4 \rightarrow {}^7F_2$	640-655	vw	Dependent on environment
$^5D_4 \rightarrow {}^7F_1$	660-670	vw	-
$^5D_4 \rightarrow {}^7F_0$	675-680	vw	-

vw = very weak, w = weak, m = medium, s = strong, vs = very strong.

1.4 Coordination Polymers

Coordination polymers (CPs) are a class of materials that, since the late 1950s, have been reported a large amount in the literature because of their capacity to cover a lot of fields [34], such as catalysis, gas adsorption, magnetism, luminescent probes, and so on [35][36][37]. To understand its multifunctionality, we need to understand its structure. CPs assemble metal centers or clusters with various organic ligands forming one-, two- or three-dimensional networks [38], as represented in Figure 17. If permanent porosity is present in 3D CPs, they can be referred to as Metal-organic frameworks (MOFs) or porous coordination polymers (PCPs) [39].

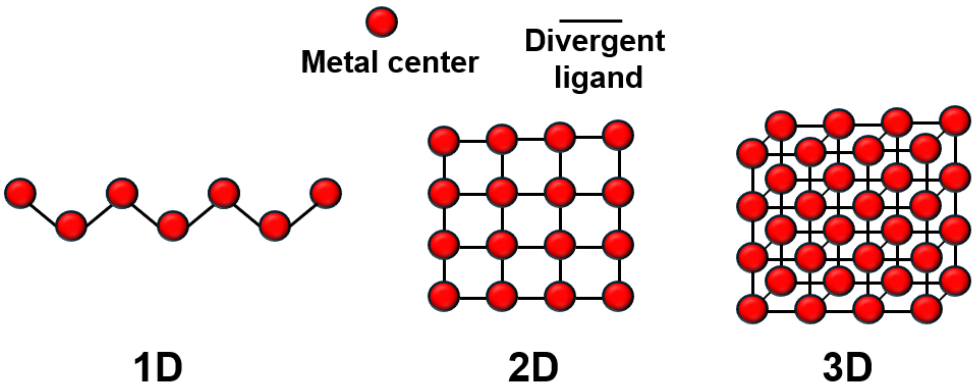

Figure 17: Representation of the dimensionality of coordination polymers (adapted from [40]).

Coordination chemistry has been demonstrated to be the most versatile choice for creating a wide variety of supramolecular structures since the presence of different metal ions in CPs, alongside the large organic molecules, can provide different coordination geometries [40]. As represented in Figure 18, there are two categories of organic ligands: divergent ligands and convergent/auxiliary ligands.

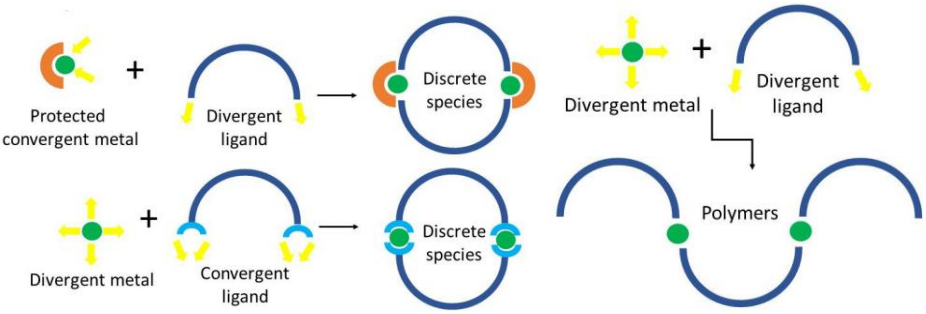

Figure 18: Distinct roles of convergent and divergent ligands for coordination chemistry.

Divergent ligands have several coordination sites and are responsible for the extension of the polymeric chain. An example of an interesting divergent ligand is polycarboxylic acids since they have high structural stability, act as a pathway for magnetic interactions, and several coordination sites [41]. Large divergent ligands are interesting for SIM behavior since they can generate small magnetic interactions due to the large distance between the metal ions. 1,3,5-tris(4-

carboxylphenyl)benzene (BTB) is a divergent ligand that shows great promise for developing these types of materials because of the presence of three coordination sites and its large width. Coumarin-3-carboxylic acid (3-HCCA) is a molecule that can form 1D coordination polymers coordinating through the carboxylic acid and the carbonyl from the lactone group.

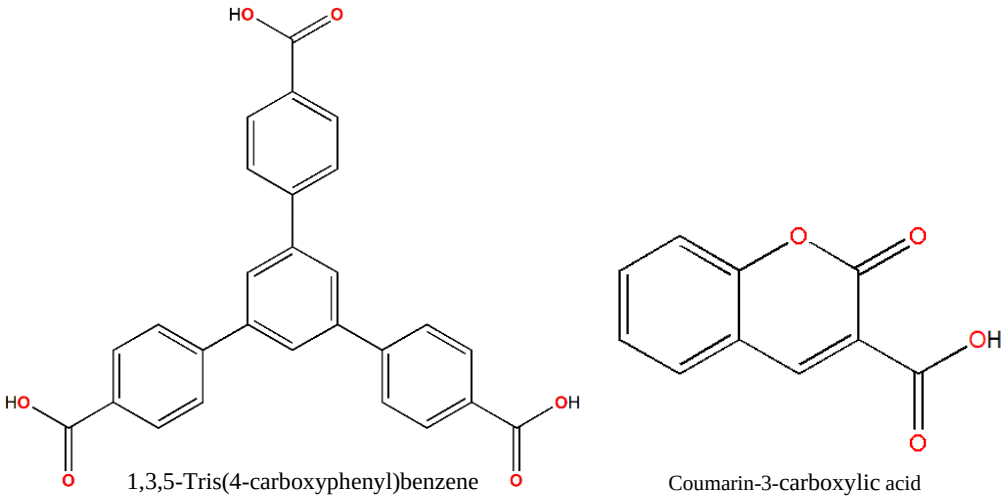

Figure 19: a) Structure of the BTB ligand. b) Structure of the 3-HCCA

Auxiliary ligands, on the other hand, are molecules that can affect the structure and properties of a polymer, and their insertion has been the topic of many investigations [42]. One way to vary the structure of the compound is to utilize chelating ligands that can prevent the expansion of the polymeric chain in certain directions. N-donor chelate ligands such as 1,10-phenanthroline and 5 5’-dimethyl-2 2’-bipyridine can generate different structure topologies [43].

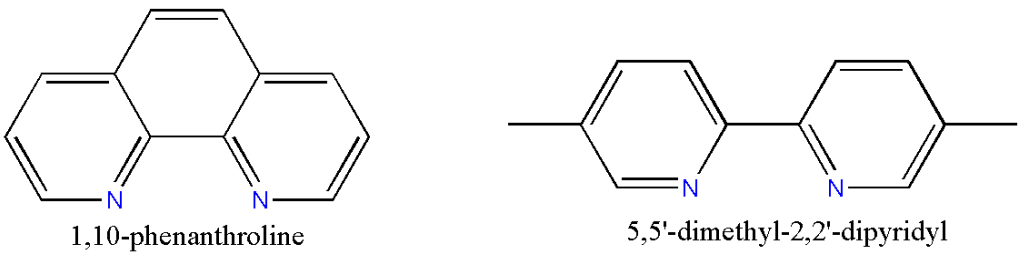

Figure 20: Structure of 1,10-phenanthroline and 5,5’-dimethyl-2,2’-dipyridyl.

1.5

State of the art

The development of new molecular nanomagnets is of extreme interest due to the different possible potential applications of these types of materials, such as in magnetic storage systems, molecular spintronics, qubits for applications in quantum computers, and many others. In that regard, many authors have adopted the interest in creating multifunctional materials, that is, materials that could be applied in many different areas. As discussed previously, nonzero-dimensional compounds such as coordination polymers enable this multifunctionality [44].

A bibliographic search used the keywords “Single Ion Magnet” and “Coordination Polymers” to better understand the project's current state of the art. Most works involve Co^{2+} and Ln^{3+} ions such as Gd, Tb, and Dy due to their already discussed magnetic properties.

Benmansour *et al.* [45] recently published a paper on developing three Dy^{3+} coordination polymers utilizing Anilato ligands with different substitutions. Due to the structure of the ligand, they obtained a Metal-Organic Framework (MOF). They studied the magnetic properties, where a Single-Ion Magnet behavior was obtained with an energy barrier ranging from 30-42 K.

Uhlmann and co-authors [46] have recently also published work that has received much attention regarding the publication time. They published the first rare-earth complexes with an organometallic ligand that contains 14-π-electrons. In their coordination polymer, the Ln ions are sandwiched between the aromatic rings of the ligands, and the polymeric chain extends in the direction of these rings. They obtained SMM behavior for both Dy^{3+} and Er^{3+} complexes.

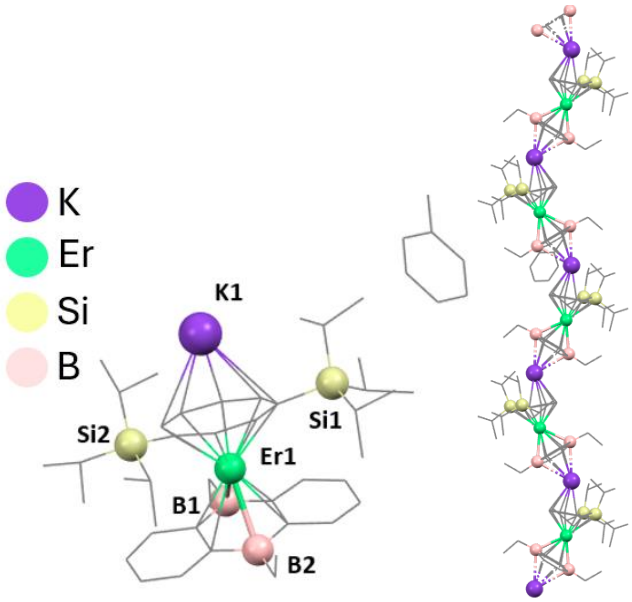

Figure 21: Geometry and polymer extension from the discussed work [46].

The use of carboxy ligands for synthesizing coordination polymers is well evidenced in Hong and co-authors work [47], where they obtained lanthanide-based 1D multifunctional coordination polymers utilizing a dicarboxylate ligand. The supramolecular arrangement of the polymer resulted in a small interaction between polymeric chains, and when dynamic magnetic studies were conducted, single-chain Chain Magnet behavior was evident.

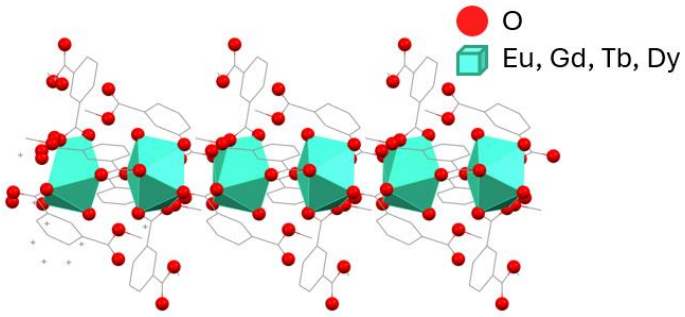

Figure 22: Geometry and polymeric extension from the discussed work [47].

Many works have presented the system of uniting carboxylates with auxiliary N-donor ligands. Two works utilize the BTB alongside phenanthroline. The first is a 2018 work from Nguyen et al. [47], where they obtained an Ytterbium

(Yb) 2D coordination polymer that emits near-infrared. The most recent work is from Coban [48], in 2023, where a 3D dimeric MOF Ho^{3+} was obtained through a solvothermal route, exhibiting very strong and characteristic luminescence emission in the visible region.

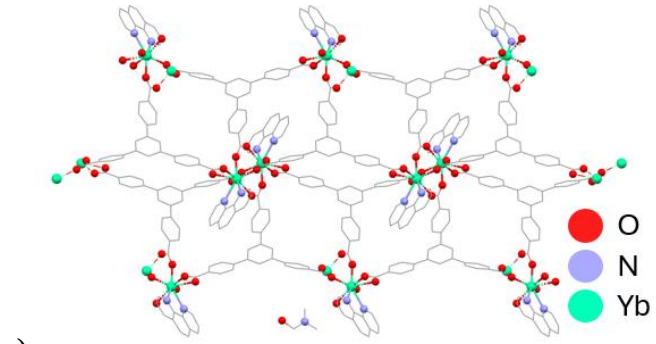

a)

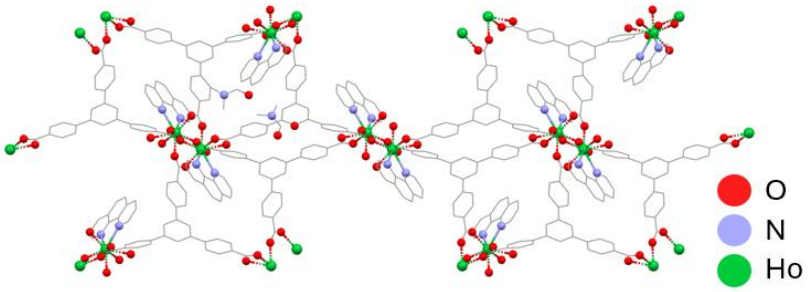

b)

Figure 23: a) 3D polymeric chain from [48] b) 3D polymeric chain from [49].

Co^{2+} ions are also of extreme interest to develop these CPs due to its high anisotropy caused by ZFS. Tao Long and co-authors [50] developed two rare 4-coordinated Co^{2+} coordination polymers that present zigzag and ribbon 1D topologies. This tetrahedral geometry resulted in uniaxial anisotropy in magnetization along its C_2 axis, mostly dependent on the N_{py}-Co-N_{py} bite angle.

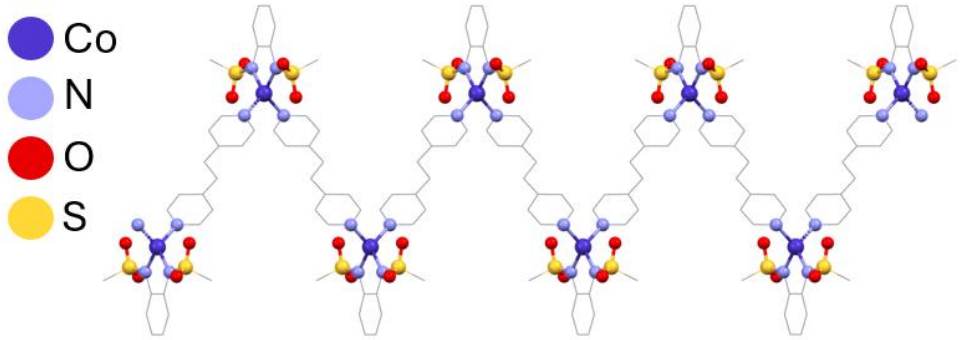

Figure 24: Polymer extension and geometry of the metal ion from the discussed work [50].

To illustrate the possibles applications of molecular magnets we selected a few works. Molecular magnets are one of the candidates for the development of qubit devices. Fursina and Sintskii [51] recently published a review in which they went through many important compound synthesized for this application. Firstly, they explained that a good candidate for qubit are compounds that have a long coherence time (lifetime of quantum superposition state), and this parameter is related to both spin-lattice relaxation time and spin-spin relaxation time. Stewart *et al*. [52] developed a Ho based complex that has potential work as qubits since it has an easy-axis anisotropy and $m_j = \pm 8$ quasi-doublets ground state that is well separated from excited crystal field states.

Molecular magnetism is also present in refrigerate systems due to the previously discussed magnetocaloric effect. Wang *et al*. [53] calculated magnetocaloric effect for Gd^{3+} complexes, where they obtained a $-\Delta S_m$ smaller than the theoretical value, likely due to antiferromagnetic interactions between the Gd ions. Zhang *et al*. [54] developed two frustrated lanthanide molecular compounds, in which the frustrated configuration of Gd^{3+} spins lead to low temperature paramagnetic state, prohibiting magnetic transition and these systems maintain paramagnetic behavior at least down to 290 mK. With this cubane network, they

attain extremely low temperatures below 1K with demagnetization range from 2 to 4 T.

The current focus on molecular magnetism is the development of new systems capable of generating molecules with higher anisotropy for SIM behavior at higher temperatures. Ligands such as BTB are of great interest due to their large size and the development of multifunctional materials. These ligand and auxiliary N-donor molecules can generate different structures. 3-HCCA is a ligand that was not explored in molecular magnetism, but its structure allows the creation of CPs with possible SCM behavior. With this panorama, different systems have been developed utilizing these ligands alongside *d* block metals such as Cu^{2+} and Co^{2+} and lanthanides as Eu^{3+}, Gd^{3+}, Tb^{3+}, and Dy^{3+}.

2
Objective

2.1
General objective

Develop coordination compounds based on the combination of two different groups of organic ligands (carboxylato and N-donor), with either transition metals ions such as Co^{2+} and Cu^{2+} or lanthanide ions such as Eu^{3+}, Gd^{3+}, Tb^{3+}, and Dy^{3+}, and evaluate their potential as molecular nanomagnets and the photoluminescent properties of Eu^{3+} and Tb^{3+} based compounds.

2.2
Specific objectives

Synthesize two different systems of coordination compounds. The first family contains transition metal ions such as Co^{2+} and Cu^{2+}, BTB, and either Phen or Dmdpy acting as a N-donor ligand. The second system includes two different compound families presenting Ln^{3+} ions alongside 3-HCCA ligand, but differing regarding the proportion of metal-ligand, in the first family being 1:1 and the second family being 1:3;

- Compare the different structural, magnetic, and photoluminescent properties when changing the N-donor ligand and the number of organic ligands coordinated to the metal ion;
- Characterize the synthesized compounds' structure through infrared spectroscopy, thermogravimetry, and monocrystal and

polycrystal X-ray diffraction when the non-amorphous sample is obtained;

- Study the magnetic properties of each system through many different techniques, such as electron paramagnetic resonance (EPR), through DC magnetic fields for in-phase magnetic susceptibility data and AC magnetic fields to evaluate the possibility of out-of-phase signals characteristic of molecular nanomagnets;
- Estimate both the energy barrier found in the molecular nanomagnets as well as the relaxation of magnetization time found for each system;
- Study photoluminescent properties for Eu^{3+} and Tb^{3+} complexes through a fluorimeter, estimate the antenna effect efficiency for each complex, and determine the emission state lifetime.

3

Methodology

3.1

Synthesis of MBTBPhen system

3.1.1

Synthesis of $\{[Cu(H_3BTB)_2(phen)](NO_3)_2\}_n$ and $\{[Co(HBTB)_2(phen)]DMF\}_n$

Synthesis for both coordination polymers followed the same procedures, and its scheme is represented in Figure 25. For Cu^{2+} complex (**1**), 2,5 mL of distilled water containing copper(II) chloride dihydrate (8 mg, 0.04 mmol) was added to a 2,5 mL solution of DMF containing BTB (30 mg, 0.06 mmol) and phenanthroline (8.5 mg, 0.05 mmol). Blue crystals suitable for single-crystal X-ray analysis were formed after a few days of slow evaporation at room temperature (Yield: 50.49 %). The Co^{2+} complex (**2**), 2,5 mL of distilled water containing cobalt(II) nitrate hexahydrate (13,5 mg, 0.057 mmol) was added to a 2,5 mL solution of DMF containing BTB (50 mg, 0.11 mmol) and phenanthroline (10,3 mg, 0.06 mmol). Red crystals suitable for single-crystal X-ray analysis were formed after a few days of slow evaporation at room temperature (Yield: 32.65 %).

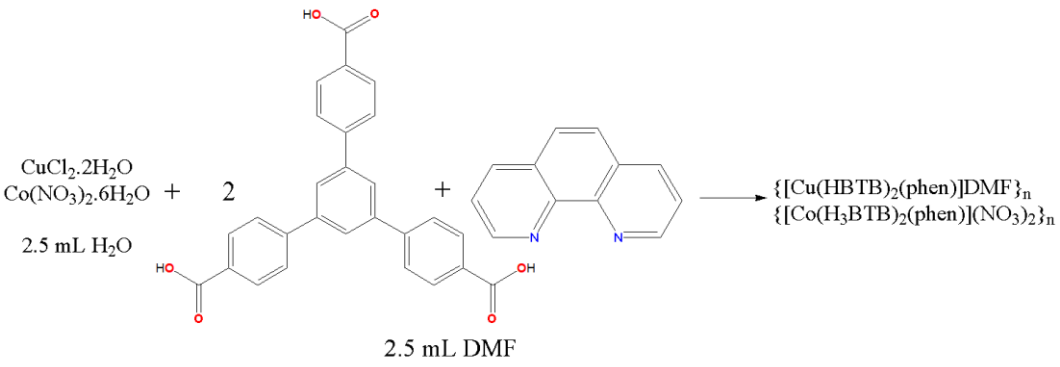

Figure 25: Synthesis for **1** and **2**.

3.1.2

Synthesis of [Cu(HBTB)Dmdpy]·2H_2O

Synthesis for [Cu(HBTB)Dmdpy] ·2H_2O (**3**) is represented in Figure 26. In summary, 2,5 mL of distilled water containing copper(II) chloride hexahydrate (7.8 mg, 0.045 mmol) was added to a 2,5 mL solution of DMF containing BTB (20 mg, 0.045 mmol) and 5,5'-dimethyl-2,2'-pyridyl (8.4 mg, 0.045 mmol). Blue crystals suitable for single-crystal X-ray analysis were formed after a few days of slow evaporation at room temperature.

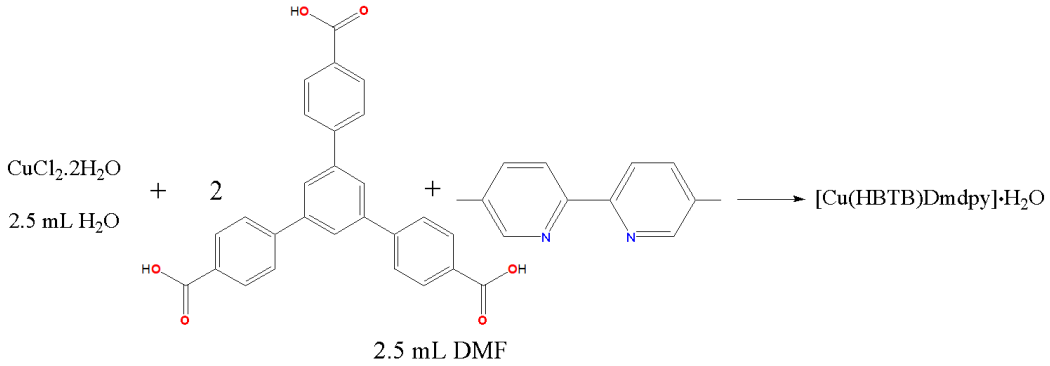

Figure 26: Synthesis of 3.

3.2

Synthesis of Ln(3-HCCA)$_n$ system

3.2.1

Synthesis of {[$LnCl_2$(3-CCA)(H_2O)$_3$]H_2O}$_n$

The synthesis of all four coordination polymers that is a part of the family {[$LnCl_2$(3-CCA)(H_2O)$_3$]H_2O}$_n$ (Ln = Eu (**4**), Gd (**5**), Tb (**6**) and Dy (**7**)) followed the same procedure and it's represented in Figure 27. At first, the respective lanthanide salt was dissolved in a mixture of 5 mL of Ethanol and 2.5 mL of distilled water. Coumarin-3-carboxylic acid was dissolved in a mixture of Ethanol and Acetone, with 5 mL each. The proportion of Ln and Coumarin is 1:1. Both solutions

were mixed and put to magnetic agitation at room temperature for 1 hour. After slow evaporation, pink crystals were obtained for characterization analysis.

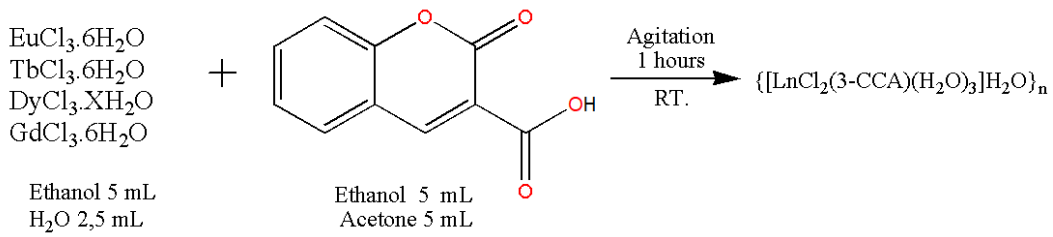

Figure 27: Scheme of the $\{[LnCl_2(3\text{-}CCA)(H_2O)_3]H_2O\}_n$ synthesis.

3.2.2

Synthesis of $\{[Ln(3\text{-}CCA)_3(H_2O)_2](H_2O)_2\}_n$

The synthesis of all four coordination polymers contained in the family $\{[Ln(3\text{-}CCA)_3(H_2O)_2](H_2O)_2\}_n$ (ln = Eu (**8**), Gd (**9**), Tb (**10**) and Dy (**11**)) followed the same procedure as previously described. However, the difference is regarded as the ratio of Ln:HCCA, which changed from 1:1 to 1:3. As summarized, the respective lanthanide salt was dissolved in a mixture of 5 mL of Ethanol and 2.5 mL of distilled water. Coumarin-3-carboxylic acid was dissolved in a mixture of Ethanol and Acetone, with 5 mL each. Both solutions were mixed and put to magnetic agitation at room temperature for 1 hour. After slow evaporation, colorless crystals were obtained for characterization analysis.

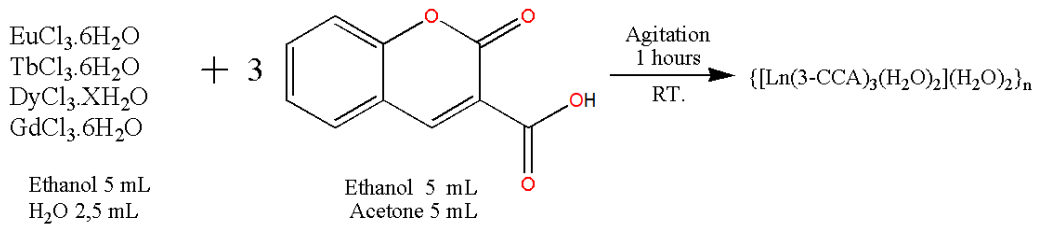

Figure 28: Scheme of the $\{[Ln(3\text{-}CCA)_3(H_2O)_2](H_2O)_2\}_n$ synthesis.

3.3
Instrumentation

FTIR analyses were performed in ATR mode using 32 scans and a resolution of 4 cm1 using an Alpha II spectrometer (Bruker).

Thermogravimetry was conducted with a Perkinelmer pyris 1 TGA analyzer under a nitrogen atmosphere at 25–800 ◦C and a heating rate of 10 ◦C min 1. These analyses were conducted by Professor Rodrigo Souza from PUC-Rio.

Powder X-ray diffraction data for all the samples were collected on a Bruker D8 Discover instrument equipped with a copper tube, nickel filter, and Lynxeye detector. The scans were obtained in the 2θ range 5 to 60◦, with a step of 0.02◦and 0.5 s per step. A beam knife was used to reduce air scattering. These analyses were conducted and refined by Professor Sonia Letichevsky from PUC-Rio.

Single-crystal X-ray diffraction data for compounds 1 and 2 were collected on a Bruker D8 Venture diffractometer with Mo Kα (λ = 0.71073 Å) radiation at 298 K. Data collection and cell refinement were performed with Bruker Instrument Service v4.2.2 and APEX4, [55], respectively. Data reduction was carried out using SAINT [56]. Empirical multiscan absorption correction using equivalent reflections was performed with the SADABS program [57]. All the crystal structures were solved and refined using the SHELXS and SHELXL packages [58]. The structures were drawn using the ORTEP-3 for Windows [59] and Mercury programs [60]. These analyses were conducted and refined by Professor Guilherme Pereira Guedes from UFF, Professor Renata Diniz from UFMG, Professor Jorg Daniels from Uni-Bonn, Germany, and Professor Adriano Oliveira from UFS.

Magnetic field measurements were performed using a vibrating sample magnetometer (VSM) and an AC Measurement System (ACMS) operating in accordance with the Quantum Design Physical Properties Measurement System

(PPMS). The data were corrected based on the diamagnetic contributions of both the sample holder and the sample. The Magprop routine of the Dave program [61] was employed for the static magnetic data fitting process. Professor Luís Ghivelder from UFRJ and Professor Stéphane Soriano from UFF conducted and refined these analyses.

The electronic paramagnetic resonance (EPR) spectrum of 2 was recorded in the solid-state (300 K) on a Bruker EMX-Plus spectrometer with an X-band cavity (9.5 GHz) and a microwave power of 10 mW. The spectrum was simulated using the EasySpin [62] MATLAB routine. Professor Odivaldo Cambraia from UFF conducted and refined these analyses.

Emission spectra were recorded in a HORIBA Jobin Yvon spectrofluorimeter model Fluorolog FL3-221, equipped with CW xenon flash lamp and a photodiode detector (HORIBA PPD-850). The excited state lifetime values of Eu^{3+} and Tb^{3+} were determined by exponentially fitting the PL decay curves using a pulsed flash lamp. Bruno Onishi and Sidney Ribeiro (UNESP) conducted these experiments.

4

Results and discussion

4.1

Synthesis, characterization, and magnetic properties of three complexes involving Co^{2+}, Cu^{2+}, 1,3,5-Tris(4-carboxylphenyl)benzene, 1,10-phenanthroline and 5,5'-dimethyl-2,2'-dipyridyl.

4.1.1

$\{[Co(H_3BTB)_2(phen)](NO_3)_2\}_n$ and $\{[Cu(HBTB)_2(phen)]\ DMF\}_n$

In this section, a system utilizing the H_3BTB as a divergent ligand and 1,10-phenanthroline as a chelate auxiliary ligand was obtained. Two different CPs were obtained in this system, differing in the metal ion utilized, being for CP1 Cu^{2+} and for CP2 Co^{2+}. Structural characterization such as Infrared spectroscopy, thermogravimetric, single-crystal and polycrystal X-Ray diffraction were conducted. For CP1 EPR measurements were conducted, while for CP2 both direct and alternated magnetic measurements were conducted due the possible SMM behavior as observed for some Co^{2+} based complexes reported in the literature.

4.1.1.1

Structure characterization

4.1.1.1.1

Infrared spectroscopy analysis

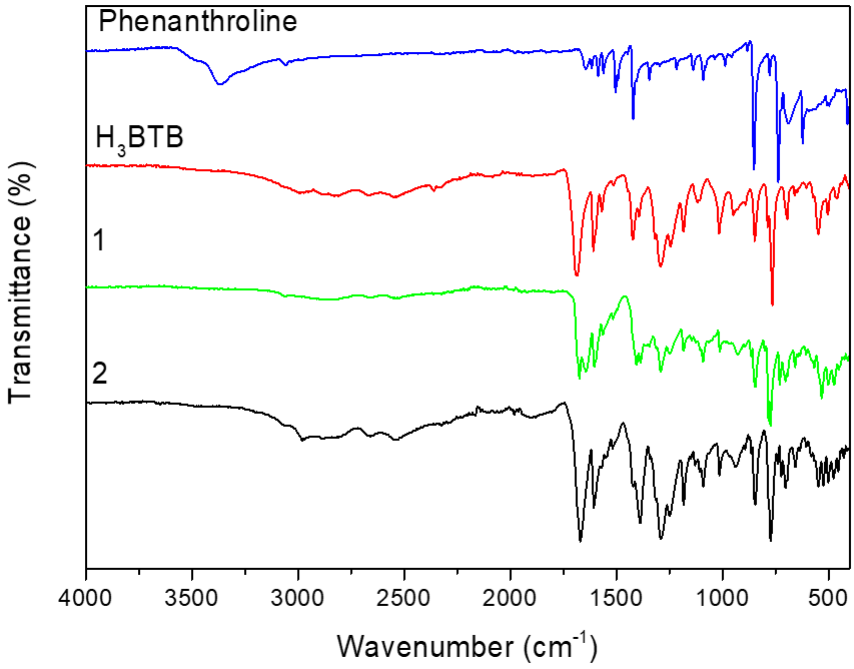

Figure 29: FTIR analysis of the pre-ligands, **1** and **2**.

Both coordination polymers were characterized by infrared spectroscopy, as shown in Figure 29. This analysis is made to have an early indication of the coordination of the organic ligands to the metallic ions by verifying a slight shift in bands from the free ligands and the complexes. At first, a strong band at 1686 cm^{-1} (νC=O) attributed to the BTB ligand was shifted to 1669 cm^{-1} and 1673 cm^{-1} in Co(II) and Cu(II) complexes, respectively [63]. The ν(CC) and ν(CN) modes from the free 1,10-phenanthroline ligand at 1643 cm^{-1}, 1615 cm^{-1} and 1585 cm^{-1} are overlapped (due to a strong peak at 1607 cm^{-1} from BTB) for both complexes [64]. The coordination of the Phen ligand can be indicated from the shifts of the bands around 855-730 attributed to the motions of the τ(CCCC) phen rings [65], where it

goes from 850 cm^{-1}, 777 cm^{-1} and 736 in the free ligand to 844 cm^{-1},772 cm^{-1} and 729 cm^{-1} for both complexes.

Table 4: Main infrared bands for free organic ligands, **1** and **2.**

Vibrational modes	H_3BTB	Phen	**1**	**2**
ν_{C-H} (DMF)	-	-	2975 cm^{-1}	-
$\nu_{C=O}$	1686 cm^{-1}	-	1670 cm^{-1}	1674 cm^{-1}
$\nu_{CC/CN}$	-	1644 cm^{-1}	1639 cm^{-1}	1642 cm^{-1}
$\nu_{CC/CN}$	-	1585 cm^{-1}	1547 cm^{-1}	1562 cm^{-1}
$\tau_{(CCCC)}$	-	850 cm^{-1}	844 cm^{-1}	844 cm^{-1}
$\tau_{(CCCC)}$	-	777 cm^{-1}	772 cm^{-1}	772 cm^{-1}
$\tau_{(CCCC)}$	-	736 cm^{-1}	729 cm^{-1}	729 cm^{-1}

4.1.1.1.2

Structure description

Table A1 displays crystal data and refinement results for both Co^{2+} and Cu^{2+} complexes. Ortep images of the asymmetric units of both complexes are displayed in Fig. A1 and Fig. A2. Both complexes are isostructural, and their fragments and coordination environments are displayed in Figure 30 (hydrogen atoms, solvent, and counterions were omitted for the sake of clarity).

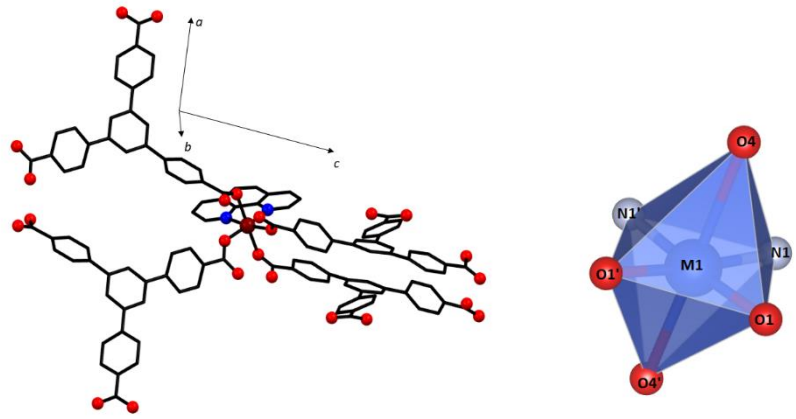

a) b)

Figure 30: a) Fragment of the coordination polymers. b) Polyhedral representation of the coordination environment of metal ions.

Two nitrogen atoms (N1 and N1') from the Phen ligand are coordinated to the metal ion forming a chelate ring of 4 members, and the coordination sphere is completed by four oxygen atoms (O1 and O4) from four monodentate BTB molecules, resulting in a coordination number of 6, with both metal ions adopting a distorted octahedral geometry. BTB molecules act as bridges between the metal ions, forming a one-dimensional coordination polymer extending at the crystallographic axis *c*, as displayed in Figure 31.

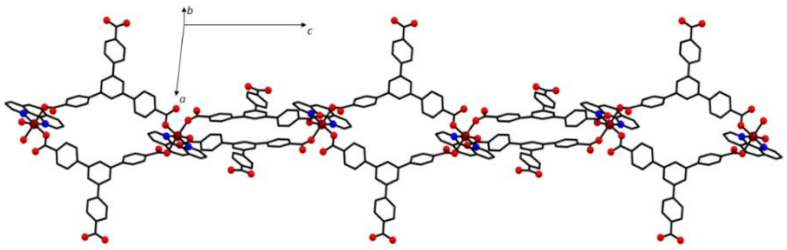

Figure 31: Extension of the polymeric chain.

Even though both complexes have the same coordination environment and structure, they present slight differences in bond lengths and bond angles. The main

bond distances and angles for both complexes are displayed in Table 5. It's observed that for Co^{2+} complex, the Co-O distances vary between 2.027(1) Å and 2.156(1) Å, while the Co-N distance is 2.115(2) Å. The smallest angle found is the N1-Co1-N1, with a value of 78.80(11) °, and the biggest angle is the angle between O4-Co1-O4 of 170.19(7)°. For the copper(II) complex, the Jahn-Teller stretch effect can be observed by comparing the distances of Cu^{2+} ion with the different oxygens with Cu1-O1 bond distance being of 1.928(16) Å while Cu1-O4 bond distance value is 2.477(1) Å. The remaining bond distance Cu1-N1 has a value of 2.014(2) Å. The smallest angle found is the N1-Cu1-N1, with a value of 82.32(14) °, and the biggest angle is the angle between O4-Cu1-O4 of 172.12(9)°. The bonds from Co^{2+} (excluding the bond stretched by the Jahn-Teller effect) are slightly smaller than Cu^{2+}, which can be attributed to the bigger value of electronegativity from the copper ion compared to the cobalt ion. Both CPs have a high interchain metal-metal distance (16.2 Å) due to BTB's size, a value that indicates a small magnetic interaction between these metal atoms.

Table 5: Selected bond distances and angles for both polymers.

1									
Bond distances (Å)		**Angle(º)**			**Bond distances (Å)**			**Angle(º)**	
Cu1-O1	1.928 2(16)	O1-Cu1-O1	97.97(11)	Co1-O1	2.027(1)	O1-Co1-O1	97.97(8)	Co1-O1	2.027(1)
Cu1-N1	2.014(2)	O1-Cu1-N1	89.86(9)	Co1-N1	2.115(2)	O1-Co1-N1	91.65(6)	Co1-N1	2.115(2)
Cu1-O4	2.477(1)	O4-Cu1-O4	172.1 2(9)	Co1-O4	2.156(1)	O4-Co1-O4	170.1 9(7)	Co1-O4	2.156(1)
Cu1···Cu1	16.26 5(8)	N1-Cu1-N1	82.32(14)	Co1···Co1	16.24 9(8)	N1-Co1-N1	78.80(11)	Co1···Co1	16.24 9(8)

Among the intermolecular interactions that stabilize the crystalline packing, it can be highlighted the presence of hydrogen bonds between BTB molecules with a distance of 2.15(9) Å for **1** and 1.71(6) for **2**, as shown in Figure 32, and π-π stacking from the benzene rings with a centroid distance of 3.70(8) Å for **1** and 3.67(8) Å for **2**. The smallest distance between metal ions of different polymeric chains to be around 10.6 Å for both complexes. This large distance indicates a small magnetic interaction between polymeric chains.

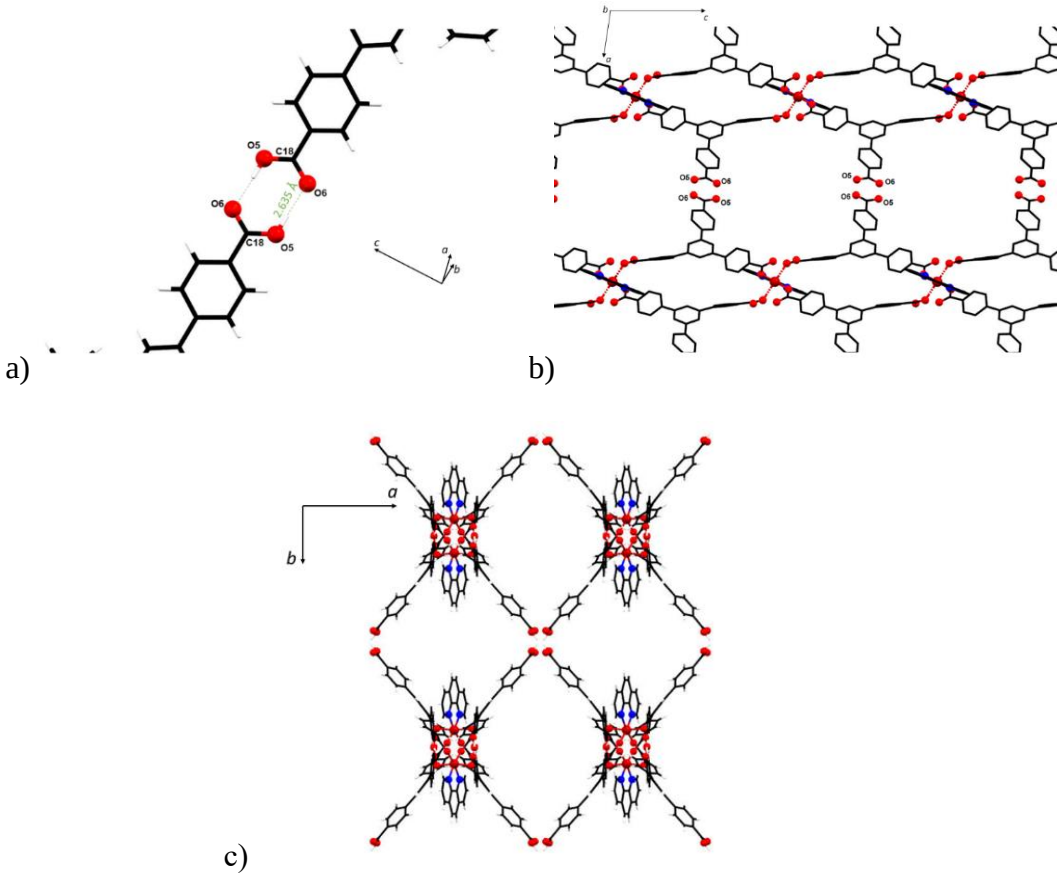

Figure 32: a) H bond interactions between chains. b) H bond interactions between chains seen through crystallographic axis b. c) H bond interactions between chains seen through crystallographic axis c.

Powder X-ray diffraction measurements for both complexes are displayed in Figures 33. The experimental diffractogram was compared with the calculated one obtained from the structure solved by single crystal X-ray diffraction data. For both complexes, the diffraction pattern from both data matches, indicating a good phase purity.

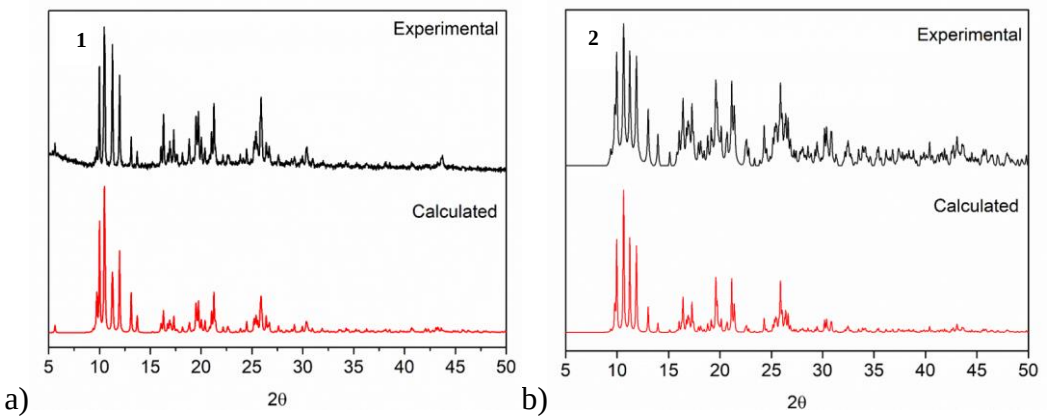

Figure 33: a) PXRD analysis for **1**. b) PXRD analysis for complex **2**.

4.1.1.1.3 Thermal analysis

Thermogravimetric and Derivative thermogravimetric analyses were performed on polycrystalline samples for both complexes under a dynamic nitrogen atmosphere (Fig. 34). TG and DTG analysis for both complexes evidence three weight loss steps. For complex **1,** the first step happens at a temperature range of 100-230 °C, and corresponds to a 7.4% weight loss, which can be attributed to the loss of the DMF molecule. The following two steps correspond to a 54.2% and 28.3% weight loss at 300 °C and 365-540 °C, respectively, and indicate the total collapse of the framework. The mass stabilizes at 540 °C. For complex **2**, the first weight loss happens at 88-99 °C, corresponds to 7.6% mass loss and it's attributed to the NO_3^{-1} ion. The second and third weight loss happens at a temperature range of 380-460 °C, and it's related to the decomposition of organic ligands. A stable mass is obtained at 460 °C, indicating that complex **1** is more thermally stable than complex **2**.

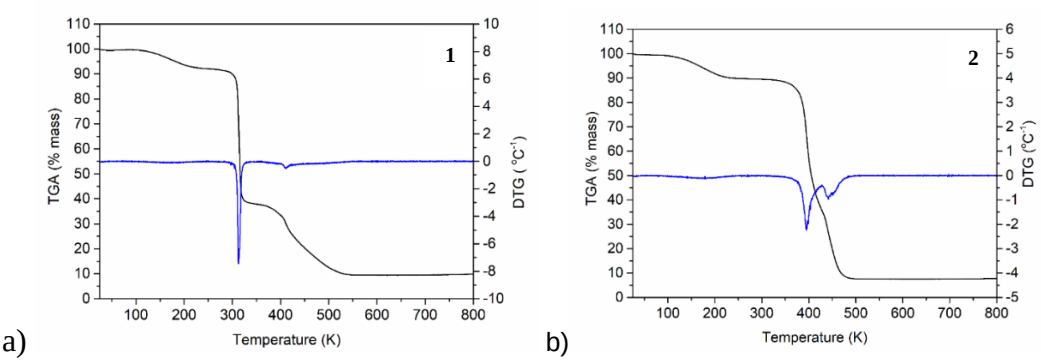

a) b)

Figure 34: TGA analysis for a) 1. b) 2.

4.1.1.2

Magnetic properties

4.1.1.2.1

{[Cu(HBTB)$_2$(phen)]DMF}$_n$

Hyperfine interactions are manifested in EPR spectrum by small splitting of resonance lines characterized by the interaction between the electronic and nuclear spin magnetic moments. There are $2nI + 1$ values of n_I ($n_I = I, I-1, \ldots, 0, \ldots, -I+1, -I$); when the hyperfine interactions occur, its terms divide the Zeeman transition into $2I+1$ lines of equal intensity. For the case of an interaction with only one proton, we have a value of $I = ½$. Therefore, we have two lines in the EPR spectrum [21].

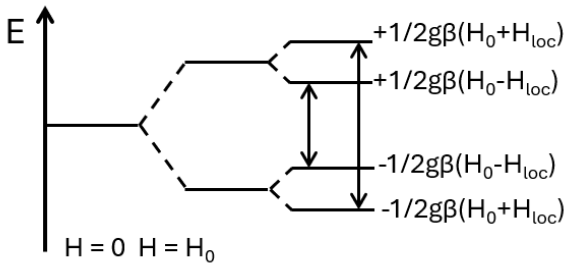

Figure 35: Hyperfine interactions representation (adapted from [20]**)**.

Copper samples present a typical EPR signal due to their hyperfine interactions. Cu^{2+} presents a nuclear spin of 3/2, so the Zeeman line will be split into four lines (n_I = 3/2, 1/2, -1/2, and -3/2).

X-band EPR spectroscopy was performed for copper complex in solid-state at room temperature (300 K) (Fig. 36). Two g tensors values were obtained, with it being $g_{\parallel} = 2.26$ and $g_{\perp} = 2.085$ in the axial spectrum. This value of g is typical for the $d_{x^2-y^2}$ orbital of the unpaired electron ground state. It is associated with the N_2O_2 ligand set in the xy Cu^{2+} ion plane. The g parallel to the spectrum exhibits signals due to hyperfine interactions, as shown in the inset of Figure 36, between unpaired electrons and the Cu nucleus with a nuclear spin of 3/2. The hyperfine constant obtained by simulation using the easy spin MATLAB routine is 163.10^{-4} cm^{-1}. It is difficult to resolve the hyperfine interactions in the powder EPR spectrum, suggesting that the Cu^{2+} centers are isolated [48].

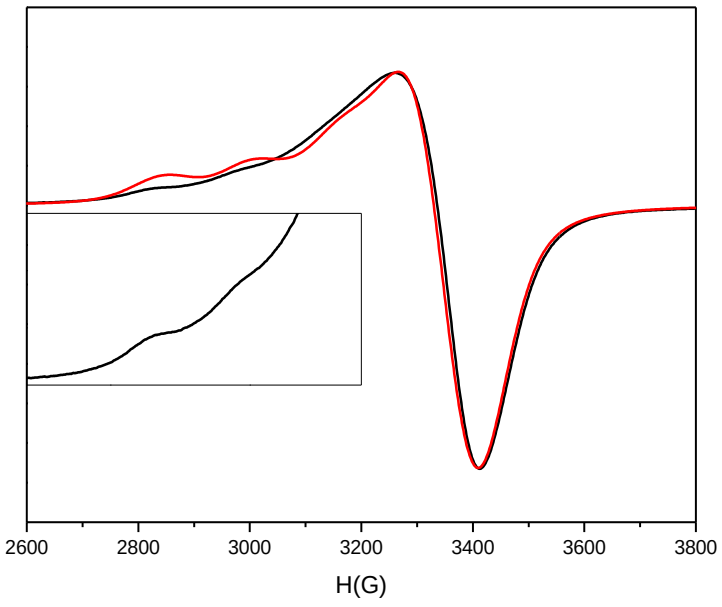

Figure 36: Powder EPR spectra (in black) recorded in derivative mode at 9.39 GHz and T = 300 K, for compound **1**. The calculated spectrum is shown as a red line.

Additionally, the experimental EPR spectrum of complex **1** could be reproduced without considering any magnetic coupling constant (J). This is further evidence that the metal centers in both complexes are essentially isolated, as proposed by the small J obtained from the CASSCF calculations and magnetic susceptibility measurements.

4.1.1.2.2

$\{[Co(H_3BTB)_2(phen)](NO_3)_2\}_n$

The polymeric structure can provide some indications regarding the magnetic properties that the compound can present. As discussed previously, Figure 37 shows that the intrachain distance between metal ions is around 16.2 Å, indicating that the magnetic interactions amongst these metals in the polymeric chain are weak. However, this distance is not the smallest found in the crystalline structure, which is a distance of 10.65 Å for Co-Cp and 11.03 Å for Cu-CP between chains. Still, there is a large distance for significant magnetic interactions, but its contribution to the Hamiltonian is present. Secondly, the angle M-BTBcentroid-M for Co-CP is 114.31°, and for Cu-Cp is 113.92°, which means it is not an ideal superposition for ferromagnetic interactions (orthogonal superposition). Therefore, we can expect antiferromagnetic interactions.

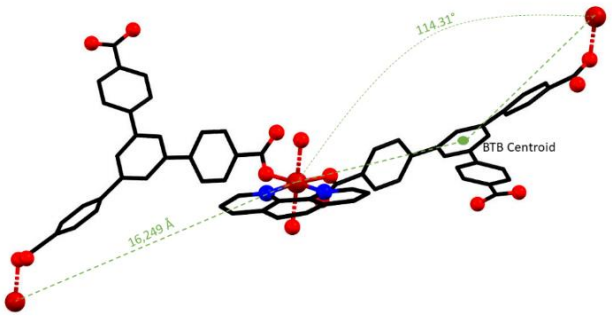

Figure 37: Distance and angle between metal ions.

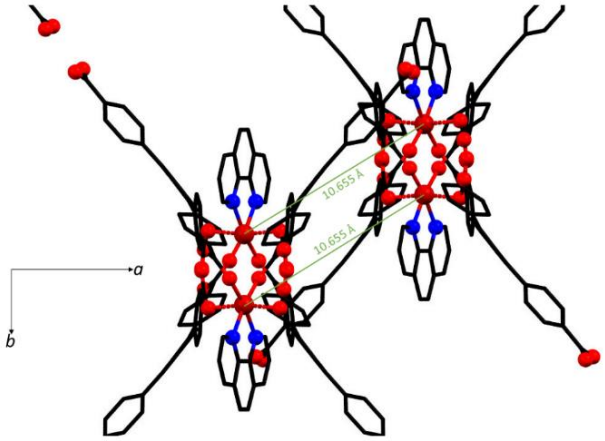

Figure 38: Smallest metal-metal distance between polymeric chains.

Cobalt(II) ions are interesting for magnetic studies due to their unique properties. Due to its high fundamental state value of S=3/2 (spin magnetic moment), the zero-field splitting (ZFS) is highly present. ZFS arises from spin-orbit coupling and produces a single-ion magnetic orientation with lower energy, called anisotropy [66]. Co^{2+} centers also present distortions from octahedral symmetry, removing the degeneracy of $^4T_{1g}$. If the distortion is tetragonal, the ground state becomes $^4A_{2g}$ with an excited state ^4E_g.

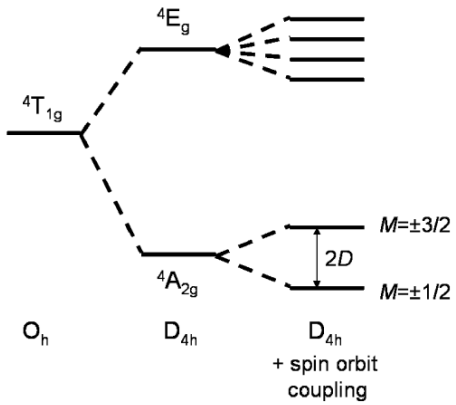

Figure 39: Combined effect of tetragonal distortion and spin-orbit coupling on energy levels of high spin Co^{2+} [67].

Spin-orbit coupling results in six Kramer's doublets, with an M = ±1/2 ground state and M = ±3/2 first excited states. The gap between these states is

measured as 2D, with D being a “quantification” of anisotropy; hence, the bigger its value, the bigger the preference for a magnetic orientation [68].

Magnetic susceptibility data from **2** was investigated in the temperature range of 3K-320K, represented by the product of $\chi_M T$ versus T is shown in Figure 40. At 320 K, the $\chi_M T$ value is approximately 2.2 cm^3mol^{-1} K, and upon cooling, we see a continuous decrease to 1.27 cm^3mol^{-1} K at 3K. This behavior can result from antiferromagnetic interactions; however, we cannot exclude the zero-field splitting effect for metal ions with S ≥1, which produces the same effect in susceptibility data. The magnetic saturation value obtained is greater than the expected value for uncoupled spin-only contributions (1.88 $cm^3mol^{-1}K$), indicating the presence of an orbital part in the magnetic moment.

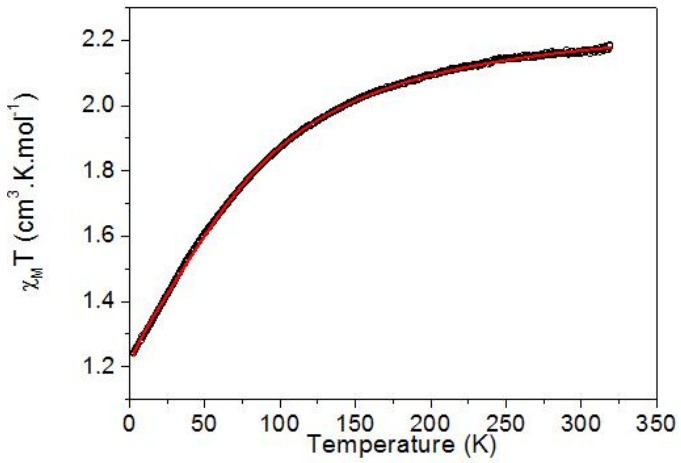

Figure 40: Thermal dependence of the $\chi_M T$ product for **2**. The red solid line corresponds to the best fit.

To better understand the magnetic field data, we utilized the spin Hamiltonian (Eq. 16), where μ_B = Bohr magneton, D = ZFS axial parameter, S = Spin magnetic moment, g = tensor g, and zJ’ = intermolecular interactions. For this, only the axial term was considered, and the contribution of the magnetic interactions within the compound was included through a mean field approximation.

$$\hat{H} = \mu_B g \vec{B} \cdot \hat{S} + D\hat{H}_z^2 - zJ'\langle S_z \rangle \hat{H}_z \qquad \text{(Eq. 16)}$$

The best fit was achieved using the following parameters: gx = gy = 2.04(1), gz = 2.50(1), D = 74.7(3) cm^{-1} and zJ' = -0.05(1) cm^{-1}. As seen from these fits, we have a small value of zJ' of -0.05(1) cm^{-1}, indicating small magnetic interactions of different polymeric chains, corroborating to the first assumption due to the large distance between metal cores of different chains.

As previously discussed, the D value is a numeric representation of the compound's anisotropy, and we obtained a high value of 74.7(3) cm^{-1}, which lies withing the observed range for octahedral Co^{2+} ions [10][69] and corresponds to an easy-plane magnetic configuration (D>0). This confirms a weak antiferromagnetic interaction within the compound, which was expected from the long distances between the metal centers. This suggests that the magnetic behavior of the compound is governed by the magnetic response of single Co^{2+} ions.

Because of this magnetic response behavior of single Co^{2+} ions and high anisotropy, **2** showed great potential as a single-ion magnet. In-phase and out-of-phase magnetic susceptibilities data was obtained to investigate its potential as a molecular nanomagnet. In the absence of a static background magnetic field (H = 0 Oe) no signal was obtained. Cobalt-based SIMs reported in the literature tend to present strong quantum tunneling of magnetization at low temperatures. Therefore, no slow relaxation of magnetization was observed [10][44][71]. We can remove this effect by applying a static magnetic field to change the system's energy levels, as represented in Figure 41. To determine the best-applied field, the frequency-dependent magnetic susceptibilities were measured to different static magnetic fields at 3 K (Figure 42), where we selected the optimum magnetic field as 2 kOe.

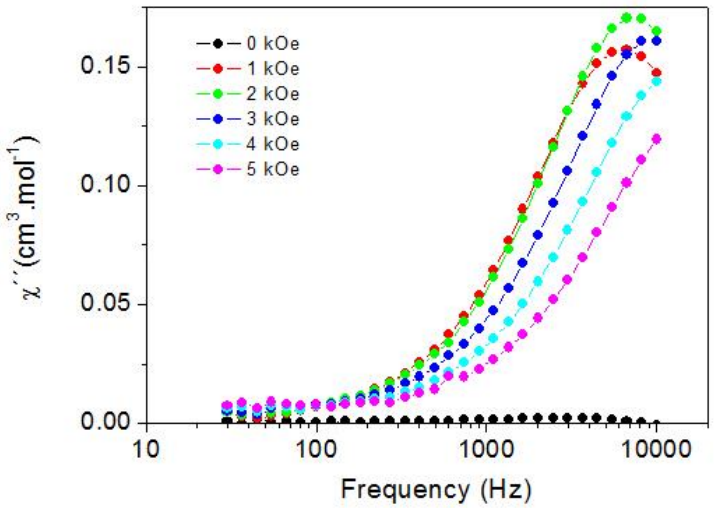

Figure 41: Frequency dependence of the out-of-phase ac magnetic susceptibility χ'' of **2**, at 3K, for different static magnetic fields.

In-phase and out-of-phase magnetic susceptibilities data were measured for temperatures ranging from 2-5K and are related in Figure 43. Cole-Cole plot semicircular shape is a signature of a single relaxation process for each temperature (Figure 44), as corroborated by the small values of α indicates a narrow distribution of relaxation times (Table A5). For a better understanding of the time and energy barrier for magnetization reversal, we select the best relaxation times (Table A5) from the local maximum of each temperature curve of out-of-phase magnetic susceptibility data and apply to Arrhenius law (Eq. 17), which gives us U_{eff} = 12.1(3) K and τ_0 = 5.52(4) × 10^{-7} s (Figure 45). As shown in Figures 45 and 46, the fit is in perfect agreement with the experimental data for the following parameters: A = 5600(100) $s^{-1}K^{-1}$, C = 730(20) $s^{-1}K^{-n}$, and n = 3.25(2).

$$\tau^{-1} = AT + CT^n \quad \text{(Eq. 17)}$$

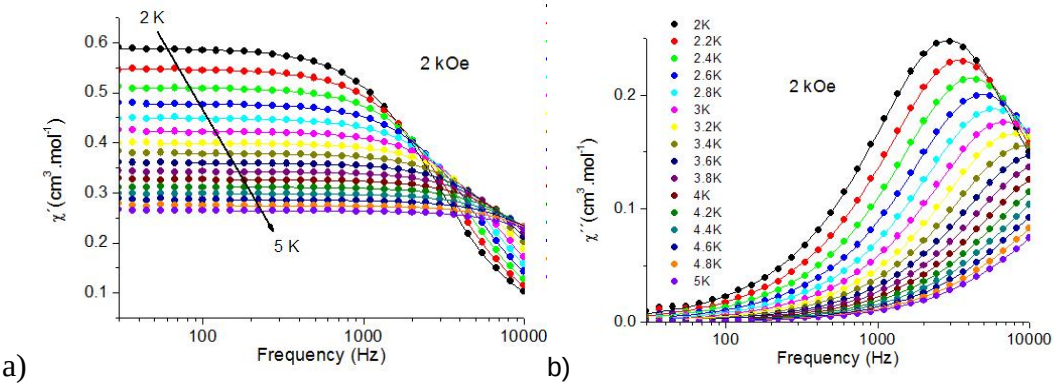

Figure 42: Frequency dependence at different temperatures of the in-phase (a) and out-of-phase (b) ac magnetic susceptibilities for **2**, under a static magnetic field of 2 kOe, at different temperatures. The solid lines correspond to the best fits by an extended Debye model.

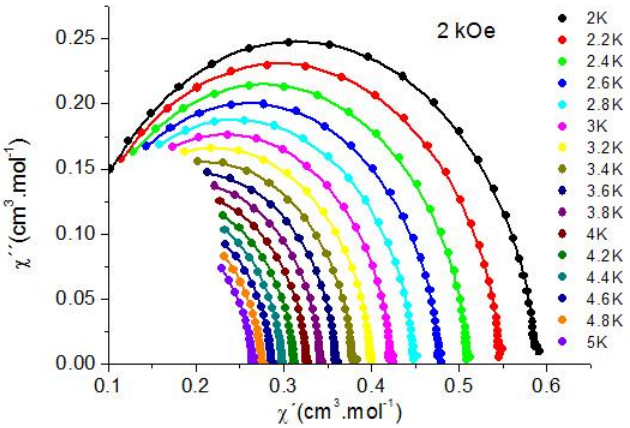

Figure 43: Cole-Cole plots of **2** at different temperatures, under a static magnetic field of 2 kOe. The solid lines correspond to the best fits.

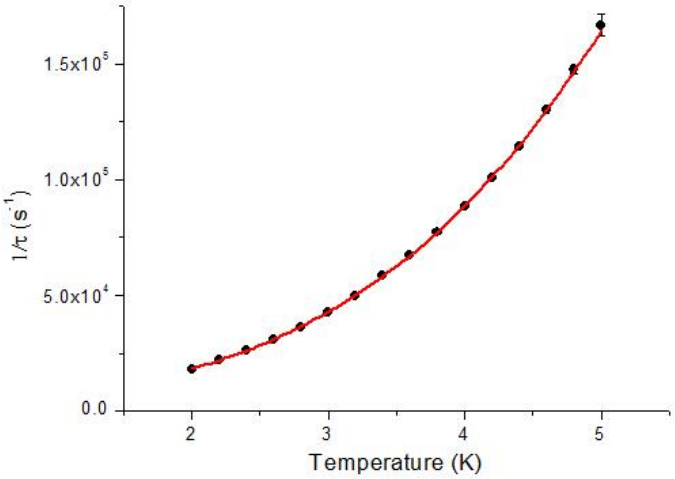

Figure 44: Inverse of the relaxation time versus temperature for **2**. The solid line corresponds to the best fit by Eq. 17.

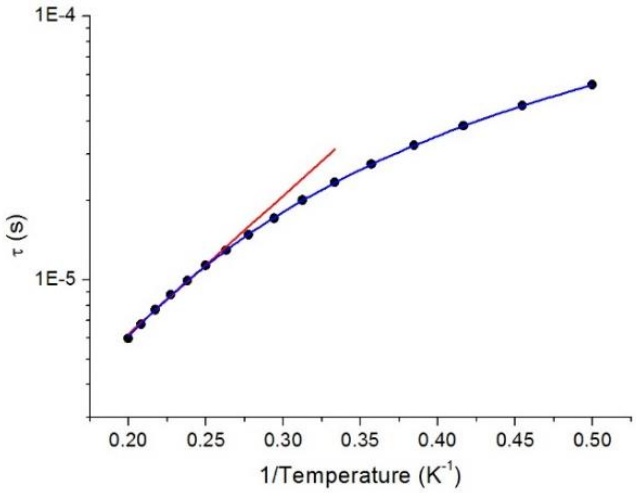

Figure 45: Arrhenius plot for **2** at 2 kOe. The red solid line corresponds to the best fit from Arrhenius's law (Eq. 6) for the highest temperatures, and the blue solid line corresponds to the best fit from Eq. 17.

With this information, we can conclude how **2** magnetic relaxation occurs. As discussed previously, no quantum tunneling is observed due to the suppression with the applied static magnetic field. Due to the obtained low energy barrier obtained, we can exclude the relaxation via the Orbach process since it involves transitions between real magnetic states, and no such levels exist below 150 cm^{-1}. A lower *n* value than expected for a Kramer ion (n = 9) [72] is commonly observed in octahedral cobalt-based compounds with SIM behavior, suggesting the contribution of acoustic and optical Raman processes [10,17,73–77] . With that, we can conclude that magnetic relaxation occurs via direct and Raman processes.

4.1.2

[Cu(HBTB)Dmdpy].2H_2O

For this complex, we utilized a system using H_3BTB as divergent ligand, but the auxiliary ligand was substituted from 1,10-phenanthroline to 5,5'-dimethyl-2-2'dipyridyl. The main objective in this section is to compare the influence of a different auxiliary ligand in both the complex's geometry, supramolecular arrangement and, as consequence, magnetic properties. In order to compare both systems, the same structural characterization was conducted (Infrared spectroscopy, thermogravimetric, single-crystal and polycrystal X-Ray diffraction). As only Cu^{2+} complex was obtained, only EPR and direct susceptibility measurements were conducted.

4.1.2.1

Structure characterization

4.1.2.1.1

Infrared spectroscopy

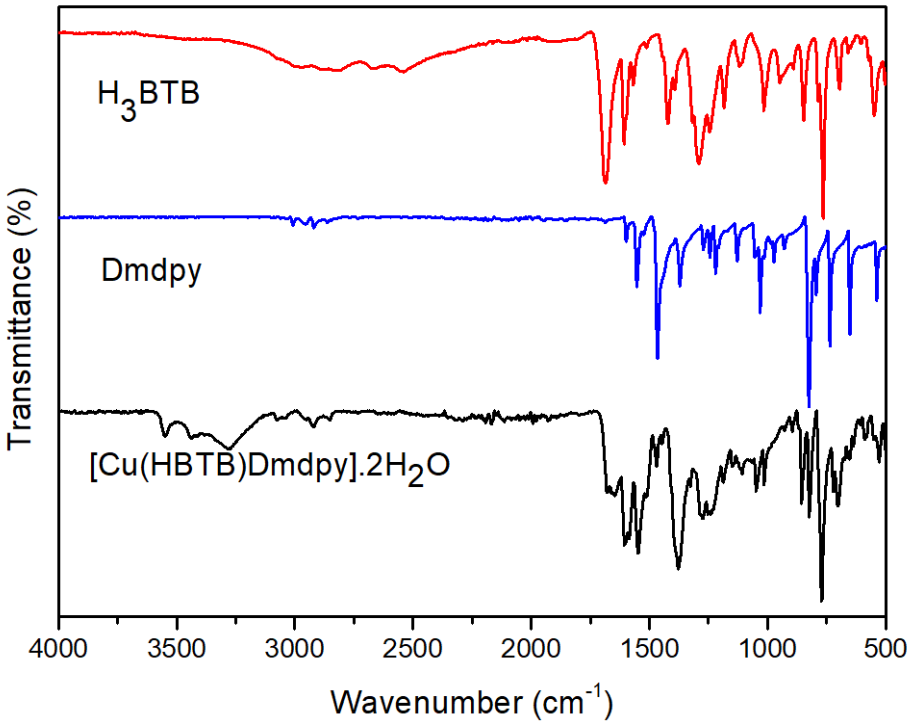

Figure 46: Infrared spectroscopy analysis of **3**.

IR spectra of the complex are displayed in Figure 46. It's observed the presence of three absorptions bands around 3550-3250 cm^{-1} that can be attributed to stretching vibrations of O-H from the water molecules present in the network. As for the $HBTB^{2-}$ we see a small shift related to the υ(C=O) from 1686 cm^{-1} in the free ligand to 1679 cm^{-1}, the appearance of two bands in 1605 cm^{-1} and 1547 cm^{-1} related to $\upsilon_{asim.}(COO^-)$ and an intense peak at 1376 from $\upsilon_{sim.}(COO^-)$, indicating not only the coordination of the polycarboxylate but also the deprotonation of a coordination site. The ancillary ligand coordination is usually inferred through the υ(CC/CN). However, due to the large number of bands in the same spectral region, we can infer the coordination through $\delta_{o.p}$(CH) deformation [78], where we see in the deformation peak at 824 cm^{-1} for both ligand and complex, indicating the presence of Dmdpy in the structure.

Table 6: Main infrared bands for free organic ligands and **3**.

Vibrational modes	H_3BTB	Dmdpy	**3**
ν_{O-H}	-	-	3548 cm^{-1}
ν_{O-H}	-	-	3440 cm^{-1}
ν_{O-H}	-	-	3284 cm^{-1}
$\nu_{C=O}$	1686 cm^{-1}	-	1679 cm^{-1}
$\nu_{asim.}(COO^-)$	-	-	1605 cm^{-1}
$\nu_{asim.}(COO^-)$	-	-	1547 cm^{-1}
$\nu_{sim.}(COO^-)$	-	-	1376 cm^{-1}
$\nu_{CC/CN}$	-	824 cm^{-1}	824 cm^{-1}

4.1.2.1.2

Structure description

Complex **3** crystallizes in a triclinic crystal system with space group P-1. Figure 47 exhibits the dinuclear structure of this complex. Each Cu(II) ion is involved in a distorted square pyramidal environment (Figure 47b), as evidenced by the trigonality index τ_5 = 0.03 [79]. The metal ions are coordinated to two nitrogen atoms (N1 and N2) from the dmdpy ligand and three oxygen atoms from two $HBTB^{2-}$ ligands (O1, O5, and O6). The $HBTB^{2-}$ ligand connects the metal ions in a syn-syn bridging mode. Additionally, this ligand exhibits two different coordination modes, syn-syn symmetric quelate (O5 and O6) and syn monodentate (O1). The dmdpy ligand exhibits its usual coordination mode, bidentate chelate.

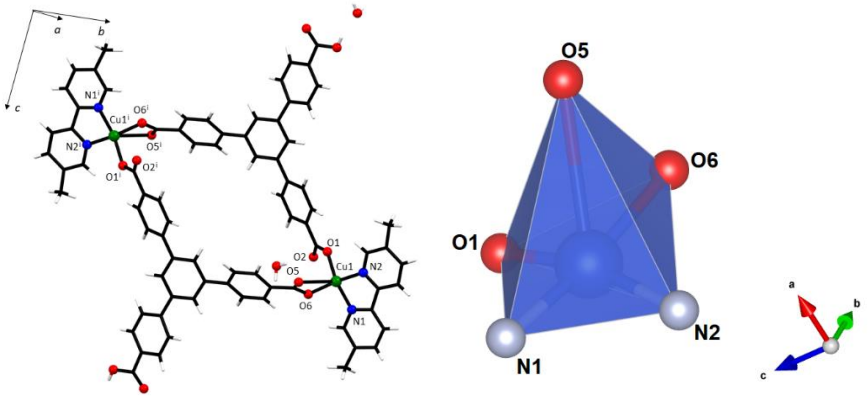

Figure 47: a) Molecular structure of the complex. b) Coordination environment of the cooper ion.

In the basal plane the bond distances are Cu1-N1 = 1.995(2) Å, Cu1-N2 = 1.976(2) Å, Cu1-O1 = 1.911(2) Å and Cu1-O6 = 1.944(2) Å. While in the apical position, the bond distance Cu1-O5 = 2.738(2) Å. The distance between the connected metal ions in the dimeric metallacycle is 16.489(8) Å.

Table 7: Selected bond distances and angles for complex **3**.

Bond distances (Å)		Angle(°)	
Cu1-N1	1.995(19)	N1-Cu1-N2	81.29(8)
Cu1-N2	1.976(19)	O6-Cu1-N1	164.15(8)
Cu1-O1	1.911(15)	O6-Cu1-N2	93.81(7)
Cu1-O5	2.738(2)	O1-Cu1-N1	92.66(8)
Cu1-O6	1.944(15)	O1-Cu1-N2	164.36(9)
Cu1-Cu1’	16.489	O1-Cu1-O6	95.63(7)

Figure 48 displays the main supramolecular interactions observed along the crystallographic axes b and c. The non-coordinated oxygen atoms from the carboxylate group of the HBTB2—ligand (O3 and O4) is responsible for an interaction between different cycles through H-bond interaction with the free H_2O molecules and the oxygen atom that did not coordinate with the metal ion (O2).

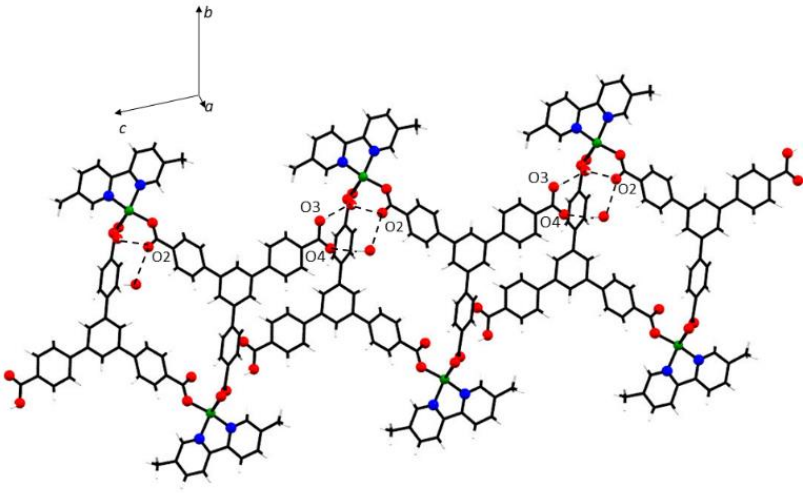

Figure 48: Supramolecular interactions through the crystallographic *a-axis* of the complex.

The principal intermolecular distances between Cu^{2+} are 7.7445(5)-15.4833(6) Å, supporting the idea of a very densely packed cycle that is bounded through π-π stacking and interactions with the free water molecules. As a result, a small surface area is present, a fact sustained by the almost-to-no solubility in many different solvents and the Thermogravimetric study.

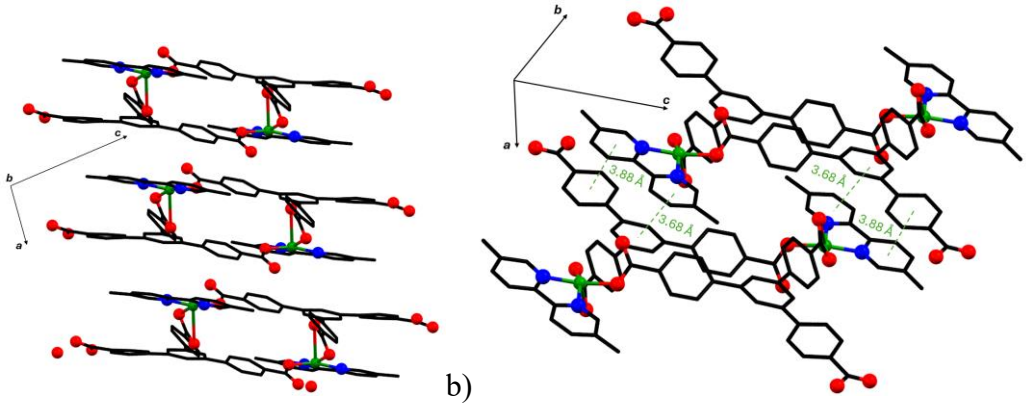

a) b)

Figure 49: a) Dimer stacking seen from crystallographic axys *b*. b) π-π stacking of the dimers.

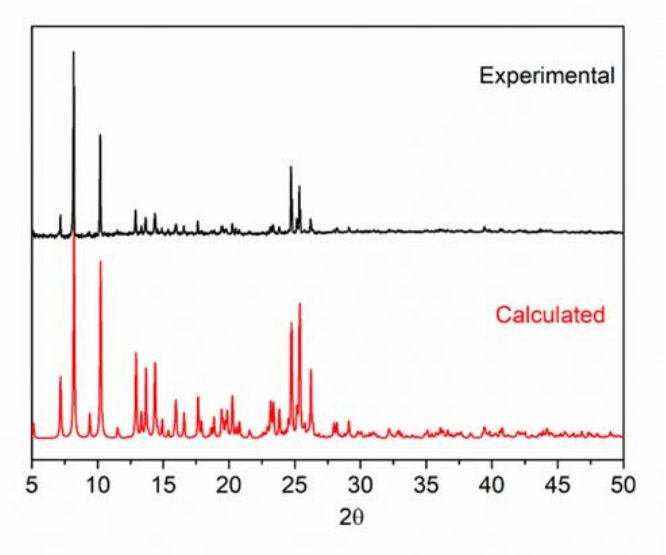

Figure 50: Powder pattern for the copper dimer.

Powder X-ray diffraction measurements were made for **3**. The experimental diffractogram was compared with the calculated one obtained from the structure solved by single crystal X-ray diffraction data. We can observe that the diffraction pattern from both data matches, indicating a good phase purity for the copper dimer.

4.1.2.1.3

Thermal analysis

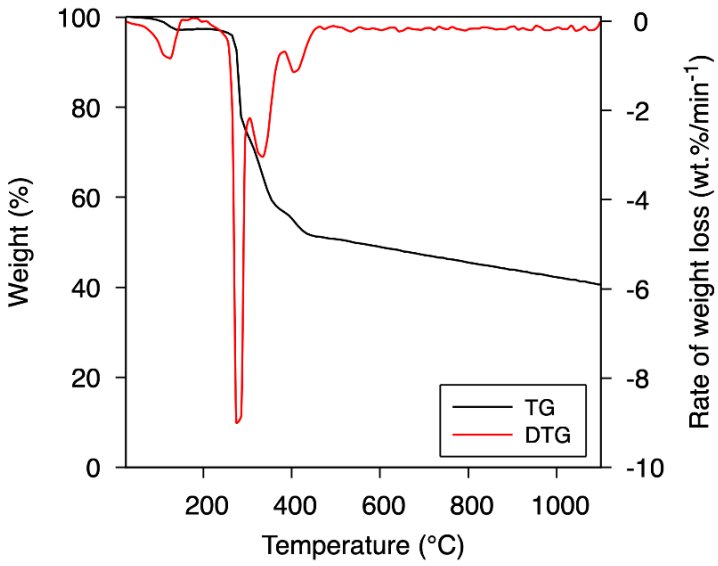

Figure 51: TG and DTG for **3**.

Thermogravimetric analysis (TGA) was performed on polycrystalline samples of complex **3** under a dynamic nitrogen atmosphere (Figure 51), where it is possible to see four weight loss events occurred. The first corresponds to the loss of the H_2O molecules inside the structure at around 100°C. The following step suggests the start of decomposition of the organic molecules between 277-408°C, which happens in three separate steps, totaling around 40% of weight loss. The remaining mass after heating to 1000°C is around 60%, indicating that the crystalline framework of the compound did not completely decompose.

4.1.2.2

Magnetic properties

An electron paramagnetic resonance (EPR) study was made for **3**, and it is shown in Figure 52.

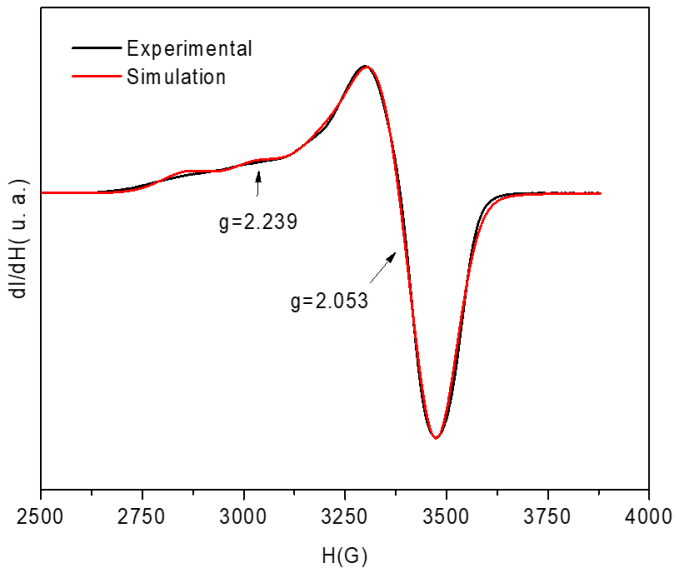

Figure 52: Powder EPR spectra (in black) recorded in derivative mode at 9.39 GHzand *T* = 300 K for **3**. The simulated spectrum is shown as a red line.

Due to the previously discussed low solubility of the complex in many solvents, EPR analysis was conducted in a crystal state. The *g* tensor reflects the local

symmetry of the system. The simulation resulted in two g-values ($g_{//}$ = 2.239 and $g\perp$ = 2.053) in the axial spectrum (Fig. 52). This value of g is typical for the dx2-y2 orbital of the unpaired electron ground state. It is associated with the N_2O_2 ligand set in the *xy* Cu^{2+} ion plane [80]. The g-factors' values are close to those reported for penta-coordinated copper dimers in the literature [81]. The hyperfine interaction in the parallel part of the spectrum was poorly resolved with a hyperfine constant of 172.10^{-4} cm^{-1}. This suggests that the Cu^{2+} centers are well isolated.

The isothermal magnetization of compound **1** was measured at 2K, 4K, and 8K with a magnetic field up to 7T (Figure 53). Considering the long distances between the copper ions within the crystal structure, no significant magnetic interaction is expected between the metal centers. Therefore, as a first attempt to reproduce the magnetic data, we only considered two identical Brillouin functions for the S=1/2 copper ions. The fitting procedure was performed regarding all temperatures simultaneously. The best fit, represented by the solid lines in Figure 53, was obtained with g = 2.09 ± 0.01 and is in very good agreement with the experimental data. Furthermore, the g parameter is consistent with the EPR measurements. Finally, as expected for isotropic non-interacting magnetic ions, the dependences of the magnetization in the function of the magnetic field over temperature (H/T) are superimposed for the different temperatures (Figure A4).

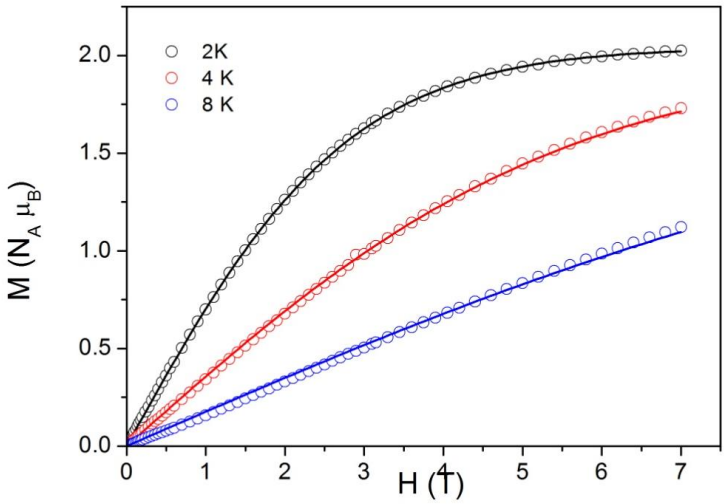

Figure 53: Magnetization measurements for **3**.

4.1.3

Conclusions

This section synthesized three new coordination compounds: two (**1** and **2**) being isomorph coordination polymers and one copper dimer (**3**). They were characterized with multiple techniques, with Single-crystal X-ray analysis showing both **1** and **2** being hexacoordinated, adopting a distorted octahedral geometry, with **3** being pentacoordinated with a distorted square pyramidal geometry.

For the Cu^{2+} CP, EPR was analyzed, but because it was analyzed in powder form, the characteristic hyperfine interactions for copper (II) were not entirely resolved. The Co^{2+} complex displayed antiferromagnetic interactions, exhibiting SIM-like behavior with slow relaxation of magnetization when a DC field was applied in order to suppress QTM.

The synthesis of **3** was a great example of the influence of auxiliary ligands in the synthesis of molecular magnetism. The change from Phen to Dmdpy ligand changed from a CP to a copper dimer metallacycle with intense intermolecular interactions, resulting in a low solubility for this complex. EPR and magnetization

measurements were conducted for this complex, which showed a small interaction between the Cu^{2+} ions in the structure.

4.2

Synthesis, characterization, magnetic, and luminescent properties of four coordination polymers involving Gd^{3+}, Dy^{3+}, Eu^{3+}, Tb^{3+}, and Coumarin-3-carboxylic acid.

4.2.1

$\{[LnCl_2(3\text{-}CCA)(H_2O)_3]H_2O\}_n$

In this section, a system utilizing 4 different Ln^{3+} ions and 3-HCCA ligand in a 1:1 ratio was obtained. Structure characterization was conducted through different techniques, such as infrared spectroscopy, thermogravimetry, single crystal and polycrystal X-Ray diffraction. Magnetocaloric studies were conducted for the Gd^{3+} derivate. Due to the high anisotropy in Tb^{3+} and Dy^{3+} ions, direct and alternate susceptibility measurements were conducted due. Both Eu^{3+} and Tb^{3+} complexes exhibited photoluminescence, and the excitation and emission spectrum for both CPs was obtained, as well as the emission lifetime was estimated.

4.2.1.1

Structure characterization

4.2.1.1.1

Infrared spectroscopy

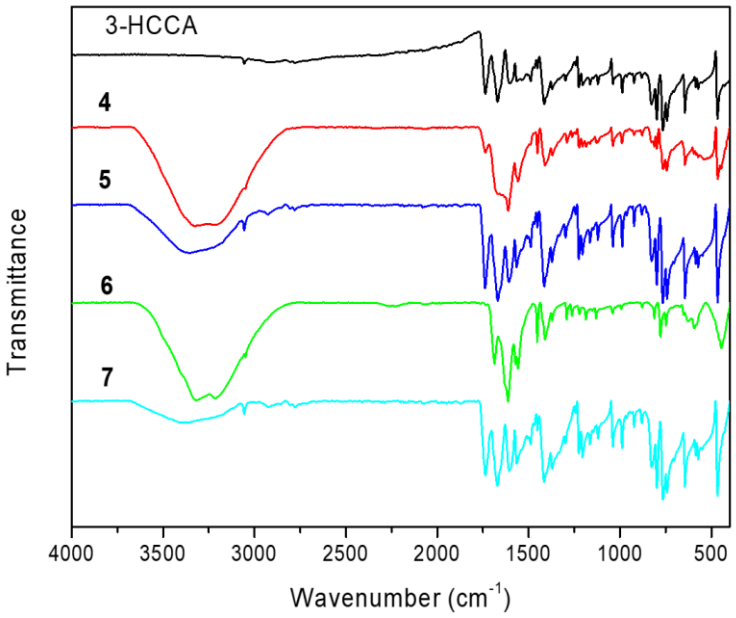

Figure 54: Infrared spectroscopy for $\{[LnCl_2(3\text{-}CCA)(H_2O)_3]H_2O\}_n$.

Infrared spectroscopy analysis was conducted for **4**, **5**, **6**, and **7** to visualize an indication of coordination due to a shift in the ligand's bands. Both complexes' spectrum was compared to the free 3-HCCA ligand. For complexes **5** and **7,** we can observe a prominent band characteristic of stretching vibrations of O-H from the water molecules present in the network; however, shift from the other vibrations from free organic ligand was not observed, likely due to the low % of the complex present in the sample (See Table 13 at Thermal Analysis section). For complexes **4** and **6,** we observe the significant stretching vibrations of O-H from the water molecules are much more intense due to the more significant % of the complex in the sample. Free 3-HCCA ligands coordinate through the C-O group. Therefore, the indication of complexation will happen around the 1800-1300 cm^{-1} range. The υ(C=O) band at 1736 cm^{-1} in the free ligand shifts to 1687 cm^{-1} for **6**, while for **4** we can observe a loss of intensity, with the appearance of two bands at 1668 and 1613 (**4** and **6**) cm^{-1} that are related to $\upsilon_{asim.}(COO^-)$, indicating not only the

coordination of the polycarboxylate but also confirming the deprotonation of a coordination site [78].

Table 8: Main infrared bands for free organic ligand, **4**, **5**, **6** and **7**.

Vibrational modes	3-HCCA	**4**	**5**	**6**	**7**
ν_{O-H}	-	3350 cm^{-1}	3350 cm^{-1}	3350 cm^{-1}	3350 cm^{-1}
$\nu_{C=O}$	1736 cm^{-1}	1736 cm^{-1}	1736 cm^{-1}	1687 cm^{-1}	1736 cm^{-1}
$\upsilon_{asim.}(COO^-)$	-	1668 cm^{-1}	-	1668 cm^{-1}	-
$\upsilon_{asim.}(COO^-)$	-	1613 cm^{-1}	-	1613 cm^{-1}	-

4.2.1.1.2

Structure description

Table A3 displays crystal data and refinement results for all coordination polymers. Figure A5 shows Ortep images of the asymmetric units of all complexes. All complexes are isostructural, and their fragments and coordination environments are displayed in Figure 55.

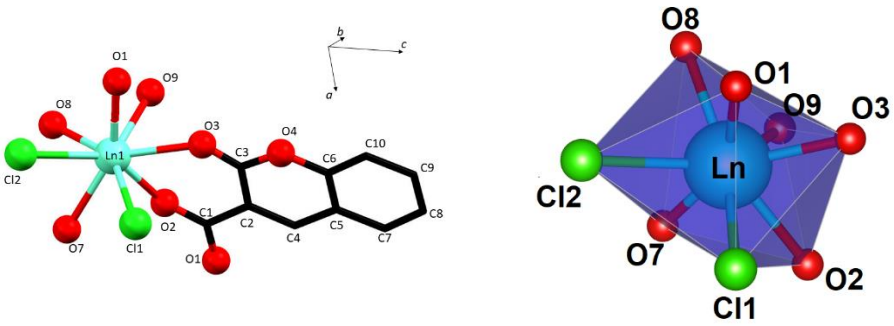

a) b)

Figure 55: a) Fragment of the coordination polymers. b) Polyhedral representation of the coordination environment of lanthanide ions (hydrogens, solvent and counterions were omitted for the sake of clarity).

The lanthanide ions are octacoordinated, with these ligands being two chloride ions, three oxygens coming from water molecules, and three other oxygens coming from two Coumarin-3-carboxylic acids, adopting a triangular dodecahedron geometry (Shape Program). Although all coordination polymers have the same coordination environment, they have slight deviations in angles and bond distances, as shown in Tables 9 and 10.

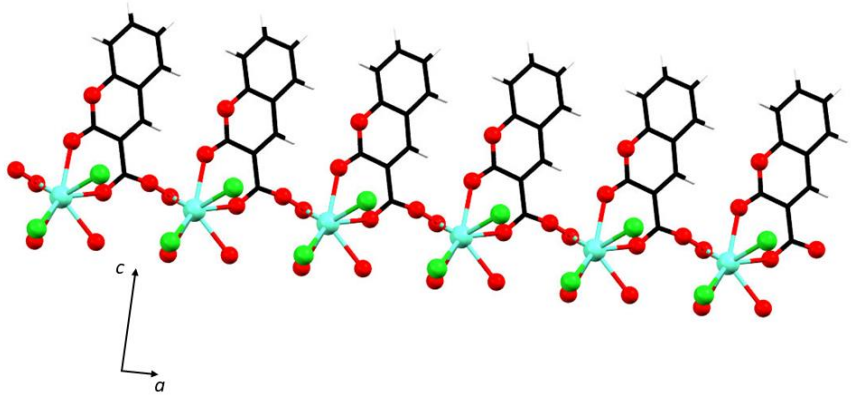

Figure 56: Extention of the polymeric chain seen through crystallographic axis *b*.

Table 9: Bond distances for $\{[LnCl_2(3\text{-}CCA)(H_2O)_3]H_2O\}_n$.

Bonds distance (Å)	Ln = Eu	Ln = Gd	Ln = Tb	Ln = Dy
Ln-Cl1	2.736(9)	2.727(7)	2.714(9)	2.705(1)
Ln-Cl2	2.862(1)	2.864(9)	2.861(1)	2.853(2)
Ln-O1	2.311(3)	2.290(2)	2.228(3)	2.270(3)
Ln-O2	2.353(3)	2.335(3)	2.327(4)	2.321(4)
Ln-O3	2.487(3)	2.465(3)	2.461(3)	2.444(3)
Ln-O7	2.469(3)	2.440(2)	2.425(3)	2.410(4)
Ln-O8	2.401(3)	2.378(2)	2.355(3)	2.349(3)
Ln-O9	2.486(3)	2.462(3)	2.425(3)	2.440(3)

Table 10: Main angles found in the coordination environment for $\{[LnCl_2(3\text{-}CCA)(H_2O)_3]H_2O\}_n$.

Bond angles (°)	Ln = Eu	Ln = Gd	Ln = Tb	Ln = Dy
Cl1-Ln-Cl2	80.19°	79.76°	79.73°	79.59°
O1-Ln-O9	73.15°	73.71°	73.54°	73.85°
O1-Ln-O3	73.62°	73.45°	73.52°	73.53°
O1-Ln-O8	94.41°	94.00°	93.27°	93.49°
O2-Ln-O3	69.72°	70.30°	70.65°	71.11°
O2-Ln-O7	69.80°	69.69°	69.78°	69.60°
O2-Ln-O9	75.84°	75.84°	75.84°	75.62°
O7-Ln-O8	73.33°	73.67°	73.76°	73.43°

Table 11: Shortest Ln-Ln distances found for $\{[LnCl_2(3\text{-}CCA)(H_2O)_3]H_2O\}_n$.

Intrachain Ln-Ln distance (Å)	Ln = Eu	Ln = Gd	Ln = Tb	Ln = Dy
Ln-Ln	6.4287(4)	6.4119(4)	6.3967(3)	6.3891(5)
Interchain Ln-Ln distance (Å)	**Ln = Eu**	**Ln = Gd**	**Ln = Tb**	**Ln = Dy**
Smallest distance	7.0855(4)	7.0230(5)	6.9561(5)	6.9533(6)

Lanthanide ions are linked by the carboxylate part of the coumarin molecule, as they act as a bridge through both O2 and O3 atoms. In this way, the coordination polymer extends along crystallographic axis *a*, as shown in Figure 56. As there is only a carboxylate bridge between the metal ions, its intrachain distance is relatively small, ranging from 6.38 to 6.43, as reported in Table 11. Each

coumarin molecule from the asymmetric unit interacts with itself via intrachain H-bond (Fig. 57), where the distances found in each CP are in Table 12.

Table 12: non-classic intrachain H-bond distance in CP family.

O3···H4-C4	D-H (Å)	H···A (Å)	D···A (Å)	D-H···A (°)
Ln = Eu	0.930	2.376	3.295	169.33
Ln = Gd	0.964	2.323	3.272	167.91
Ln = Tb	0.975	2.292	3.260	171.26
Ln = Dy	0.869	2.395	3.253	168.95
O4···H7-C7	D-H (Å)	H···A (Å)	D···A (Å)	D-H···A (°)
Ln = Eu	0.930	2.592	3.484	161.04
Ln = Gd	0.972	2.544	2.457	156.62
Ln = Tb	0.915	2.610	3.454	153.73
Ln = Dy	0.917	2.604	3.453	154.31

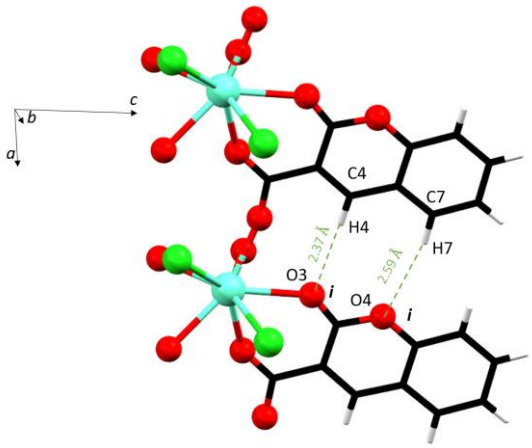

Figure 57: Intrachain H-bond distance from the polymeric chain. Symmetry codes: (i) x+1, *y*, *z*.

As for interchain interactions, we observe classic and non-classic H-bonds between the free and coordinated H_2O molecule, the coordinated Cl atoms, and the O atoms from the HCCA ligand. These interactions are found in all CPs with a slight difference in the distance for each polymer. This interaction is the main reason we find small interchain distances between Ln core centers since these

interactions create agglomerates described in Figure 58 (b) that go through the entirety of the polymeric chain. Another interchain interaction is π-π stacking of the aromatic rings from the coumarin molecule. Fig. 59 a) displays these stackings, and Fig. 59 b) shows both interchain interactions simultaneously.

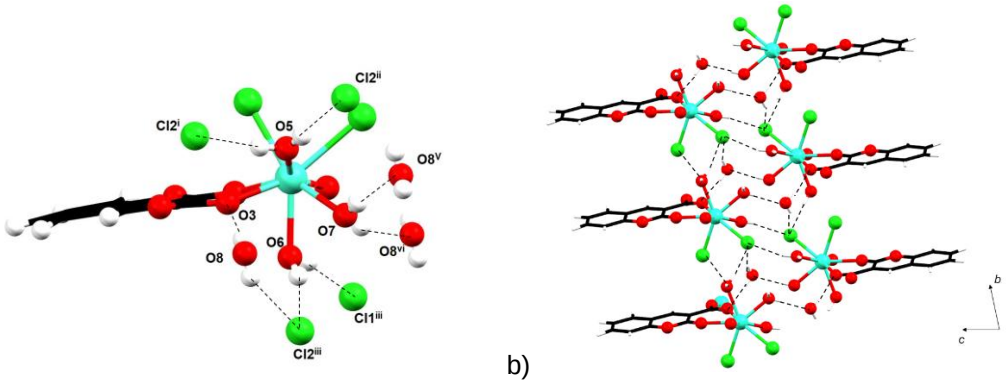

a) b)

Figure 58: a) H-bond interaction around the metal center. b) Interchain H-bond seen from crystallographic axis *a*. Symmetry codes: (i) *x*-1, *y*, *z*; (ii) -*x*+2, -*y*+2, -*z*+2; (iii) *x*, *y*-1, *z*; (v) -*x*+2, -*y*+1, -*z*+2.

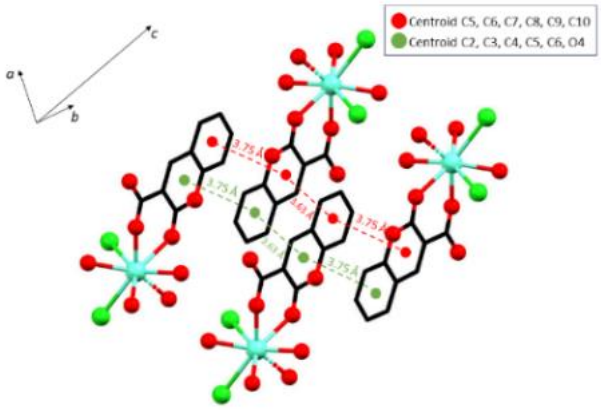

a)

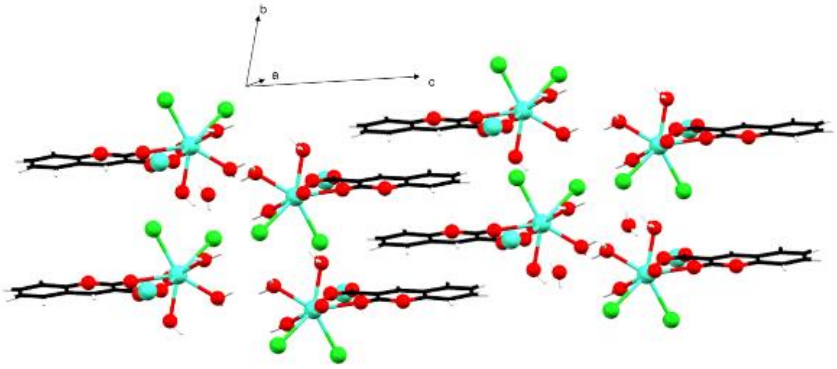

b)

Figure 59: a) Stacking of the aromatic rings from HCCA ligand. b) Both interchain interactions are found in this family of CP.

Powder X-ray diffraction measurements were made for **4**, **5**, and 6 and are displayed in Figure 60. The experimental diffractogram was compared with the calculated one obtained from the structure solved by single crystal X-ray diffraction data.

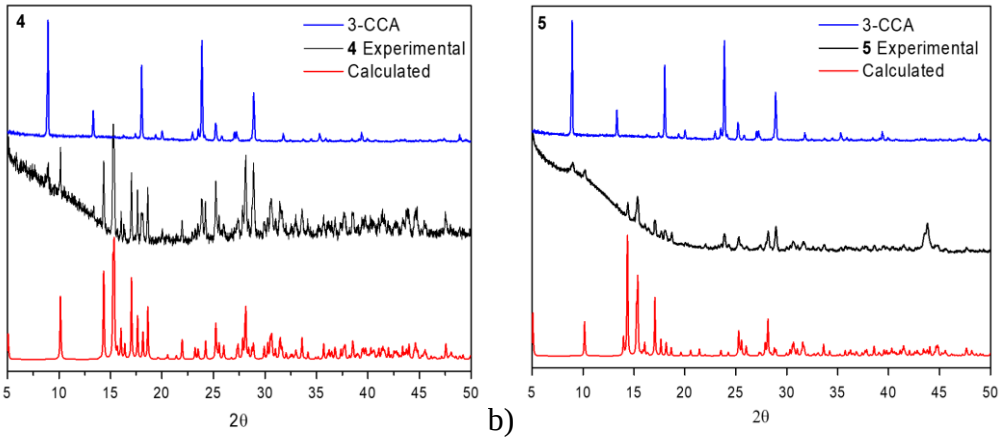

a) b)

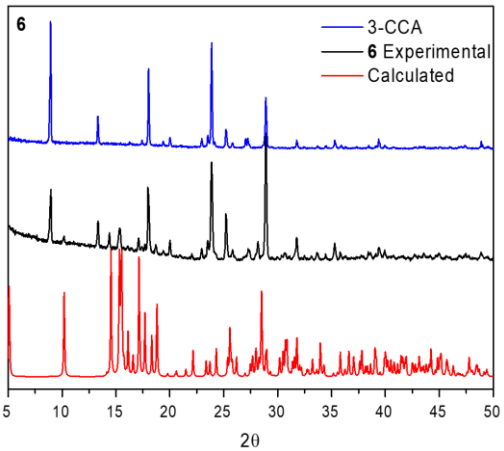

c)

Figure 60: Powder X-ray diffraction measurements for: a) **4**. b) **5**. c) **6**.

The experimental diffraction pattern for all complexes matches some peaks from the calculated data. However, we can observe the presence of the organic ligand 3-CCA crystallized alongside the complex. Although organic ligands do not interfere with magnetic properties (diamagnetic impurities can be corrected), they result in a mass error that reduces the magnetic signal, as will be discussed in this dissertation. The purification of these complexes is still in progress for the paper's publication.

4.2.1.1.3

Thermal analysis

Thermogravimetric and Derivative thermogravimetric analyses were performed on polycrystalline samples for the four polymers under a dynamic nitrogen atmosphere (Fig. 61). We can observe three to four weight loss events for all polymers. The first event usually happens at around 80-100°C, which we can attribute to the loss of the free H_2O molecules in the crystalline structure. The second weight loss step happens at approximately 160-200°C and is related to the coordinated H_2O molecules on the structure. Later, for all four complexes, we see a significant weight loss event that happens at around 230°C. However, we can observe that the complex containing Eu does not have a considerable weight loss event compared to the remaining three. In fact, for the Eu complex only, we can observe another later weight loss event happening at around 380°C, corresponding to the coordinated loss of both Cl atoms. Analyzing the remaining percentage of mass for all complexes, we can observe a smaller obtained mass than what was previously expected (Table 13), which was around 30-40%, due to the expected formation of either $Ln_{(s)}$, Ln_2O_3 or even LnO for lanthanides such as Eu that can exhibit +2 oxidation state. This indicates that the sample carried to the thermal

analysis was not entirely pure; crystallized HCCA molecules that were not coordinated were present and majorly decomposed at around 230°C, explaining the significant weight loss event in all polymers. Only complexes **6** and **7** reached thermal stability, so for the Dy sample we can estimate the amount of complex contained in the sample (Table 13), while for the other two complexes we cannot fully estimate, since they did not reach thermal stability.

We can observe the influence of this small % of the complex in the samples in magnetic studies that were conducted and are reported in Section 3.1.4, where we can observe smaller values of magnetization as were previously expected. This happens since magnetization values are based on the molar mass of the compound. Therefore, when the mass of the sample is reported and then measured, the magnetization value is not as high as it should be (Table 1) since there is an organic ligand in the sample.

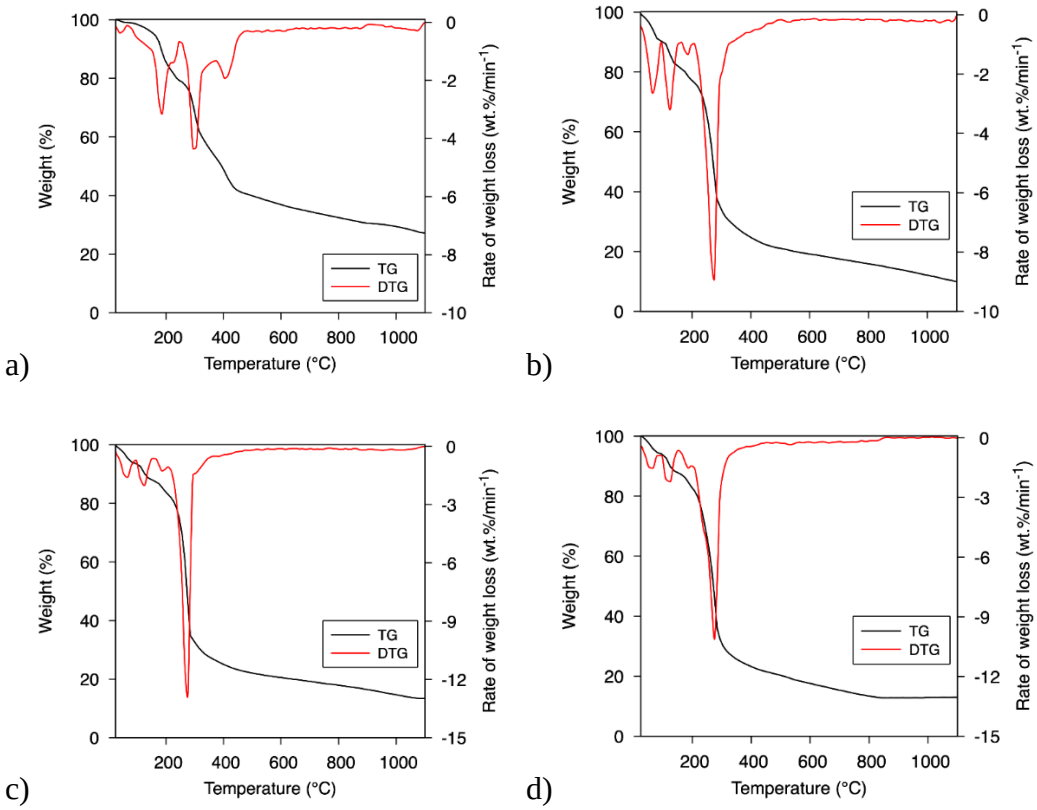

Figure 61: TGA analysis for a) **4**; b) **5**; c) **6**; d) **7**.

Table 13: Percentage of remaining mass for all complexes.

	Eu	Gd	Tb	Dy
Obtained %	27	11	18	13
% of the complex in the sample	-	-	48.32	34.48

4.2.1.2

Photoluminescent properties

Due to the unique photoluminescence properties of Eu^{3+} and Tb^{3+}, the photoluminescent properties of both $[EuCl_2(3\text{-}CCA)(H_2O)_3]H_2O_n$ and $[TbCl_2(3\text{-}CCA)(H_2O)_3]H_2On$ were investigated. When exposed to UV radiation, the Eu complex emitted a red color, but the Tb complex did not show a green emission with a commercial UV-light lamp.

The emission and excitation spectra for **4** is shown in Figure 62. The excitation spectra (blue color) were registered (250-500 nm), with the emission monitored in the intense $^5D_0 \rightarrow {}^7F_2$ (λ_{emi} = 614 nm) transition. We can observe an intense and large band from 250-400 nm, attributed to the absorption energy from the ligand's aromatic rings $S \rightarrow S_0$ (π, π^*). We can also observe a fine band $^7F_0 \rightarrow {}^5D_2$ corresponding to 4f – 4f transitions of Eu^{3+} ion.

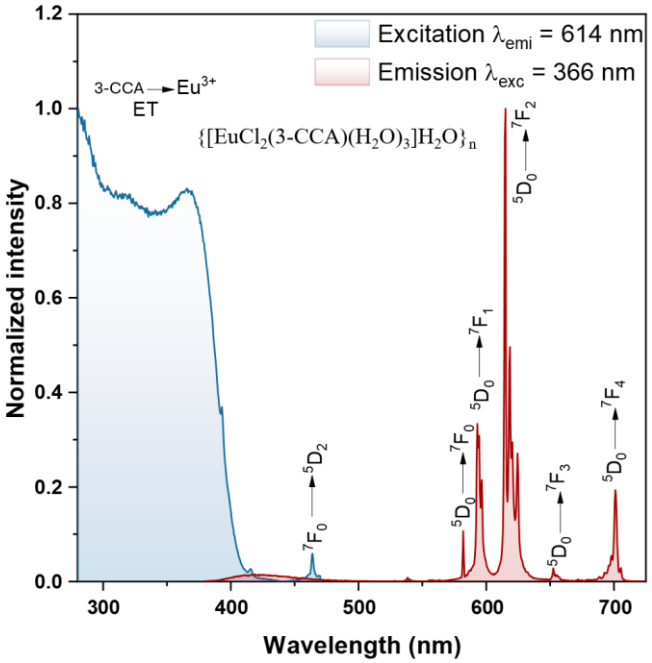

Figure 62: Emission and excitation spectra of **4** (experiment conducted in crystalline form).

The emission spectra (color red) were registered in the interval of (375-750 nm) with the excitation fixed at the highest absorption from the 3-CCA ligand (λ_{exc} = 366 nm). The complex emits many characteristic bands for Eu^{3+}ion, from its main emission state $^5D_0$ to ^7F_J, with J = 0, …, 4. The transition $^5D_0 \rightarrow {}^7F_0$ in one band indicates that all the Eu^{3+}ions are experiencing a uniform crystalline field.

For the Tb^{3+}complex, the excitation and emission spectra are displayed in Figure 63. The excitation spectra (blue color) were registered at 300-525 nm, with the emission monitored in the intense $^5D_4 \rightarrow {}^7F_5$ (λ_{emi} = 545 nm) band. We can observe the same large band from 300-375 nm corresponding to the absorption energy from the ligand $S \rightarrow S_0$ (π, π^*). However, differently from the Eu^{3+}complex, we can observe another band later at around 410 nm, which is also present in the emission spectrum (green color); that is an indication that the transfer of energy from the 3-CCA^- was not effective, that is, the antenna effect was not prevalent,

which can explain the lack of green emission when excited with a regular UV light lamp.

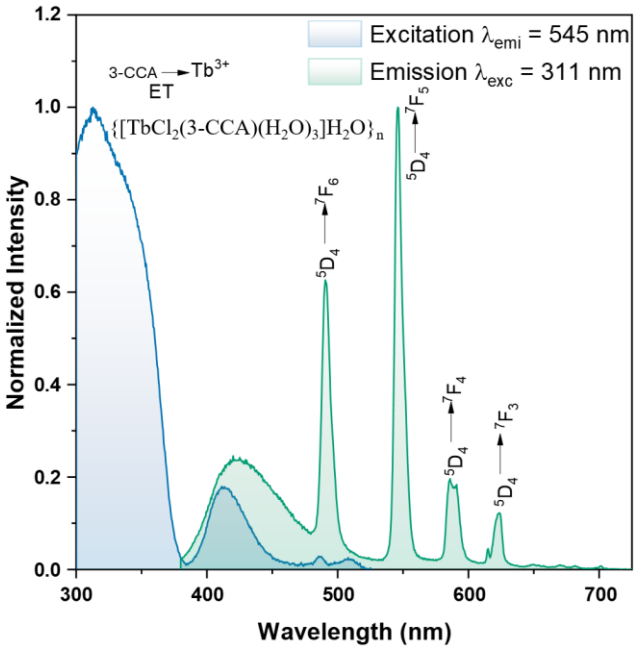

Figure 63: Emission and excitation spectra of **6** (experiment conducted in crystalline form).

The emission spectra were registered at 375-725 nm, with the λ_{exc} = 311 nm being the highest absorption found for the organic ligand. We can observe that in these spectra, differently than the Eu^{3+}spectra, we can hardly see the Stark levels, as the bands tend to be larger for Tb^{3+}ions since both of their fundamental state $^7F_6$ and their excited state $^5D_4$ are degenerated. As previously discussed, we observed the large band, indicating that the antenna effect was not prevalent. We can also observe several characteristic bands from the Tb^{3+}ion involving the main emission state for the lanthanide, $^5D_4 \rightarrow {}^7F_J$ with J = 3, …, 6.

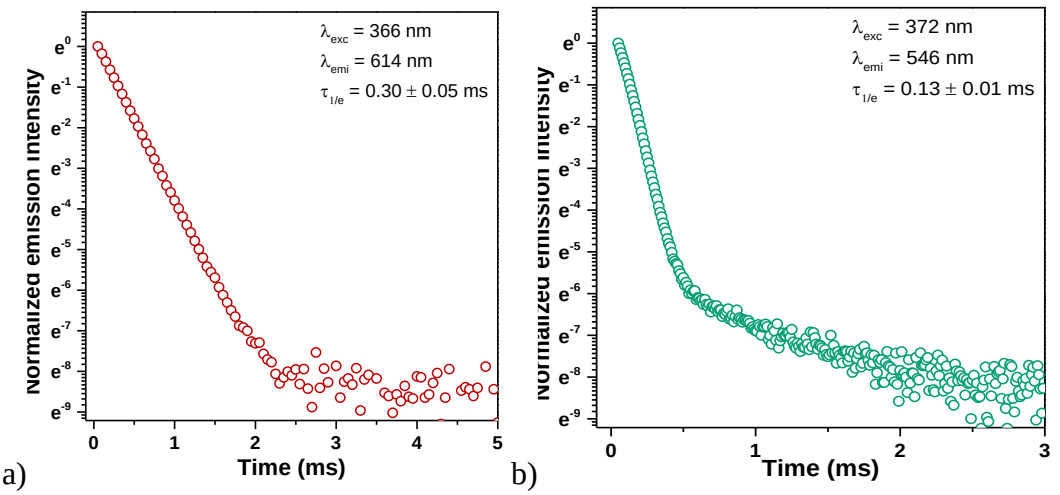

Figure 64: Half-life analysis of a) **4** b) **6**.

The transition involving the emission state $^5D_0$ for the Eu^{3+}complex and $^5D_4$ for the Tb^{3+}complex was selected to analyze the complex's emission lifetime. The first was excited at 366 nm, and their emissions were monitored in the maximum emission wavelength (614 nm), while the latter was excited at 372 nm, with the emission at 546 nm. We can observe that the emission lifetime for the Tb^{3+}complex is smaller than literature values [82][83] and is smaller than the Eu^{3+} one. This is more evidence that the antenna effect was not prevalent for the Tb^{3+}complex since the opposite was expected due to the difference of energy of the emission state and fundamental state for Tb^{3+} ($^5D_4 \rightarrow {}^7F_6$) being higher than the one for Eu^{3+} ($^5D_0 \rightarrow {}^7F_0$).

4.2.1.3

Magnetic properties

4.2.1.3.1

{[$GdCl_2$(3-CCA)(H_2O)$_3$]H_2O}$_n$.

A magnetocaloric effect study was conducted for **5** because Gd^{3+} presented no hysteresis curve. Magnetization measurements were performed at a field of 0-9 T in the temperature range of 1.8-10K (Figure 65). We can observe a continuous increase in magnetization with the field increase, coming up to a value of around 4 Nβ. When comparing this value to other Gd-based materials in the literature, the obtained value is smaller (the expected value for one spin-only Gd^{3+} being 7 Nβ). This error might be caused by the presence of the organic ligand in the sample affecting the mass sample error or the temperature-independent paramagnetism (TIP) effect.

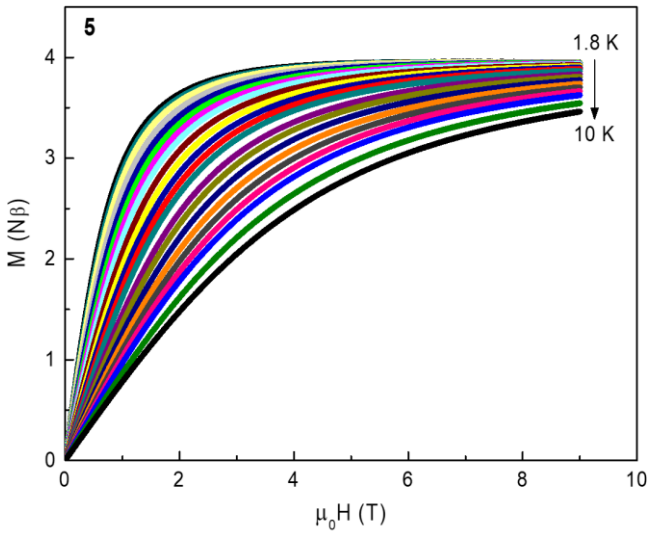

Figure 65: Magnetization measurements for **5**.

The ΔS value was obtained for different applied fields using Maxwell equation Eq. 14, and Figure 66 displays the graphs of ΔS vs. T and ΔS vs. H.

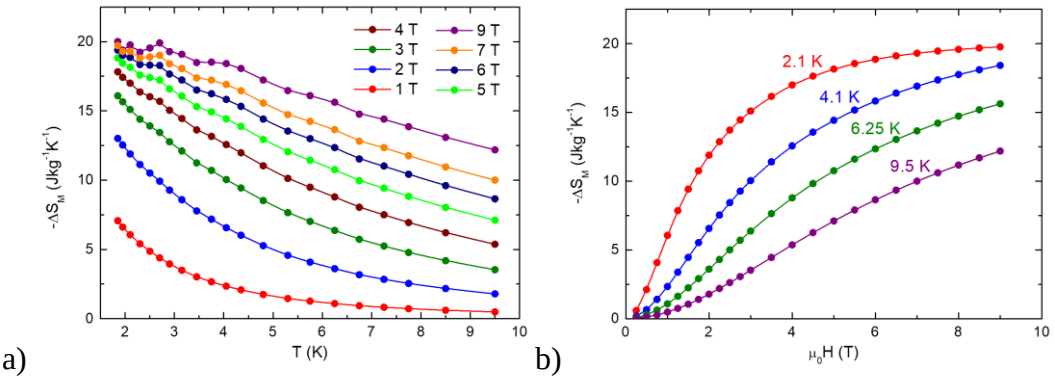

a) b)

Figure 66: Maximum entropy variation for **5**.

As observed in both graphs, the ΔS_M^{Max} obtained was around 20 $Jkg^{-1}K^{-1}$ at 2.1 K with an applied field of 9T. The theoretical value obtained by: $\Delta S_M^{Max} = Rln(2S+1)/M_w$, when using S = 7/2 and a molecular weight of 489.35 g/mol, the expected value is 35.3 $Jkg^{-1}K^{-1}$. This theoretical value agrees with the values found in the literature [84][85], but the smaller obtained value can be attributed to the mass error previously discussed.

4.2.1.3.2 {[TbCl$_2$(3-CCA)(H$_2$O)$_3$]H$_2$O}$_n$.

Direct current magnetic susceptibility data was measured for **6** from 2-350 K and is displayed in Figure 67 a). We can observe the χT value at 3.88 $cm^3K.mol^{-1}$ decreases its value with the decrease in temperature up until 8K due to the Stark level's depopulation, where it hits a value of 3.1 $cm^3K.mol^{-1}$ and increases upon cooling, reaching 3.13 $cm^3K.mol^{-1}$ at the 3K mark. This increase in χT value at low temperatures might be due to temperature-independent paramagnetism (TIP), from the sample's sample holder.

The obtained χT value was way smaller than the expected value for the free ion approximation of an uncoupled Tb^{3+} ion ($\chi_M T$ = 11.82 $cm^3.K.mol^{-1}$) (Table 1). Due to this, computational CASSCF calculations were conducted on this family of

compounds, where Fig. 67 b) shows the calculated χT value for **6** of 11.66 $cm^3K.mol^{-1}$, a value that is much closer to the expected value.

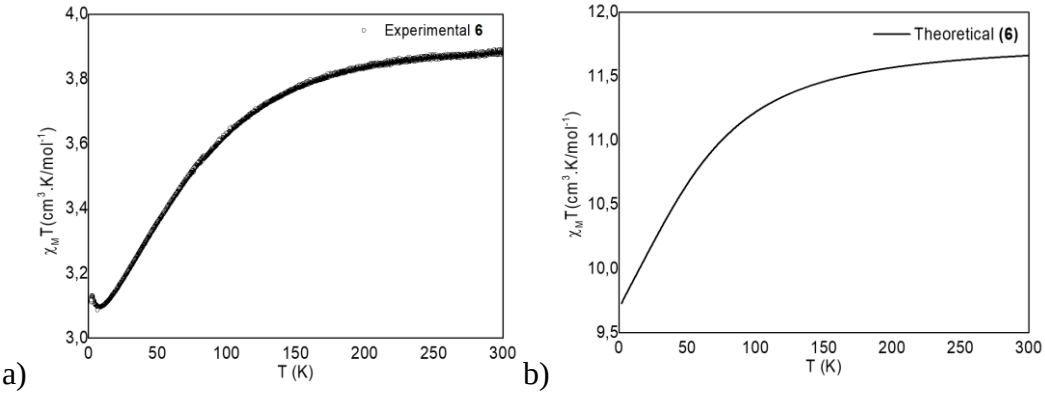

a) b)

Figure 67: a) χ_MT measurement for **6.** b) CASSCF calculation for χ_MT for **6.**

CASSCF calculation is an *ab initio* form of calculation frequently used to help understand magnetic data. They were conducted for **6**, and Table 14 shows the energy levels of the electronic states of Tb^{3+} ion for **6**. Due to their accessible energy states, only the first 12 energy states have a Boltzmann population relevant for magnetic properties. After that, there is a massive increase in energy value, which characterizes high anisotropy for **6**.

Table 14: Electronic state energy levels calculated from CASSCF calculation for **6**.

Tb^{3+} (6)	
State	Energy (cm^{-1})
1	0
2	0.10
3	120.31
4	123.40
5	137.32
6	143.11
7	194.79
8	213.01
9	250.83
10	296.24
11	312.22
12	394.95
13	2250.14

Tb^{3+}-based coordination compounds can behave as SMMs due to their high anisotropy. Therefore, alternating-current susceptibility measurements of the complex were conducted. The in-phase and out-of-phase measurements are displayed in Figure 68. Firstly, it evaluated the best static magnetic field to conduct a slow relaxation of magnetization study. With an alternating field of H_{ac} =10 Oe, the in-phase and out-of-phase signals were evaluated by applying different background static fields ranging from 0-4kOe. As observed in Figure 68, the

background field that resulted in the best χ' signal was 1 kOe and 1.5 kOe, and the ones that resulted in the best χ'' signal were 1.5 kOe and 2 kOe. With that, 1.5 kOe was the best-selected field for further analysis.

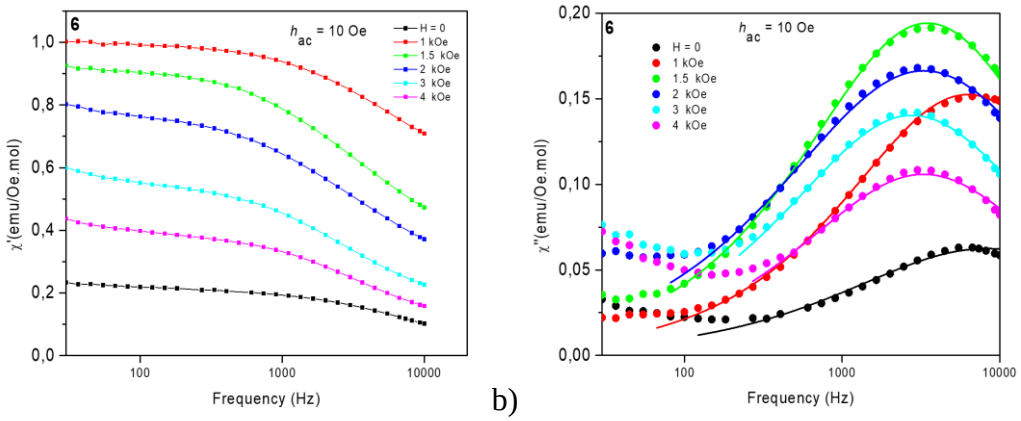

a) b)

Figure 68: a) In-phase *ac* measurements for **6**. b) Out-of-phase *ac* measurements for **6**.

Purification processes are in progress since further analysis is needed to determine the energy barrier, the relaxation time, and the mechanism of relaxation due to the small signal obtained by organic ligands in the samples. However, Fig 68 b) shows us out-of-plane frequency-dependent signals that indicate the slow relaxation of magnetization in **6**.

4.2.1.3.3 {[DyCl$_2$(3-CCA)(H$_2$O)$_3$]H$_2$O}$_n$.

Direct current magnetic susceptibility data was measured for **7** at a 2-350 K temperature range, as shown in Figure 69. We can observe a $\chi_M T$ value of 9.55 cm^3Kmol^{-1}, with a gradient reduction in the $\chi_M T$ with the decrease of temperature reaching a value of 5.38 cm^3Kmol^{-1} at 2K. This result is associated with the depopulation of the Stark levels for Dy^{3+} ions. Compared to the literature and tabulated data, the obtained $\chi_M T$ is smaller than expected (~14 cm^3Kmol^{-1}).

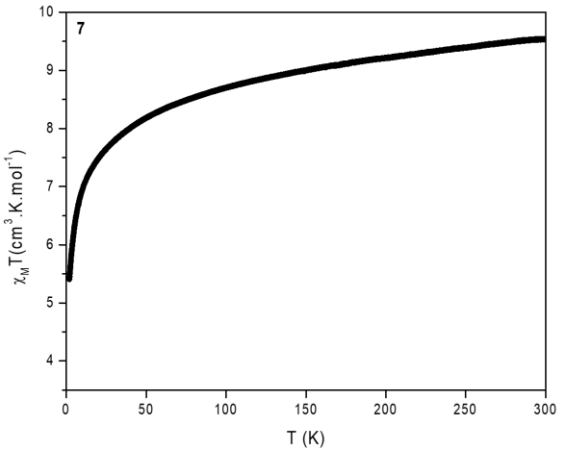

Figure 69: $\chi_M T$ measurements for **7** at 1kOe.

Just like Tb^{3+} ions, Dy^{3+}-based compounds can behave as Single Molecule Magnets. Therefore, dynamic magnetic studies were conducted. Figure 70 shows us in-phase (a) and out-of-phase (b) magnetic measurements vs temperature at different applied fields. We can observe the presence of maximum values at the field range of 1 kOe – 1T for the out-of-phase at a fixed frequency of 1 kHz. This indicates the slow relaxation of magnetization present in this compound; however, further analysis is required to determine the relaxation time and the energy barrier for the magnetization reversal.

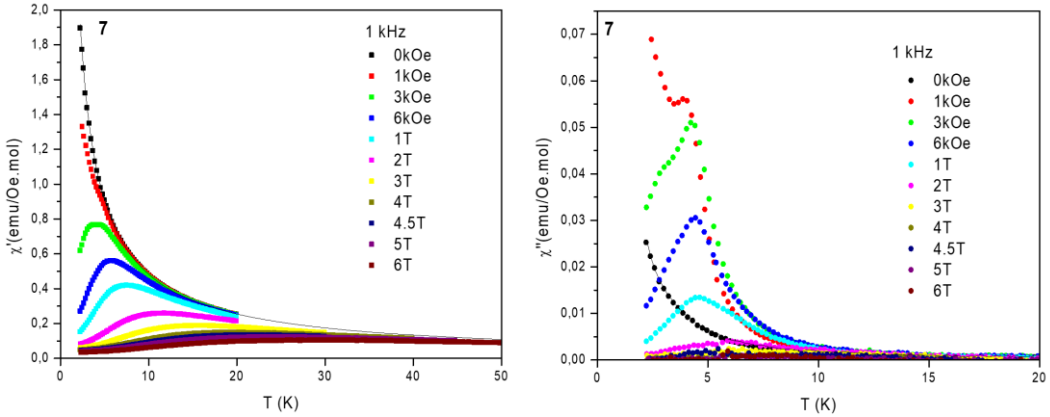

Figure 70: a) In-phase *ac* measurements for **7**. b) Out-of-phase *ac* measurements for **7**.

4.2.2

$\{[Ln(3\text{-}CCA)_3(H_2O)_2](H_2O)_2\}_n$

In this section, a different system was obtained utilizing 4 different Ln^{3+} ions and 3-HCCA ligand, but with a different Ln:3-HCCA ligand ratio, where in the previous family a 1:1 ratio was obtained, and in this section a 1:3 ratio was obtained. To compare both family properties, the same structure characterization was conducted (infrared spectroscopy, thermogravimetry, single crystal and polycrystal X-Ray diffraction). Both Eu^{3+} and Tb^{3+} complexes exhibited photoluminescence, and their excitation and emission spectrum and the emission lifetime for both CPs was obtained and compared to the previous family.

4.2.2.1

Structure characterization

4.2.2.1.2

Infrared spectroscopy

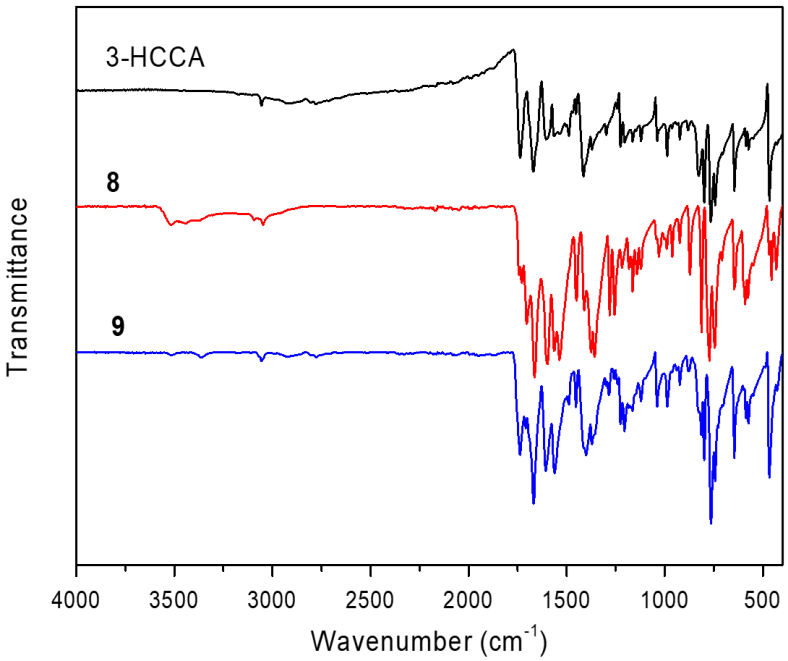

Figure 71: Infrared spectroscopy for **8** and **9.**

Infrared spectroscopy analysis was conducted for **8** and **9** to visualize an indication of coordination due to a shift in the ligand's bands. Both complexes' spectrum was compared to the free 3-HCCA ligand. The behavior of these spectra is similar to the ones found in **4** and **6**. We can observe weak bands at 3519 and 3441 cm^{-1} due to H_2O molecules in the structure, with the υ(C=O) band at 1736 cm^{-1} in the free ligand shifting to lose intensity in **8**, with the appearance of a band at 1704 cm^{-1} for both complexes that can be attributed to a shift in υ(C=O). However, the presence of the band still in 1736 cm^{-1} for **9** can indicate the presence of free organic ligand in the sample in **9**, since the position for the free ligand band is much stronger than **8**, while the peak at 1704 cm^{-1} for the complex is much weaker than **8** (PXRD shows good purity for **8**).

Table 15: Main infrared bands for the free organic ligand, **8** and **9**.

Vibrational modes	3-HCCA	**8**	**9**
ν_{O-H}	-	3519 cm^{-1}	3519 cm^{-1}
ν_{O-H}		3441 cm^{-1}	3441 cm^{-1}
$\nu_{C=O}$	1736 cm^{-1}	1704 cm^{-1}	1704 cm^{-1}

4.2.2.1.3

Structure description

Single-crystal X-ray analysis was conducted for two of the four complexes obtained, and powder X-ray analysis was conducted for complex **8**. Crystal data and refinement results for **8** and **9** are displayed in Table A4. Ortep images of the asymmetric units of both complexes are displayed in Fig. A6 and A7. Complex **8** and Complex **9** are eneacoordinated and octacoordinated, respectively. The bond

distances and central angles found for both CPs are displayed in Tables 15 and 16. Their fragments and coordination environments are displayed in Figures 72 and 73 (hydrogens were omitted for clarity).

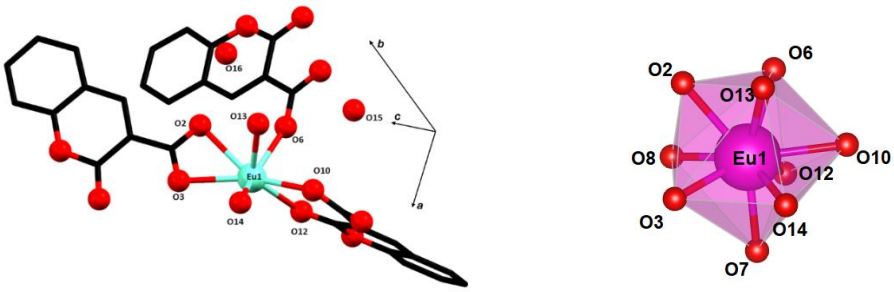

a) b)

Figure 72: a) Asymmetric unit of $\{[Eu(3\text{-}CCA)_3(H_2O)_2](H_2O)_2\}_n$, b) Polyhedron representation of the metal's surrounding.

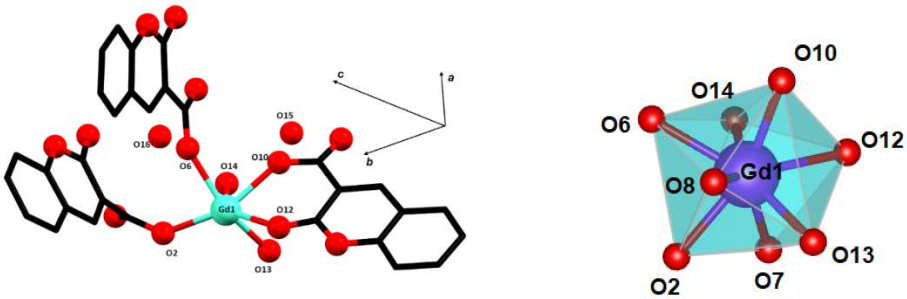

a) **b)**

Figure 73: a) Asymmetric unit of $\{[Gd(3\text{-}CCA)_3(H_2O)_2](H_2O)_2\}_n$, b) Polyhedron representation of the metal's surrounding.

Complex **8** is enea-coordinated, adopting a Tricapped trigonal prism geometry (Shape Program), where we can observe two oxygens coordinated from H2O molecules, two oxygens coordinated through the carboxyl group of the ligand, and two other HCCA coordinated through one of the oxygens from the carboxyl group and one from the lactone part of the ligand. The remaining two coordination spots are from the coumarin responsible for the polymeric chain extension, coordinated with the lactone oxygen and one oxygen from the carboxyl group. In

contrast, the remaining oxygen is coordinated with another Ln via bridge mode. We can observe the extension of the polymeric chain in Figure 74.

Table 16: Bond distances found in the coordination environment for the lanthanide ions.

Bonds distances	**Ln = Eu**	**Bonds distances**	**Ln = Gd**
Ln-O2	2.531(3)	**Ln-O2**	2.333(4)
Ln-O3	2.491(3)	**Ln-O6**	2.339(5)
Ln-O6	2.414(3)	**Ln-O7**	2.406(5)
Ln-O7	2.436(4)	**Ln-O8**	2.471(5)
Ln-O8	2.464(4)	**Ln-O10**	2.299(5)
Ln-O10	2.339(3)	**Ln-O12**	2.488(5)
Ln-O12	2.561(4)	**Ln-O13**	2.342(6)
Ln-O13	2.399(6)	**Ln-O14**	2.396(5)
Ln-O14	2.463(6)	**-**	-

Complex **9** is octacoordinated, adopting a triangular dodecahedron geometry (Shape Program) with two H_2O coordinated to the Gd^{3+} ion alongside three other 3-CCA molecules. The difference from Complex **8** is that none of the organic ligands coordinates through both oxygens from the carboxylate group, resulting in one less coordinated atom. Regardless of this fact, both CPs extend similarly to each other, and their supramolecular arrangements are also similar.

Table 17: Main angles found in the coordination environment for the lanthanide ions.

Bond angles	Ln = Eu	Bond angles	Ln = Gd
O2-Ln-O3	51.6°	**O2-Ln-O6**	80.9°
O2-Ln-O6	73.9°	**O2-Ln-O7**	72.9°
O2-Ln-O8	71.2°	**O2-Ln-O13**	96.6°
O2-Ln-O13	70.8°	**O6-Ln-O8**	72.0°
O3-Ln-O7	76.2°	**O6-Ln-O10**	79.9°
O3-Ln-O8	71.2°	**O6-Ln-O14**	76.5°
O6-Ln-O8	85.5°	**O7-Ln-O8**	69.7°
O6-Ln-O10	87.0°	**O7-Ln-O12**	70.4°
O6-Ln-O12	71.4°	**O8-Ln-O12**	70.6°
O6-Ln-O13	76.7°	**O10-Ln-O12**	68.5°
O7-Ln-O8	68.8°	**O10-Ln-O13**	85.8°
O7-Ln-O10	91.5°	**O10-Ln-O14**	75.8°
O7-Ln-O12	71.1°	**O13-Ln-O14**	69.5°
O7-Ln-O14	71.0°		
O8-Ln-O12	69.7°		
O10-Ln-O12	67.9°		
O10-Ln-O13	76.7°		
O10-Ln-O14	70.6°		

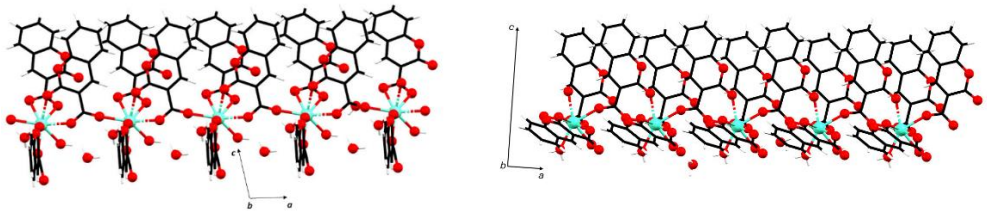

a) b)

Figure 74: a) Extension of **8** as seen through the crystallographic axis *b*. b) Extension of **9** as seen through the crystallographic axis *b*.

The description of polymeric chain extension is similar to that of the previous group discussed, where only one of the coumarin ligands is responsible through the carboxyl group. Because of that, we observe similar intrachain distances of Ln ion cores, as described in Table 17. However, unlike the previously described polymers, we have a substitution of small ligands (H_2O and Cl) for bigger ones, resulting in a different supramolecular distribution.

Table 18: Smallest distances found in $\{[Ln(3\text{-}CCA)_3(H_2O)_2](H_2O)_2\}_n$

Intrachain Ln distances	**Ln = Eu**	**Ln = Gd**
Ln-Ln	6.7038(4)	6.3944(7)
Interchain Ln distances	**Ln = Eu**	**Ln = Gd**
Smallest distance	6.7468(5)	7.3846(8)

For **8** the polymeric chain extends through crystallographic axis *a*, as is observed in Figure 75. (a). In this figure, we can also see one of two different intermolecular interactions between chains that are observed in these complexes, that is, a stacking of the aromatic rings from the HCCA ligand. However, we cannot affirm that this interaction is π-π stacking due to the angles found between the aromatic ring's centroid being around 70°, which is not ideal for this type of interaction. The other interchain interactions are H-bonds between the free, coordinated H_2O molecules and Oxygen atoms from the organic ligand in the structure. Figure 75 (b) shows the H-bonds in more detail. These interactions are responsible for a small interchain distance, where in the case of the Eu complex, the value is obtained between metal centers like the ones found intrachain (~ 6.7 Å) (Table 17).

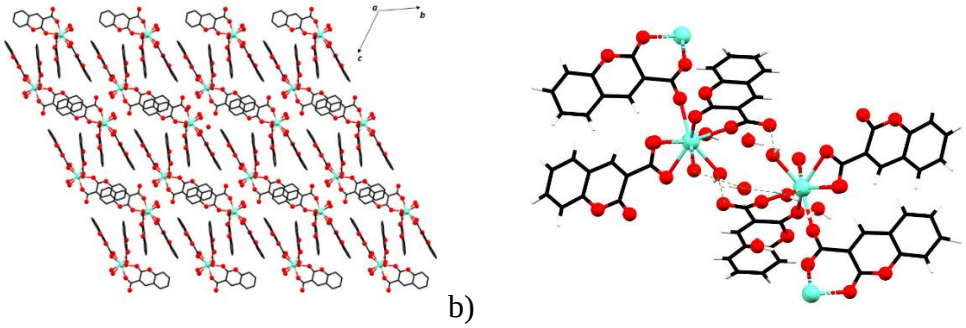

a) b)

Figure 75: Supramolecular arrangement for **8** as seen through crystallographic axis a for a) Overall interactions; b) Classic H-bond interaction up close.

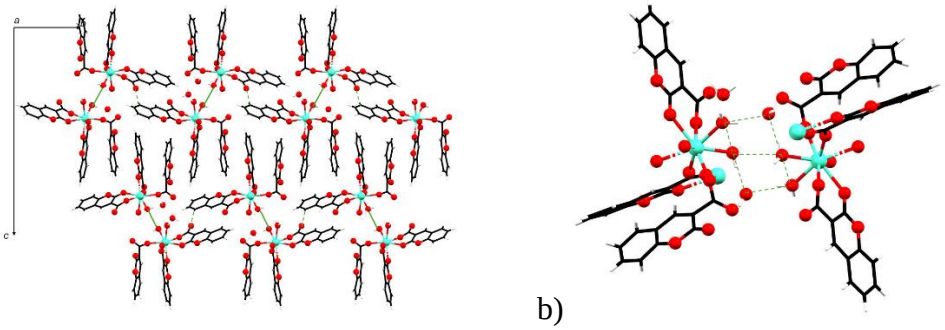

a) b)

Figure 76: Supramolecular arrangement for **9** as seen through crystallographic axis *a* for: a) Overall interactions; b) Classic H-bond interaction up close.

In Figure 76 a) we can observe the supramolecular arrangement for **9.** Differently than **8,** we do not observe a stacking of aromatic rings. The main supramolecular interactions found are classic (full green line, in more detail in (b)) between the coordinated and uncoordinated H_2O molecules in the structure and non-classic H-bonds (dotted line) from the cycle O atom found in the lactone part of the ligand, with the polymeric chain extending through crystallographic axis *a*. In the Gd complex, we obtained a smaller intrachain distance between Gd^{3+} cores (~6.4 Å), and we obtained a more considerable interchain distance (~7.38 Å) when compared to the Eu^{3+} complex.

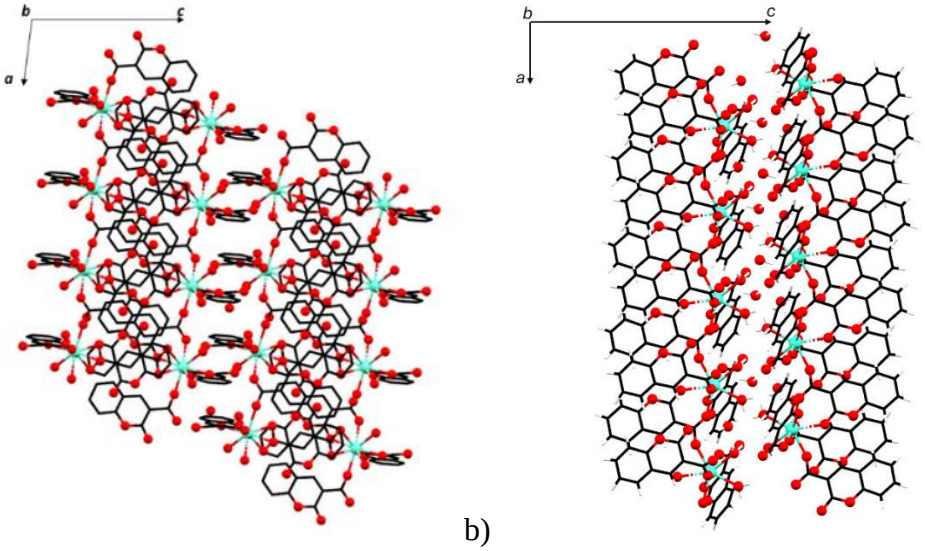

a) b)

Figure 77: Supramolecular arrangement as seen through crystallographic axis *b* for: a) Compound **8**; b) Compound **9.**

In Figure 77 we can observe the supramolecular arrangements seen through crystallographic axis *b.* In (a), we can better observe the aromatic ring stacking for 8, as in (b), the classic H-bonds found in complex **9** are highlighted.

Powder X-ray diffraction measurements were made for **8** and are displayed in Figure 78. The experimental diffractogram was compared with the calculated one obtained from the structure solved by single crystal X-ray diffraction data. We can observe that both diffractograms match, indicating good phase purity for further analysis.

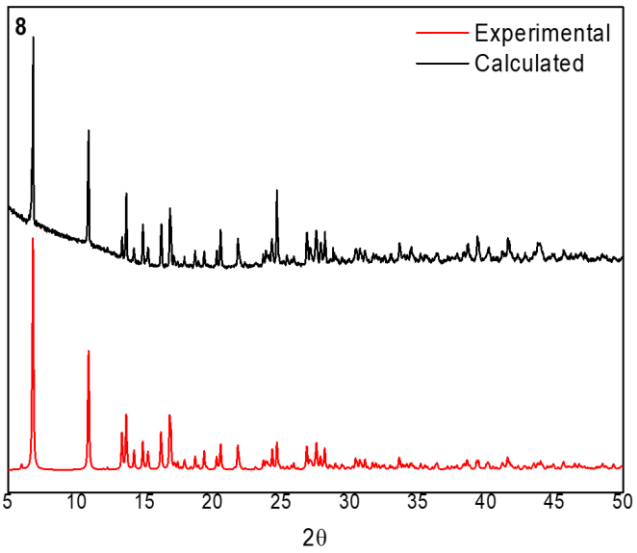

Figure 78: Powder X-ray diffraction for **8**.

4.2.2.2

Photouminescent properties

The emission and excitation spectra for **8** is shown in Figure 79. The excitation spectra (blue color) were registered at 250-500 nm, with the emission monitored in the intense $^5D_0 \rightarrow {}^7F_2$ (λ_{emi} = 614 nm) transition. We can observe an intense and large band from 250-400 nm, attributed to the absorption energy from the ligand S $\rightarrow S_0$ (π, π^*). We can also observe a fine band $^7F_0 \rightarrow {}^5D_2$ corresponding to 4f – 4f transitions of Eu^{3+} ion.

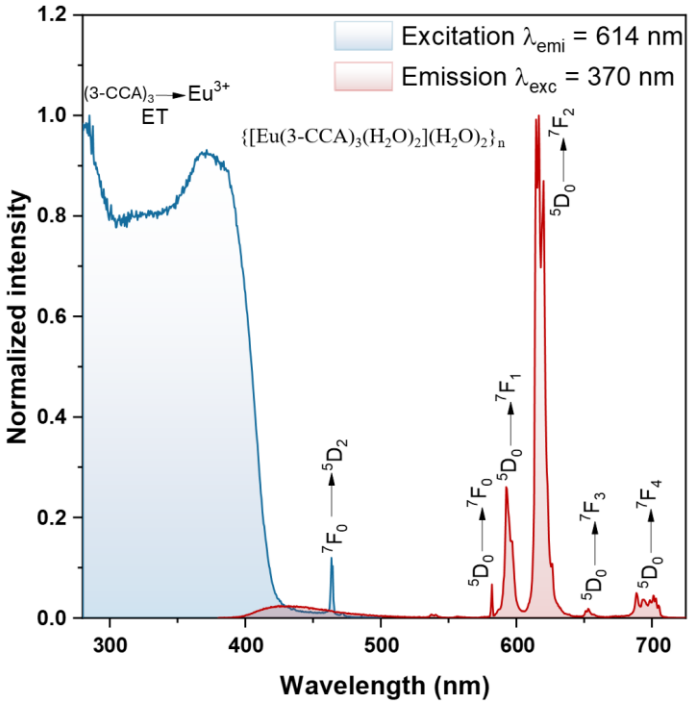

Figure 79: Emission and excitation spectra of **8** (experiment conducted in crystalline form).

The emission spectra (red color) were registered in the interval of (375-750 nm) with the excitation fixed at the highest absorption from the 3-CCA ligand (λ_{exc} = 366 nm). The complex emits many characteristic bands for Eu^{3+} ion, from its main emission state $^5D_0$ to ^7F_J, with j = 0, …, 4. Compared to the complex with only 1 coordinated 3-CCA ligand, the main emission band $^5D_0 \rightarrow {}^7F_2$ seems more intense in this complex, most likely due to the more significant amount of ligand transferring energy to the Eu^{3+} ion. The transition $^5D_0 \rightarrow {}^7F_0$ in one band indicates that all the Eu^{3+} ions occupy the exact influence of the crystalline field.

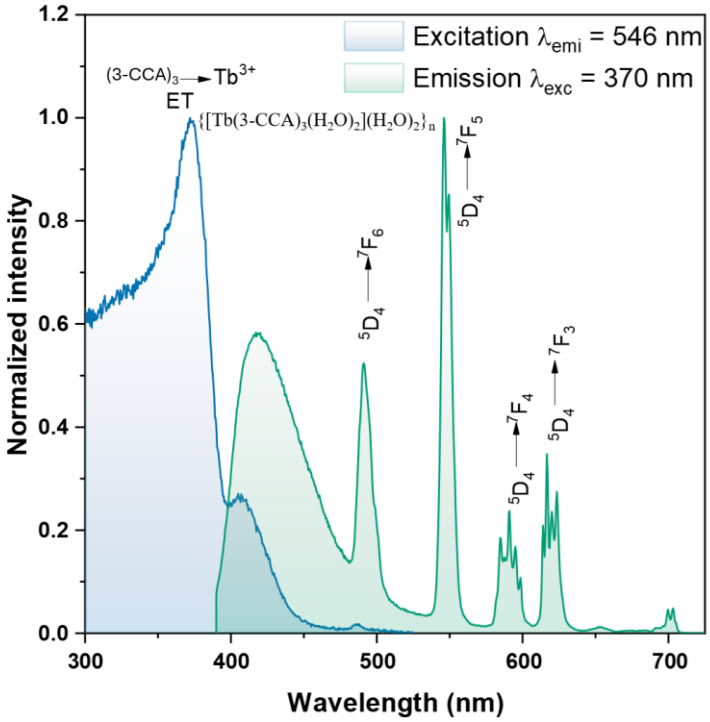

Figure 80: Emission and excitation spectra of **10** (experiment conducted in crystalline form).

For the Tb^{3+} complex, the excitation and emission spectra are displayed in Figure 80. The excitation spectra (blue color) were registered in the interval of 300-525 nm, with the emission monitored in the intense $^5D_4 \rightarrow {}^7F_5$ (λ_{emi} = 545 nm) band. We can observe the same large band from 300-375 nm corresponding to the absorption energy from the ligand $S \rightarrow S_0$ (π, π^*). As expected, the antenna effect was not prevalent, changing the number of organic ligands coordinated since it does not alter the energy level of the molecules.

The emission spectra were registered in the interval of 375-725 nm, with the λ_{exc} = 311 nm being the highest absorption found for the organic ligand. We can observe several characteristic bands from the Tb^{3+} ion involving the main emission state for the lanthanide, $^5D_4 \rightarrow {}^7F_J$ with J = 3, …, 6. However, the characteristics of the bands $^5D_4 \rightarrow {}^7F_3$ and $^5D_4 \rightarrow {}^7F_4$ are different since, in this compound, we can observe the Stark levels. We can also observe another peak at around 700 nm, which

is characteristic of Eu^{3+} compounds. That concludes that this sample was contaminated with Eu^{3+} ions, interfering in the photoluminescent analysis.

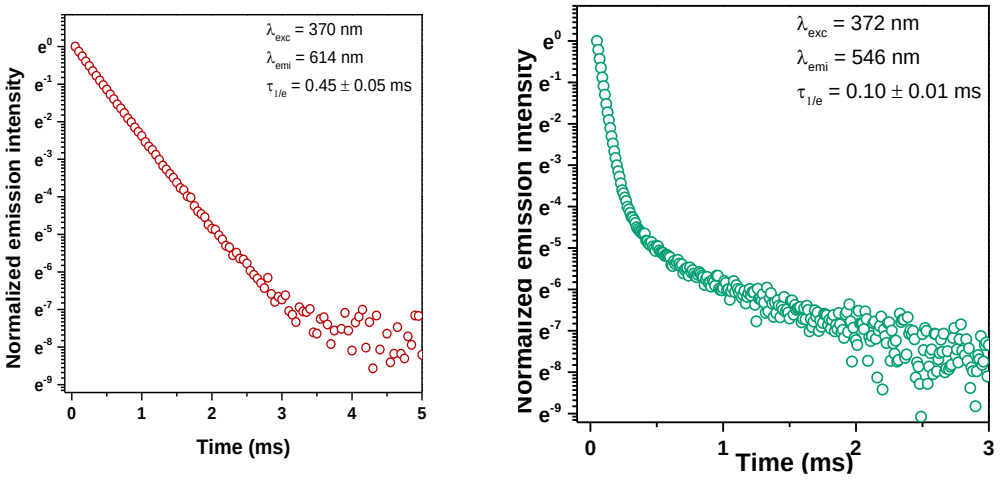

Figure 81: a) Half-life analysis of **8**. b) Half-life analysis of **10**.

For the analysis of the complex's emission lifetime, the transition involving the emission state $^5D_0$ for the Eu^{3+} complex and $^5D_4$ for the Tb^{3+} complex was selected. The first was excited at 366 nm, and their emissions were monitored in the maximum emission wavelength (614 nm), while the latter was excited at 372 nm, with the emission at 546 nm. We can observe that the emission lifetime for the Tb^{3+} complex is smaller than the Eu^{3+} one.

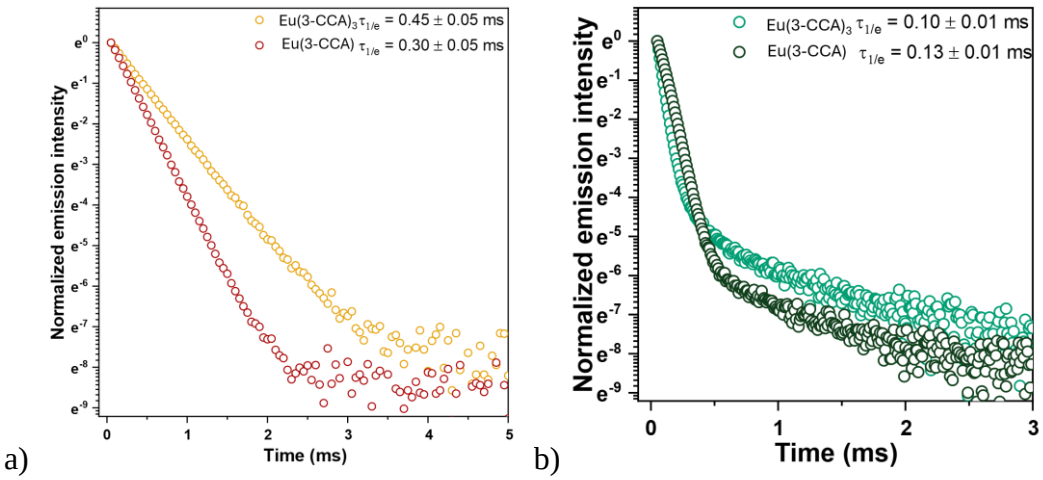

a) b)

Figure 82: Transition lifetime comparison of: a) **4** and **8** b) **6** and **10**.

When comparing both Eu^{3+} complexes obtained, we can observe that the increase in coordinated organic molecules and the removal of 1 coordinated water molecule increased the lifetime of the transition. This is due to the reduction in quenching caused from the harmonics of O-H bond. For the Tb^{3+} complexes, we cannot affirm due to the contamination of the second sample; however, significant differences in the lifetime are not expected due to the low practical antenna effect.

4.2.3
Conclusions

Two CP families were synthesized, and Single-Crystal X-ray analysis was conducted. For the first family, all of them were isomorphs 1D CPs, and their crystal structure was successfully discussed. However, the reproducibility of these complexes' synthesis is still to be optimized due to the crystallization of the complex happening alongside the crystallization of the organic ligand, something that interferes with other analyses such as IV, TG, and DTG, PXRD, and Magnetic susceptibility data. Luminescence studies were conducted for Eu^{3+} and Tb^{3+} complexes, with an evident antenna effect for the Europium complex. Magnetocaloric studies were conducted for the Gd^{3+} complex, but lower-than-expected values were obtained due to the mass problem discussed. With the evidence above, both Tb^{3+} and Dy^{3+} behave as SIMs. However, further analysis is yet to be conducted to precisely determine the relaxation time and energy barrier of these CPs.

Changing the metal: ligand ratio from 1:1 to 1:3, four new CPs that were synthesized. Eu^{3+} and Gd^{3+} complexes had Single-Crystal X-ray analysis conducted where they were not isomorphs. However, both were 1D CPs and presented the same amount of coordinated organic ligands and H_2O molecules. Further

characterization analysis for the remaining CP derivates is required to determine their structure fully. However, IV analysis indicates that both other CPs (Tb^{3+} and Dy^{3+})) have similar structures. Adding two organic molecules and removing one coordinated H_2O molecule in the Eu^{3+} complex resulted in a higher luminescence lifetime. The same was not seen for the Tb^{3+} complex due to a weak antenna effect. However, the possible Eu^{3+} impurity in the Tb^{3+} complex can interfere with the results. Magnetic analysis is yet to be conducted due to the possibility of Tb^{3+} and Dy^{3+} complexes behaving as SIMs.

6

Final Considerations

Nine new coordination compounds were synthesized and characterized by spectroscopy and analytic techniques. For the d-block metals, all the characterizations and magnetic measurements were successfully conducted, obtaining two CP's containing six-coordinated Cu^{2+} and Co^{2+} with BTB and Phen ligand and a Cu^{2+} copper dimmer with the substitution of auxiliary N-donor ligand from Phen to Dmdpy.

The Ln(3-CCA) systems still need further purification to repeat the magnetic measurements and publication of the data. However, the preliminary experiments could indicate the SIM behavior for Tb^{3+} and Dy^{3+} due to the out-of-phase signals obtained in AC magnetic measurements.

During this master's work, two scientific papers were published. The first one was in collaboration with the Lab of Synthesis and Analysis of Organic Compounds (LabSint), where crystallographic measurements were made regarding a new Coumarin molecule synthesized by the group. The second concerns both CPs discussed in Chapter 2. The copper(II) dimer and Ln(3-HCCA)n derivates are also expected to generate two additional scientific papers.

In addition, three different presentations have been made regarding this project. A banner was presented at the 46° annual reunion of the Brazilian Society of Chemistry, and a banner and oral presentation were given at the 7° journey of VII Postgraduation and Research in Chemistry—"Teaching, research and extension: the path to scientific and technological advancement."

6.1

Future Perspective

The purification process of Ln(3-CCA)$_n$ systems is still in development to guarantee the reproducibility of this work and ensure precise characterization and magnetic/spectroscopy measurement.

The author is registered in the PhD program in Chemistry at PUC-Rio, where it will continue to optimize the Ln(3-CCA)$_n$ system alongside the PhD thesis that will evolve the development of magnetic nanoparticles for cancer treatment with magnetic hyperthermia.

REFERENCES

[1] W. Lowrie, Fundamentals of Geophysics, 2nd ed., Cambridge University Press, Zurich, 2007. https://doi.org/10.1017/CBO9780511807107.

[2] E. Coronado, Molecular magnetism: from chemical design to spin control in molecules, materials and devices, Nat. Rev. Mater. 5 (2020) 87–104. https://doi.org/10.1038/s41578-019-0146-8.

[3] O. Kahn, Molecular Magnetism, VCH Publishers, Inc., Ney York, 1993.

[4] J.M.D. Coey, Magnetism and magnetic materials, 1°, Cambridge University Press, New York, 2010. https://doi.org/10.1017/CBO9780511845000.

[5] J.S. Miller, Organic- and molecule-based magnets, Mater. Today. 17 (2014) 224–235. https://doi.org/10.1016/j.mattod.2014.04.023.

[6] P. Cheng, Lanthanides, Elsevier, 2023. https://doi.org/10.1016/C2019-0-04432-9.

[7] R. Sessoli, D. Gatteschi, A. Caneschi, M.A. Novak, Magnetic bistability in a metal-ion cluster, Nature. 365 (1993) 141–143. https://doi.org/10.1038/365141a0.

[8] D. Gatteschi, R. Sessoli, Molecular nanomagnets: The first 10 years, J. Magn. Magn. Mater. 272–276 (2004) 1030–1036. https://doi.org/10.1016/j.jmmm.2003.12.004.

[9] D. Gatteschi, A.L. Barra, A. Caneschi, A. Cornia, R. Sessoli, L. Sorace,

EPR of molecular nanomagnets, Coord. Chem. Rev. 250 (2006) 1514–1529. https://doi.org/10.1016/j.ccr.2006.02.006.

[10] P. Kumar Sahu, R. Kharel, S. Shome, S. Goswami, S. Konar, Understanding the unceasing evolution of Co(II) based single-ion magnets, Coord. Chem. Rev. 475 (2023) 214871. https://doi.org/10.1016/j.ccr.2022.214871.

[11] M. Dolai, H. Ali Molla, G. Rogez, M. Ali, Two [Mn3(μ3-O)]7+ based Single Chain Magnets with different solvent ligation, Polyhedron. 127 (2017) 248–256. https://doi.org/10.1016/j.poly.2017.01.043.

[12] J.M. Frost, K.L.M. Harriman, M. Murugesu, The rise of 3-d single-ion magnets in molecular magnetism: Towards materials from molecules?, Chem. Sci. 7 (2016) 2470–2491. https://doi.org/10.1039/c5sc03224e.

[13] R.S. Drago, Physical Methods for Chemists, 2nd ed., Saunders College Publishing, 1992.

[14] A. Akbarzadeh, M. Samiei, S. Davaran, Magnetic nanoparticles: preparation, physical properties, and applications in biomedicine, Nanoscale Res. Lett. 7 (2012) 144. https://doi.org/10.1186/1556-276X-7-144.

[15] S. Román, Superparamagnetic nanoparticles and the separation problem, (2014). https://mappingignorance.org/2014/03/05/superparamagnetic-nanoparticles-and-the-separation-problem/ (accessed July 25, 2024).

[16] A. Zabala-Lekuona, J.M. Seco, E. Colacio, Single-Molecule Magnets: From Mn12-ac to dysprosium metallocenes, a travel in time, Coord. Chem. Rev. 441 (2021) 213984. https://doi.org/10.1016/j.ccr.2021.213984.

[17] A. Landart-Gereka, M.M. Quesada-Moreno, I.F. Díaz-Ortega, H. Nojiri, M. Ozerov, J. Krzystek, M.A. Palacios, E. Colacio, Large easy-axis magnetic anisotropy in a series of trigonal prismatic mononuclear cobalt(ii) complexes with zero-field hidden single-molecule magnet behaviour: the important role of the distortion of the coordination sphere and intermolecular interactions, Inorg. Chem. Front. 9 (2022) 2810–2831. https://doi.org/10.1039/d2qi00275b.

[18] D. Gatteschi, R. Sessoli, J. Villain, Molecular Nanomagnets, Mol. Nanomagnets. 9780198567 (2007) 1–408. https://doi.org/10.1093/acprof:oso/9780198567530.001.0001.

[19] J.A. Weil, J.R. Bolton, Electron Paramagnetic Resonance: Elementary Theory and Practical Applications, 2nd ed., John Wiley & Sons, New Jersey, 2007.

[20] O. Yalçin, Ferromagnetic Resonance - Theory and Applications, InTech, 2013. https://doi.org/10.5772/50583.

[21] E.C. Duin, Electron Paramagnetic Resonance Theory, (n.d.). https://webhome.auburn.edu/~duinedu/epr/1_theory.pdf (accessed July 19, 2024).

[22] M. Reis, Fundamentals of Magnetism, 1st ed., Elsevier Inc., Kidlington, 2013.

[23] A.M. Tishin, Y.I. Spichkin, V.I. Zverev, P.W. Egolf, A review and new perspectives for the magnetocaloric effect: New materials and local heating and cooling inside the human body, Int. J. Refrig. 68 (2016) 177–186. https://doi.org/10.1016/j.ijrefrig.2016.04.020.

[24] J. Reedijk, K.R. Poeppelmeier, Comprehensive Inorganic Chemistry III, Third Edition, in: J. Reedijk, K.R. Poeppelmeier (Eds.), Compr. Inorg. Chem. III, Third Ed., 3rd ed., Elsevier Ltd, 2023: pp. 1–1071.

[25] M.A. Willard, M. Daniil, Handbook of Magnetic Materials, in: Elsevier B.V., 2013: pp. 173–342.

[26] B. Ensign, R. Choudhary, H. Ucar, D. Paudyal, Electronic structure, magnetic properties, and exchange splitting of gadolinium intermetallics, J. Magn. Magn. Mater. 509 (2020) 166882. https://doi.org/10.1016/j.jmmm.2020.166882.

[27] B. Valeur, M.N. Berberan-Santos, A brief history of fluorescence and phosphorescence before the emergence of quantum theory, J. Chem. Educ. 88 (2011) 731–738. https://doi.org/10.1021/ed100182h.

[28] J.R. Lakowicz, Principles of Fluorescence Spectroscopy, 3rd ed., Springer, Baltimore, 2006.

[29] F.A. Sigoli, A.G.B. Junior, P.C. de S. Filho, Lantanídeos. Química, Luminescência e Aplicações, 1st ed., São Paulo, 2022.

[30] V.K. Pecharsky, K.A.G. Jr, Electronic structure and ionic radius in rare-earth element, (2024). https://www.britannica.com/science/rare-earth-element/Properties-of-the-metals (accessed July 25, 2024).

[31] A. Powell, Lanthanides and Actinides in Molecular Magnetism. Edited by

Richard A. Layfield and Muralee Murugesu., Angew. Chemie Int. Ed. 54 (2015) 15328–15328. https://doi.org/10.1002/anie.201509764.

[32] G.E. Buono-core, H. Li, B. Marciniak, Quenching of excited states by lanthanide ions and chelates in solution, Coord. Chem. Rev. 99 (1990) 55–87. https://doi.org/10.1016/0010-8545(90)80060-7.

[33] K. Binnemans, Interpretation of europium(III) spectra, Coord. Chem. Rev. 295 (2015) 1–45. https://doi.org/10.1016/j.ccr.2015.02.015.

[34] N. Li, R. Feng, J. Zhu, Z. Chang, X.H. Bu, Conformation versatility of ligands in coordination polymers: From structural diversity to properties and applications, Coord. Chem. Rev. 375 (2018) 558–586. https://doi.org/10.1016/j.ccr.2018.05.016.

[35] D. Davarcı, C. Duyar, Y. Zorlu, 3D Ag(I) coordination polymer constructed from a flexible pyridyloxycyclotetraphoshazene linker: Synthesis, crystal structure and dye adsorption properties, Polyhedron. 231 (2023) 2–9. https://doi.org/10.1016/j.poly.2022.116250.

[36] Y.H. Gao, P.P. Huang, H.T. Xu, P. Huang, B. Liu, J.F. Lu, H.G. Ge, Two novel Zn(II) coordination polymers constructed by the same dicarboxylate and different bis-imidazole as co-ligand: Syntheses, crystal structures and properties, J. Mol. Struct. 1281 (2023) 135106. https://doi.org/10.1016/j.molstruc.2023.135106.

[37] C. feng Wang, J. Wang, X. ping Wang, X. Zhang, Y. Meng, F. Chen, L. Lin, X. min Meng, Rational design of three Co(II) coordination polymers based on a semirigid tricarboxylate ligand: Syntheses, structural variability, electrochemical behavior, magnetic and photocatalytic properties, J. Mol. Struct. 1265 (2022) 133439. https://doi.org/10.1016/j.molstruc.2022.133439.

[38] S.N. Zhao, X.Z. Song, S.Y. Song, H. jie Zhang, Highly efficient heterogeneous catalytic materials derived from metal-organic framework supports/precursors, Coord. Chem. Rev. 337 (2017) 80–96. https://doi.org/10.1016/j.ccr.2017.02.010.

[39] H.Y. Wang, L. Cui, J.Z. Xie, C.F. Leong, D.M. D'Alessandro, J.L. Zuo, Functional coordination polymers based on redox-active tetrathiafulvalene and its derivatives, Coord. Chem. Rev. 345 (2017) 342–361. https://doi.org/10.1016/j.ccr.2016.10.011.

[40] R. Sanchis-Gual, M. Coronado-Puchau, T. Mallah, E. Coronado, Hybrid nanostructures based on gold nanoparticles and functional coordination polymers: Chemistry, physics and applications in biomedicine, catalysis and magnetism, Coord. Chem. Rev. 480 (2023) 215025. https://doi.org/10.1016/j.ccr.2023.215025.

[41] F.F. Wu, Y.Q. Wu, Z.X. Wang, X. He, M.X. Li, Structural variation of hydroxide-metal clusters and three Co(II)/Zn(II) coordination polymers assembled by tripodal 3,5-bis(4-carboxybenzyloxy)benzoic acid, Inorg. Chem. Commun. 146 (2022). https://doi.org/10.1016/j.inoche.2022.110202.

[42] L. Liu, Y. Ran, M. Cao, X. Zhao, Y. Mu, Effect of solvent/auxiliary ligand on the structures of Cd(II) coordination polymers based on ligand 5-(2-benzothiazolyl)isophthalic acid, Polyhedron. 199 (2021) 115103. https://doi.org/10.1016/j.poly.2021.115103.

[43] D. Mal, R. Sen, P. Brandao, F. Shi, R.A.S. Ferreira, Z. Lin, Auxiliary ligand-assisted structural diversities of two coordination polymers with 2-hydroxyquinoline-4-carboxylic acid, Inorg. Chem. Commun. 40 (2014) 92–96. https://doi.org/10.1016/j.inoche.2013.11.038.

[44] I.C. Soares, H.C.S. Junior, P.S.V.B. de Almeida, O.C. Alves, S. Soriano, G.B. Ferreira, G.P. Guedes, Coordination polymers containing a pyrazole-based ligand and 4,4′-bipyridine as a spacer: enhancing the family of nonzero-dimensional compounds featuring single-ion magnetic behavior, Inorg. Chem. Commun. 121 (2020) 108201. https://doi.org/10.1016/j.inoche.2020.108201.

[45] S. Benmansour, C. Pintado-Zaldo, S.H. Casal-García, J. Martínez-Ponce, C.J. Gómez-García, Anilato-Based Coordination Polymers with Slow Relaxation of the Magnetization: Role of the Synthetic Method and Anilato Ligand, Chem. – A Eur. J. 30 (2024). https://doi.org/10.1002/chem.202400410.

[46] C. Uhlmann, L. Münzfeld, A. Hauser, T. Ruan, S. Kumar Kuppusamy, C. Jin, M. Ruben, K. Fink, E. Moreno-Pineda, P.W. Roesky, Unique Double and Triple Decker Arrangements of Rare-Earth 9,10-Diborataanthracene Complexes Featuring Single-Molecule Magnet Characteristics, Angew. Chemie Int. Ed. 63 (2024). https://doi.org/10.1002/anie.202401372.

[47] M.-X. Hong, Z.-H. Wu, C. Chen, L. Cao, H. Tian, X.-Y. Zheng, Multifunctional 1D lanthanide-based coordination polymers exhibiting single-chain magnets and fluorescence detection, Polyhedron. 251 (2024) 116847. https://doi.org/10.1016/j.poly.2024.116847.

[48] T.N. Nguyen, G. Capano, A. Gładysiak, F.M. Ebrahim, S. V. Eliseeva, A. Chidambaram, B. Valizadeh, S. Petoud, B. Smit, K.C. Stylianou, Lanthanide-based near-infrared emitting metal–organic frameworks with tunable excitation wavelengths and high quantum yields, Chem. Commun. 54 (2018) 6816–6819. https://doi.org/10.1039/C8CC01294F.

[49] M.B. Coban, A new 3D HoIII-organic framework constructed from 1,3,5-tris(4-carboxyphenyl)benzene and 1,10-phenanthroline: Crystal structure, morphological and solid state luminescence properties, J. Solid State Chem. 317 (2023) 123651. https://doi.org/10.1016/j.jssc.2022.123651.

[50] T. Long, J. Yang, S. Moorthy, D. Shao, S.K. Singh, Y.-Z. Zhang, Incorporating Highly Anisotropic Four-Coordinate Co(II) Ions within One-Dimensional Coordination Chains, Cryst. Growth Des. 23 (2023) 2980–2987. https://doi.org/10.1021/acs.cgd.3c00082.

[51] A.A. Fursina, A. Sinitskii, Toward Molecular Spin Qubit Devices: Integration of Magnetic Molecules into Solid-State Devices, ACS Appl. Electron. Mater. 5 (2023) 3531–3545. https://doi.org/10.1021/acsaelm.3c00472.

[52] R. Stewart, A.B. Canaj, S. Liu, E. Regincós Martí, A. Celmina, G. Nichol, H.-P. Cheng, M. Murrie, S. Hill, Engineering Clock Transitions in Molecular Lanthanide Complexes, J. Am. Chem. Soc. 146 (2024) 11083–11094. https://doi.org/10.1021/jacs.3c09353.

[53] Z.-Q. Wang, J.-J. Li, X.-Y. Guo, J.-X. Ge, J.-L. Wang, Y.-N. Zhu, X.-L. He, N. Qiao, W.-M. Wang, Magnetic refrigeration property and single-molecule magnetic behavior of three asymmetric Ln2 (LnIII = Gd, TB and Dy) compounds, Inorg. Chem. Commun. 158 (2023) 111660. https://doi.org/10.1016/j.inoche.2023.111660.

[54] Y. Zhang, T. Nomoto, S. Yamashita, H. Akutsu, N. Yoshinari, T. Konno, Y. Nakazawa, Direct measurement of magnetocaloric effect (MCE) in frustrated Gd-based molecular complexes, J. Therm. Anal. Calorim. (2024). https://doi.org/10.1007/s10973-024-13344-9.

[55] Bruker, APEX2 , (2007).

[56] Bruker, SAINT, (2013).

[57] G.M. Sheldrick, SADABS, (1996).

[58] G.M. Sheldrick, SHELXL-97 A Program for Crystal Structure Refinement, (1997).

[59] L.J. Farrugia, ORTEP-3 for Windows - a version of ORTEP-III with a Graphical User Interface (GUI), J. Appl. Cryst. 30 (1997) 565.

[60] C.F. Macrae, I.J. Bruno, J.A. Chisholm, P.R. Edgington, P. McCabe, E. Pidcock, L. Rodriguez-Monge, R. Taylor, J. Van De Streek, P.A. Wood, Mercury CSD 2.0 - New features for the visualization and investigation of crystal structures, J. Appl. Crystallogr. 41 (2008) 466–470. https://doi.org/10.1107/S0021889807067908.

[61] L.R.K. R.T. Azuah Y. Qiu, P.L.W. Tregenna-Piggott, C.M. Brown, J.R.D. Copley, R.M. Dimeo, DAVE: A comprehensive software suite for the reduction, visualization, and analysis of low energy neutron spectroscopic data, J. Res. Natl. Inst. Stan. Technol. 114, 341 (2009). 114 (2009).

[62] S. Stoll, A. Schweiger, EasySpin, a comprehensive software package for spectral simulation and analysis in EPR, J. Magn. Reson. 178 (2006) 42–55. https://doi.org/10.1016/j.jmr.2005.08.013.

[63] M.B. Coban, A new 3D HoIII-organic framework constructed from 1,3,5-tris(4-carboxyphenyl)benzene and 1,10-phenanthroline: Crystal structure, morphological and solid state luminescence properties, J. Solid State Chem. 317 (2023) 123651. https://doi.org/10.1016/j.jssc.2022.123651.

[64] F.J. Teixeira, L.S. Flores, T. Valverde, L.B.L. Escobar, M.S. Reis, C.C. Corrêa, Synthesis and magnetic properties of two cobalt-coordination polymers containing 1,10-phenanthroline and alkyl dicarboxylates ligands, J. Mol. Struct. 1261 (2022) 132820. https://doi.org/10.1016/j.molstruc.2022.132820.

[65] J.A.O. Rodrigues, A.U. Torres, N.A.B. de Sousa, T.J.D. de Sousa, J.G.O. Neto, A.S. Reis, M.R. Lage, A.O. dos Santos, C.C. dos Santos, A.S. de Menezes, F.F. de Sousa, Synthesis, characterization, DFT study, and antibacterial activity of a coordination complex of Cu(II) with 1,10-phenanthroline and L-methionine ligands, J. Mol. Struct. 1293 (2023). https://doi.org/10.1016/j.molstruc.2023.136197.

[66] J. Juráková, I. Šalitroš, Co(II) single-ion magnets: synthesis, structure, and magnetic properties, Springer Vienna, 2022. https://doi.org/10.1007/s00706-022-02920-0.

[67] M. Murrie, Cobalt(ii) single-molecule magnets, Chem. Soc. Rev. 39 (2010) 1986. https://doi.org/10.1039/b913279c.

[68] M. Murrie, Cobalt(ii) single-molecule magnets, Chem. Soc. Rev. 39 (2010) 1986–1995. https://doi.org/10.1039/b913279c.

[69] N. V. Reis, M.V. Marinho, T.R.G. Simões, K.C. Metz, R.C.A. Vaz, W.X.C. Oliveira, C.L.M. Pereira, W.P. Barros, C.B. Pinheiro, S.O.K. Giese, D.L. Hughes, K.R. Pirota, W.C. Nunes, H.O. Stumpf, Structural versatility driven by the flexible di(4-pyridyl) sulfide ligand: From cobalt(II) single-ion magnets to sheet-like copper(II) weak antiferromagnets, Polyhedron. 171 (2019) 203–211. https://doi.org/10.1016/j.poly.2019.07.005.

[70] G. Christou, D. Gatteschi, D.N. Hendrickson, R. Sessoli, Single-Molecule Magnets, MRS Bull. 25 (2000) 66–71. https://doi.org/10.1557/mrs2000.226.

[71] I.M. Dias, H.C.S. Junior, S.C. Costa, C.M. Cardoso, A.G.B. Cruz, C.E.R. Santos, D.R.S. Candela, S. Soriano, M.M. Marques, G.B. Ferreira, G.P. Guedes, Mononuclear coordination compounds containing a pyrazole-based ligand: Syntheses, magnetism and acetylcholinesterase inhibition assays, J. Mol. Struct. 1205 (2020). https://doi.org/10.1016/j.molstruc.2019.127564.

[72] A. Abragam, B. Bleaney, Electron Paramagnetic Resonance of Transition Ions, U.K, 1970.

[73] L. Chen, J. Zhou, H.H. Cui, A.H. Yuan, Z. Wang, Y.Q. Zhang, Z.W. Ouyang, Y. Song, Slow magnetic relaxation influenced by change of symmetry from ideal: C i to D 3d in cobalt(II)-based single-ion magnets, Dalt. Trans. 47 (2018) 2506–2510. https://doi.org/10.1039/c7dt04651k.

[74] S. Roy, I. Oyarzabal, J. Vallejo, J. Cano, E. Colacio, A. Bauza, A. Frontera, A.M. Kirillov, M.G.B. Drew, S. Das, Two Polymorphic Forms of a Six-Coordinate Mononuclear Cobalt(II) Complex with Easy-Plane Anisotropy: Structural Features, Theoretical Calculations, and Field-Induced Slow Relaxation of the Magnetization, Inorg. Chem. 55 (2016) 8502–8513.

https://doi.org/10.1021/acs.inorgchem.6b01087.

[75] K.N.S. A. Singh, Optical-acoustic two-phonon relaxation in spin systems, Phys. Status Solidi. 95 (1979) 273–277.

[76] K.N. Shrivastava, Theory of Spin–Lattice Relaxation, Phys. Status Solidi. 117 (1983) 437–458.

[77] R.P. Sharma, A. Saini, D. Monga, P. Venugopalan, J. Jezierska, A. Ozarowski, V. Ferretti, Influence of nitrogen donor ligands on the coordination modes of copper(ii) 2-nitrobenzoate complexes: Structures, DFT calculations and magnetic properties, New J. Chem. 38 (2014) 437–447. https://doi.org/10.1039/c3nj00736g.

[78] N.A. Guilherme, J. Pereira de Oliveira Silva, M. V. Colaço, M. V. dos Santos, R.S. Pugina, F.R. Torres, R.O. Freire, C.M. Barreto, L.F. Marques, First Eu3+, Gd3+ and Tb3+ complexes containing the non-steroidal anti-inflammatory drug ketoprofen and N,N-donors ligands: Synthesis, solid state characterization and photoluminescence studies, J. Lumin. 269 (2024). https://doi.org/10.1016/j.jlumin.2024.120472.

[79] D. Trans, A.W. Addison, T.N. Rao, Synthesis, Structure, and Spectroscopic Properties, (1984).

[80] K. Das, S. Goswami, B.B. Beyene, A.W. Yibeltal, E. Garribba, A. Frontera, A. Datta, EPR, DFT and electrochemical interpretation of a Cu(II) derivative incorporating a Schiff base precursor, Polyhedron. 159 (2019) 323–329. https://doi.org/10.1016/j.poly.2018.11.058.

[81] Y. Singh, R.N. Patel, S.K. Patel, R.N. Jadeja, A.K. Patel, N. Patel, H. Roy, P. Bhagriya, R. Singh, R.J. Butcher, J.P. Jasinski, S. Herrero, M. Cortijo, Supramolecular assemblies of new pseudohalide end-to-end bridged copper(II) complex and molecular structural variety of penta and hexa-coordinted metal(II) complexes with hydrazido-based ligand, Inorganica Chim. Acta. 503 (2020) 119371. https://doi.org/10.1016/j.ica.2019.119371.

[82] J. Ran, X. Zhao, X. Hu, Y. Chen, Z. Tian, 3D Tb(III) and Eu(III) coordination polymers with mixed dicarboxylate ligands: Synthesis, structure and luminescence properties, Polyhedron. 194 (2021) 114910. https://doi.org/10.1016/j.poly.2020.114910.

[83] M. Tsvetkov, D. Elenkova, M. Kolarski, R. Lyapchev, B. Morgenstern, V. Videva, J. Zaharieva, M. Milanova, Synthesis, crystal structure and

luminescence properties of two novel Tb(III) complexes with 1,10-phenanthroline derivatives as ligands, J. Mol. Struct. 1314 (2024) 138768. https://doi.org/10.1016/j.molstruc.2024.138768.

[84] Z.Y. Li, F.F. Wang, P.Y. Zhu, D.Q. Wu, G.X. Cao, B. Zhai, One trans-aconitate-based two-dimensional Gd(III) polymer displaying large magnetocaloric effect, Inorg. Chem. Commun. 120 (2020) 108166. https://doi.org/10.1016/j.inoche.2020.108166.

[85] W.-W. Wei, L.-P. Lu, S.-S. Feng, M.-L. Zhu, U. Englert, Synthesis, structure and magnetocaloric properties of a new two-dimensional gadolinium(III) coordination polymer based on azobenzene-2,2′,3,3′-tetracarboxylic acid, Acta Crystallogr. Sect. C Struct. Chem. 77 (2021) 591–598. https://doi.org/10.1107/S2053229621008871.

Appendix

Crystallographic data and ORTEP images

Table A1: Crystal data and refinement results for complexes **1** and **2**.

	{[Co(H$_3$BTB)$_2$(phen)](NO$_3$)$_2$}$_n$	**{[Cu(HBTB)$_2$(phen)]DMF}$_n$**
Formula	$C_{66}H_{44}CoN_4O_{18}$	$C_{72}H_{54}CuN_4O_{14}$
Formula weight	1239.98	1262.73
Crystal system	Monoclinic	Monoclinic
Space group	C2/c	C2/c
a (Å)	18.2202(7)	18.3706(10)
b (Å)	11.0533(4)	11.0279(6)
c (Å)	31.7162(10)	31.8192(18)
α (°)	90	90
β (°)	97.1750(10)	98.864(2)
Y (°)	90	90
*V (*Å^3)	6337.4(4)	6369.24
Z	4	4
Crystal size (mm)	0.632 x 0.576 x 0.410	0.249 x 0.201 x 0.103
Dcalc (g cm^{-3})	1.295	1.317
μ(Mo Kα) (cm^{-1})	0.344	0.413
T_{min}/T_{max}	0.805/0.868	0.905/0.958
Measured reflections	198860	160529
Unique reflections	6503	7319
Observed reflections	5978	5877
No. parameters	440	417
R ([$F^2 > 2\sigma(F^2)$])	0.053	0.0517
wR	0.152	0.1727
S	1.05	1.203
CCDC No.	2321446	2321447

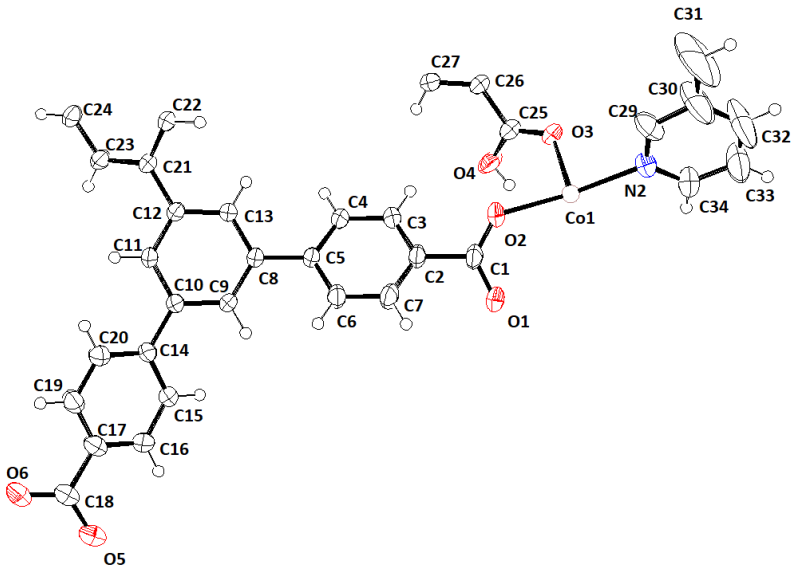

Figure A1: Ortep representation of the asymmetric unit of $[Co(H_3BTB)_2(phen)](NO_3)_2\}_n$ (Ellipsoids 50% probability). The free nitrate ion has been omitted for sake of clarity.

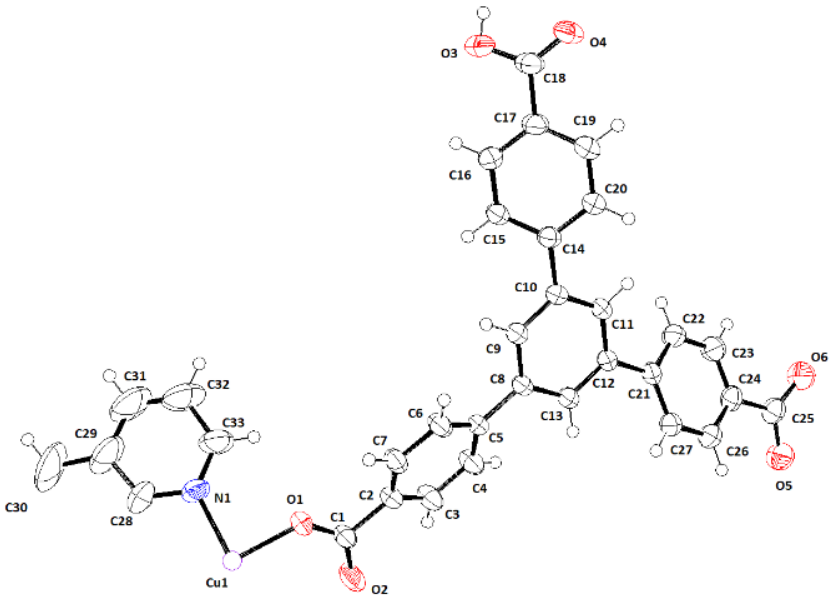

Figure A2: Ortep representation of the asymmetric unit of $\{[Cu(HBTB)_2(phen)]DMF\}_n$ (Ellipsoids 50% probability). The free DMF has been omitted for sake of clarity.

Table A2: Crystal data and refinement results for [Cu(HBTB)Dmdpy].2H_2O

	[Cu(HBTB)Dmdpy].2H_2O
Formula	$C_{39}H_{28}CuN_2O_8$
Formula weight	720,20
Crystal system	triclinic
Space group	P-1
a (Å)	7.7445(3)
b (Å)	12.5128(3)
c (Å)	17.4762(6)
α (°)	97.819(2)
β (°)	92.791(3)
Y (°)	96.871(2)
*V (*Å^3)	1662.10(10)
Z	2
Crystal size (mm)	0.12 x 0.08 x 0.04
Dcalc (g cm^{-3})	1.439
μ(Mo Kα) (cm^{-1})	1.417
T_{min}/T_{max}	0.946/0.848
Measured reflections	25515
Unique reflections	6842
Observed reflections	5755
No. parameters	568
R	0.0468
wR	0.1262
S	1.036
CCDC No.	

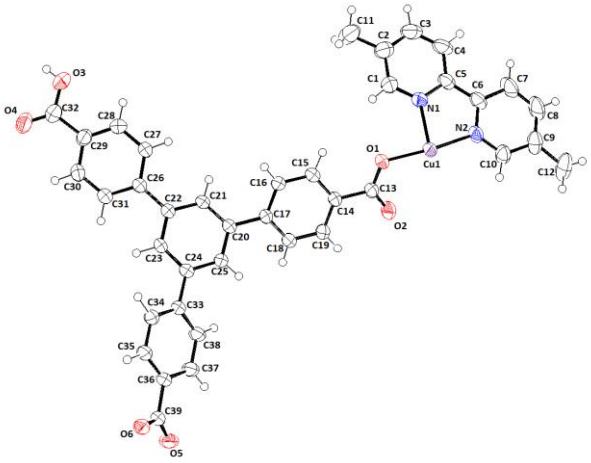

Figure A3: Ortep representation of the asymmetric unit of [Cu(HBTB)Dmdpy].2H_2O (Ellipsoids 50% probability). The free H_2O has been omitted for sake of clarity.

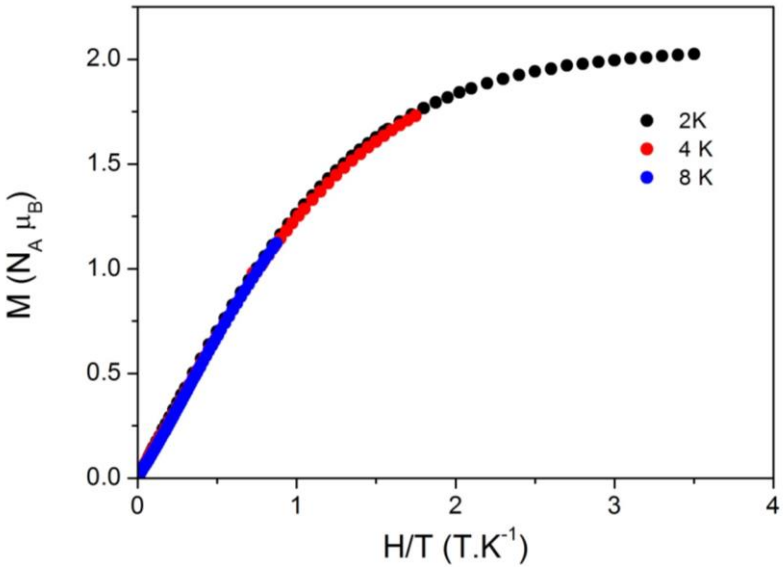

Figure A4: Isothermal field dependence of the magnetization at 2K, 4K and 8K for compound **3**.

Table A3- Crystal data and refinement results for $\{[LnCl_2(3\text{-}CCA)(H_2O)_3]H_2O\}_n$.

	$\{[EuCl_2(3\text{-}CCA)(H_2O)_3]H_2O\}_n$	**$\{[GdCl_2(3\text{-}CCA)(H_2O)_3]H_2O\}_n$**	**$\{[TbCl_2(3\text{-}CCA)(H_2O)_3]H_2O\}_n$**	**$\{[DyCl_2(3\text{-}CCA)(H_2O)_3]H_2O\}_n$**
Formula	$C_{10}H_{13}Cl_2EuO_8$	$C_{10}H_{13}Cl_2GdO_8$	$C_{10}H_{13}Cl_2TbO_8$	$C_{10}H_{13}Cl_2DyO_8$
Formula weight	484.06	489.35	491.02	494.60
Crystal system	Triclinic	Triclinic	Triclinic	Triclinic
Space group	P-1	P-1	P-1	P-1
a (Å)	6.4287(3)	6.4119(3)	6.39670(10)	6.3891(4)
b (Å)	7.0855(3)	7.0230(4)	7.0139(2)	7.0133(4)
c (Å)	17.5738(8)	17.4946(8)	17.4962(5)	17.4794(11)
α (°)	82.5290(10)	82.501(3)	82.5030(10)	82.556(4)
β (°)	85.4150(10)	85.193(3)	85.132(2)	85.231(3)
Y (°)	64.0870(10)	63.541(2)	63.678(2)	63.590(4)
V (Å^3)	713.661	698.95(6)	697.25(3)	695.29(8)
Z	2	2	2	2
Crystal size (mm)	0.404 x 0.258 x 0.080	0.208 x 0.082 x 0.060	0.140 x 0.100 x 0.090	0.152 x 0.056 x 0.054
Dcalc (g cm^{-3})	2.253	2.325	2.339	2.363
μ(Mo Kα) (cm^{-1})	4.803	5.1410	5.490	5.793
T_{min}/T_{max}	0.247/0.700	0.4107/0.7449	0.514/0.638	0.745/0.473
Measured reflections	25548	14129	3783	4753
Unique reflections	2510	5758	2603	2853
Observed reflections	2458	5331	2453	2596
No. parameters	197	242	241	241
R	0.0183	0.0292	0.0310	0.0276
wR	0.0456	0.0714	0.0810	0.0628
S	1.220	1.045	1.046	1.070
CCDC No.				

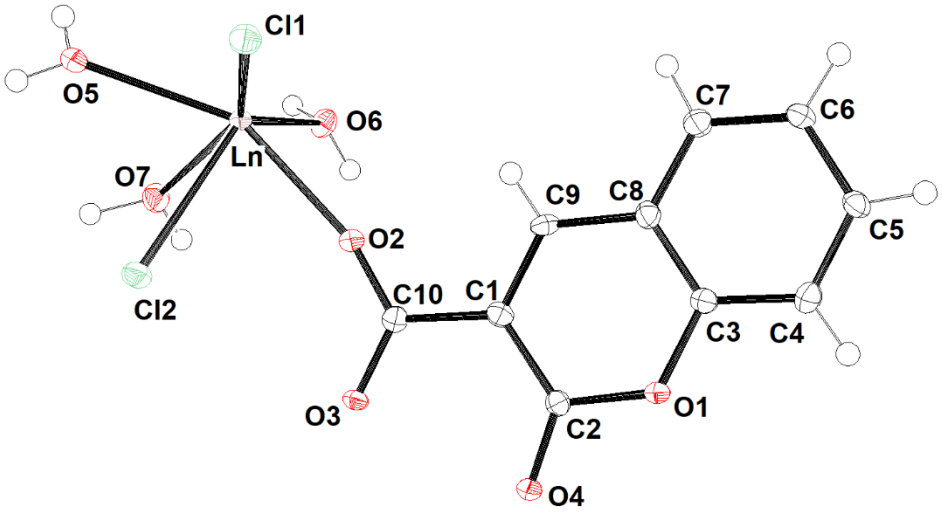

Figure A5: Ortep representation of the asymmetric unit of $\{[LnCl_2HCCA(H_2O)_3]H_2O\}_n$. (Ellipsoids 50% probability). The free H_2O has been omitted for sake of clarity.

Table A4: Crystal data and refinement results for $\{[Ln(3\text{-}CCA)_3(H_2O)_2](H_2O)_2\}_n$.

	$\{[Eu(3\text{-}CCA)_3(H_2O)_2](H_2O)_2\}_n$	**$\{[Gd(3\text{-}CCA)_3(H_2O)_2](H_2O)_2\}_n$**
Formula	$C_{30}H_{23}EuO_{16}$	$C_{30}H_{23}GdO_{16}$
Formula weight	791.44	796.73
Crystal system	Triclinic	Monoclinic
Space group	P-1	P 21/c
a (Å)	6.7038(2)	6.3944(4)
b (Å)	14.4738(6)	14.2250(8)
c (Å)	16.4695(5)	31.7647(19)
α (°)	115.366(2)	90
β (°)	93.898(2)	92.171(3)
Y (°)	94.663(2)	90
*V (*Å^3)	1429.77(9)	2887.3(3)
Z	2	4
Crystal size (mm)	0.330 x 0.044 x 0.032	0.350 x 0.022 x 0.010
Dcalc (g cm^{-3})	1.838	1.833
μ(Mo Kα) (cm^{-1})	2.277	2.380
T_{min}/T_{max}	0.520/0.931	0.490/0.977
Measured reflections	14184	14485
Unique reflections	7786	6262
Observed reflections	6150	2736
No. parameters	512	480
R	0.0385	0.0501
wR	0.0838	0.0547
S	1.028	0.834
CCDC No.		

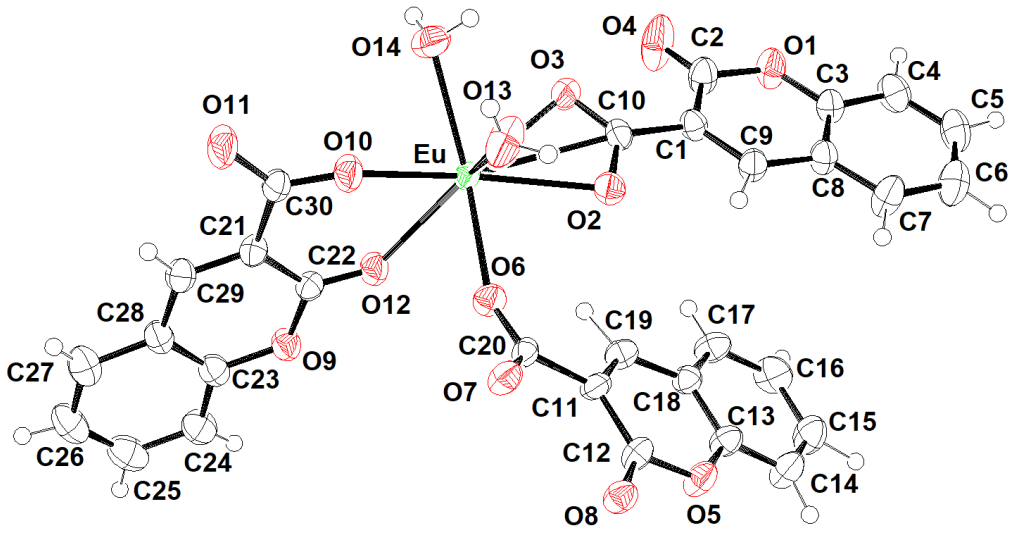

Figure A6: Ortep representation of the asymmetric unit of $\{[Eu(HCCA)_3(H_2O)_2]H_2O\}_n$ (Ellipsoids 50% probability). The free H_2O has been omitted for sake of clarity.

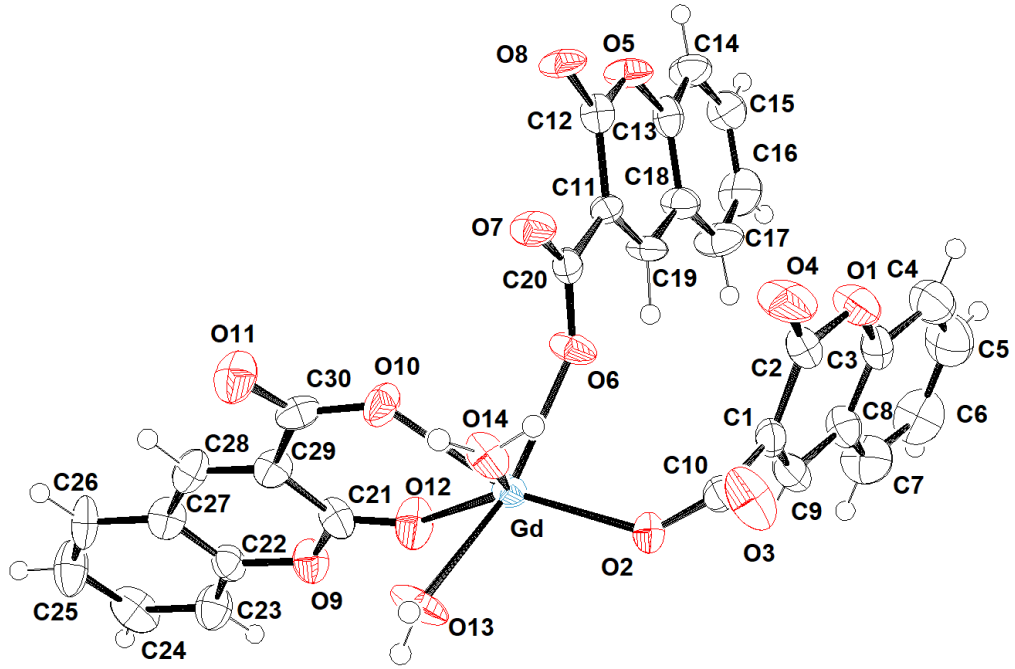

Figure A7: Ortep representation of the asymmetric unit of $\{[Gd(HCCA)_3(H_2O)_2]H_2O\}_n$ (Ellipsoids 50% probability). The free H_2O has been omitted for sake of clarity.

MAGNETIC DATA

Table A5- Summary of the parameters for the concurrent fit of the in-phase and out-of-phase ac magnetic susceptibilities by the extended Debye model for **1**.

T (K)	χ_S ($cm^3.mol^{-1}$)	$\Delta\chi$ ($cm^3.mol^{-1}$)	α	τ (s)
2.0	0.040	0.549	0.064	5.48×10^{-5}
2.2	0.041	0.507	0.060	4.58×10^{-5}
2.4	0.042	0.468	0.055	3.83×10^{-5}
2.6	0.042	0.436	0.053	3.23×10^{-5}
2.8	0.042	0.407	0.051	2.74×10^{-5}
3.0	0.043	0.380	0.046	2.34×10^{-5}
3.2	0.043	0.357	0.045	2.00×10^{-5}
3.4	0.043	0.336	0.049	1.71×10^{-5}
3.6	0.043	0.316	0.046	1.48×10^{-5}
3.8	0.043	0.299	0.046	1.29×10^{-5}
4.0	0.044	0.283	0.045	1.13×10^{-5}
4.2	0.043	0.269	0.045	9.9×10^{-6}
4.4	0.042	0.256	0.045	8.8×10^{-6}
4.6	0.040	0.246	0.047	7.7×10^{-6}
4.8	0.038	0.237	0.050	6.8×10^{-6}
5.0	0.037	0.228	0.057	6.0×10^{-6}

Scientific production

Works published in event annals (summary):

1. **HOLLAUER, H. V. P.**; SALOMAO, G.; ESCOBAR, LÍVIA B. L.; GUEDES, GUILHERMEP..Bis(1,3,5-tris(4-carboxyphenyl)benzoate)phenanthrolinecobalt(II):Synthesis, Characterization, Polymeric Crystal Structure and Magnetic Properties In: 46° Reunião Anual da Sociedade Brasileira de Química, 2023, Águas de Lindóia. **Resumo da 46° Reunião Anual da SBQ**2023,

Presentation of work and lecture:

1. **HOLLAUER, H. V. P.**; SALOMAO, G.; GUEDES, GUILHERME P.; GHIVELDER, L.; SORIANO, S.; ESCOBAR, LÍVIA B. L.. Síntese, estrutura cristalina e propriedades magnéticas de dois polímeros de coordenação 1D contendo Co(II) e Cu(II), 1,3,5-tris(4- carboxilfenil)benzeno e 1,10-fenantrolina, 2023. (Lecture, Work presentation)

2. SAADE, G. Q.; **HOLLAUER, HENRIQUE V. P.**; DINIZ, R.; ESCOBAR, L. B. L.. Síntese e estudo de estrutura cristalina de um dímero de Cu(II), contendo 1,3,5-tris(4-carboxilfenil)benzeno e 5-5'dimetil-2-2'dipiridil, 2023. (Work Presentation)

Published articles

Acta Cryst E CRYSTALLOGRAPHIC COMMUNICATIONS

ISSN 2056-9890

Synthesis, characterization and crystal structure of methyl 2-(2-oxo-2*H*-chromen-4-ylamino)benzoate

Henrique V. P. Hollauer,[a] Rachel C. Vilas Novas,[a] Guilherme P. Guedes,[b] Camilla D. Buarque[a] and Lívia B. L. Escobar[a]*

[a]Chemistry Department, Pontifical Catholic University of Rio de Janeiro, 22451-900 Rio de Janeiro, RJ, Brazil, and [b]Chemistry Institute, Federal Fluminense Universidade, Niteroi, 24020-141 Rio de Janeiro, Brazil. *Correspondence e-mail: liviablescobar@puc-rio.br

Received 19 July 2023
Accepted 21 August 2023

Edited by J. T. Mague, Tulane University, USA

Keywords: crystal structure; coumarin; benzoate; ester.

CCDC reference: 2289922

Supporting information: this article has supporting information at journals.iucr.org/e

Methyl 2-(2-oxo-2*H*-chromen-4-ylamino)benzoate, $C_{17}H_{13}NO_4$ (**1**), was prepared by condensation between 4-hydroxycoumarin and methyl 2-aminobenzoate. It crystallizes in the orthorhombic space group $Pca2_1$ at 300 K. The molecule of compound **1** consists of the 2*H*-chromen-2-one part connected by an amine moiety (–NH–) to the methyl benzoate ring. The supramolecular array is formed by hydrogen bonds between the aromatic ring and the O atoms of the lactone and ester portions. The structural details match the spectroscopic data acquired from NMR and IR spectroscopy.

1. Chemical context

Coumarins are an important class of lactones composed of benzene fused to an α-pyrone ring (Fig. 1). These structures have two pharmacophoric groups: the aromatic ring, which can promote hydrophobic interactions, such as π-interactions, and the lactone group, which is a hydrogen-bond acceptor with receptors such as enzymes (Yildirim *et al.*, 2023).

These compounds are widely distributed in nature, especially as secondary metabolites of vascular plants. Coumarin was first isolated from tonka beans (*Dipteryx odorata* Wild; Fabaceae family) by Vogel in 1820. Since then, more than 1300 coumarins have been identified from natural sources (Bor *et al.*, 2016).

Their versatile scaffold also brings a wide range of applications, such as biocides, phytochemicals, pharmacological agents and flavorings, widely used in different industries. In medicinal chemistry, a widely used coumarin drug is warfarin, an anticoagulant that has made it possible for thrombosis treatment to be done orally (Annunziata *et al.*, 2020). In addition, multiple biological activities are well known, including anti-inflammatory (Bansal *et al.*, 2013), antimicrobial (Regal *et al.*, 2020), antioxidant (Rosa *et al.*, 2021), anti-allergic (Liu *et al.*, 2019), anti-HIV (Xu *et al.*, 2021), anticancer (Emam *et al.*, 2023) and antiviral (Sharapov *et al.*, 2023) activities.

Recent work has demonstrated the importance of coumarins in the design of small-molecule fluorescent chemosensors (Cao *et al.*, 2019). Here we report the synthesis and characterization of methyl 2-(2-oxo-2*H*-chromen-4-ylamino)-benzoate, **1** (Fig. 2), by condensation between 4-hydroxycoumarin and methyl 2-aminobenzoate, according to the literature (Carneiro *et al.*, 2021). The principal purpose of producing this compound was to investigate its biological properties because coumarin derivatives are potential candidates for antileishmaniasis drugs (Carneiro *et al.*, 2021). Also, studies involving the complexation of this molecule with metal

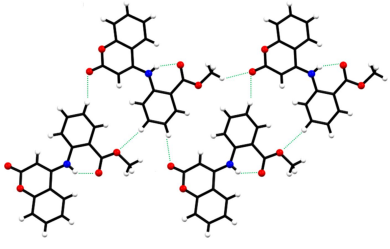

Table 1
Hydrogen-bond geometry (Å, °).

D—H···A	D—H	H···A	D···A	D—H···A
C1—H1B···O4^{i}	0.96	2.52	3.232 (8)	131
C7—H7···O4^{ii}	0.93	2.47	3.387 (6)	167
N1—H1···O2	0.84 (6)	1.92 (6)	2.631 (6)	141 (5)

Symmetry codes: (i) $x-1, y, z$; (ii) $x-\frac{1}{2}, -y+2, z$.

ions, such as Cu^{II} and Gd^{III}, are in progress in our laboratory for future contributions.

2. Structural commentary

Compound **1** was synthesized *via* a reaction of the precursor coumarin and the corresponding aniline (Scheme 1). The resulting compound was recrystallized from dimethylformamide to yield yellow single crystals. Compound **1** crystallizes in the orthorhombic space group $Pca2_1$, with the asymmetric unit consisting of one methyl 2-(2-oxo-2*H*-chromen-4-ylamino)benzoate molecule (Fig. 3). The absolute structure could not be established with certainty.

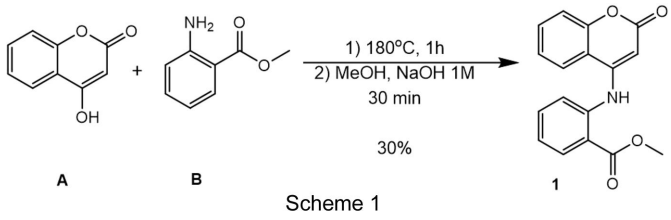

Scheme 1

The average C—C bond distance in the aromatic portion of the coumarin is 1.374 (7) Å, while the C9—C13, C9—C10 and C10—C11 bond lengths in the lactone portion are 1.450 (7), 1.353 (7) and 1.412 (7) Å, respectively, because of the partial localization of π-bonding within the ring. The C11—O3 and C12—O3 bond lengths are equivalent at 1.374 (7) and 1.373 (7) Å, respectively, while the C11═O4 distance is 1.204 (7) Å. The sum of the angles about N1 is 359 (3)°, implicating involvement of its lone pair in N—C π-bonding. This is supported by the N1—C9 and N1—C4 distances of 1.351 (6) and 1.391 (6) Å, respectively. Similar geometrical parameters are found in closely related structures (see *Database survey* section), although the C4—N1—C9 angle at 130.9 (4)° is about 7° larger than in those molecules, presumably due to the intramolecular N1—H1···O2 hydrogen bond (Table 1). In the C3–C8 ring, the average C—C bond distance is 1.379 (8) Å, with the ester portion bond lengths of C2═O2 = 1.203 (6), C2—O1 = 1.316 (7) and C1—O1 = 1.440 (8) Å.

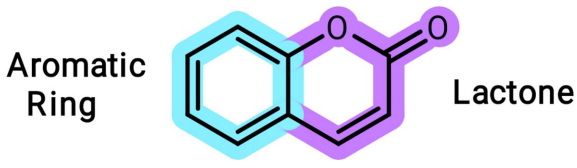

Figure 1
The main structure of coumarins.

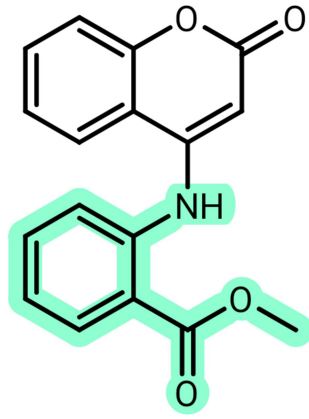

Figure 2
Chemical structure of **1**.

The dihedral angle between the mean plane which contains the main structure of the coumarin and the mean plane containing the aromatic ester portion is 31.21 (10)°.

The NMR spectra are shown in Figs. 4 and 5. The characterization by ^{1}H and ^{13}C NMR confirms the product as methyl 2-(2-oxo-2*H*-chromen-4-ylamino)benzoate. In the ^{1}H NMR spectrum, there is a singlet at δ 3.74 ppm attributable to the methoxy group of the ester, the coumarin vinylic H atom appears at δ 5.31 ppm and a singlet is seen at δ 9.67 which can be assigned to N—H. In addition, there are eight aromatic H atoms between δ 7.44 and 8.14 ppm. In the ^{13}C NMR spectrum, the methoxy group appears at δ 52.47 ppm, the two carbonyl C atoms at δ 166.50 and 161.40, and the vinylic and aromatic C atoms between δ 114 and 154 ppm.

3. Supramolecular features

The supramolecular array is formed by hydrogen bonds between the H atoms of the methyl group and the O atom of

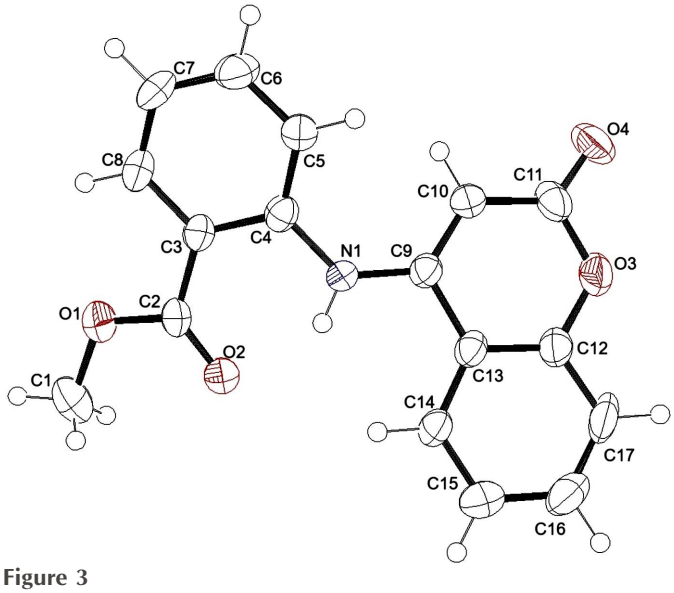

Figure 3
The asymmetric unit of **1**, with the numbering scheme and 50% probability displacement ellipsoids.

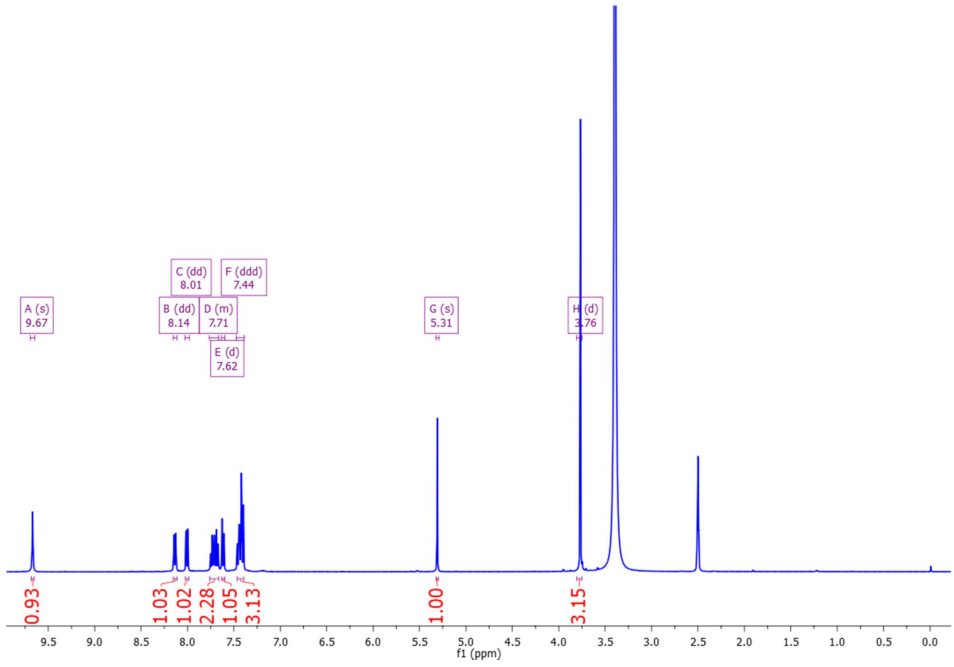

Figure 4
NMR-H: ^{1}H NMR (400 MHz, DMSO-d_6) δ 9.67 (*s*, 1H), 8.14 (*dd*, *J* = 8.1, 1.2 Hz, 1H), 8.01 (*dd*, *J* = 7.9, 1.5 Hz, 1H), 7.76–7.66 (*m*, 2H), 7.62 (*d*, *J* = 7.4 Hz, 1H), 7.44 (*ddd*, *J* = 15.4, 9.8, 4.6 Hz, 3H), 5.31 (*s*, 1H), 3.76 (*d*, *J* = 7.7 Hz, 3H).

the lactone portion (C1—H1*B*···O4^{i}) and the H atom from the aromatic ring (C7—H7···O4^{ii}) (Table 1). These build corrugated chains two molecules wide extending along the *a*-axis direction (Fig. 6). The crystal packing (Fig. 7) involves layers of chains parallel to the *ab* plane which stack along the *c*-axis direction, all associated through van der Waals interactions.

4. Database survey

A search of the Cambridge Structural Database (CSD; Groom *et al.*, 2016; updated to March 2023) yielded a substantial number of hits for chromenes having a nitrogen-containing substituent in the 3-position of the lactone ring but relatively few with this substituent in the 4-position. Most of the latter

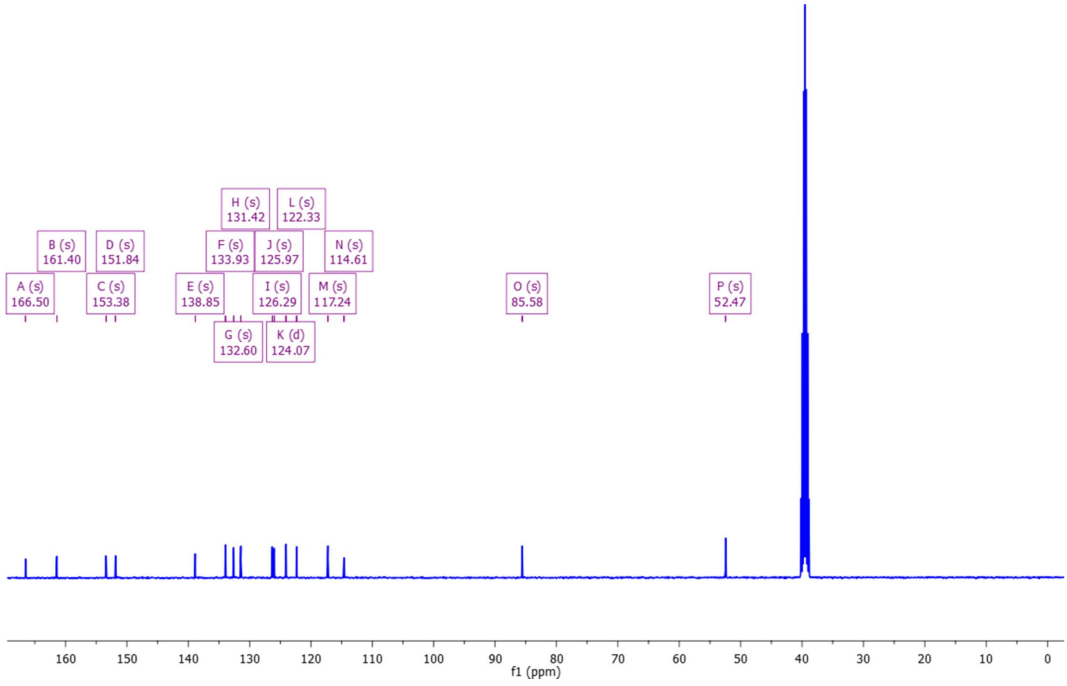

Figure 5
NMR-C: ^{13}C NMR (101 MHz, DMSO-d_6) δ 166.50 (*s*) 161.40 (*s*), 153.38 (*s*), 151.84 (*s*), 138.85 (*s*), 133.93 (*s*), 132.60 (*s*), 131.42 (*s*), 126.29 (*s*), 125.97 (*s*), 124.07 (*d*, *J* = 4.0 Hz), 122.33 (*s*), 117.24 (*s*), 114.61 (*s*), 85.58 (*s*), 52.47 (*s*).

Table 2
Experimental details.

Crystal data	
Chemical formula	$C_{17}H_{13}NO_4$
M_r	295.28
Crystal system, space group	Orthorhombic, $Pca2_1$
Temperature (K)	298
a, b, c (Å)	12.7698 (16), 14.9212 (18), 7.1087 (8)
V (Å^3)	1354.5 (3)
Z	4
Radiation type	Mo $K\alpha$
μ (mm^{-1})	0.10
Crystal size (mm)	0.39 × 0.08 × 0.06
Data collection	
Diffractometer	Bruker D8 Venture
Absorption correction	Multi-scan (*SADABS*; Krause *et al.*, 2015)
T_{min}, T_{max}	0.666, 0.745
No. of measured, independent and observed [$I > 2\sigma(I)$] reflections	35019, 2328, 2096
R_{int}	0.102
(sin $\theta/\lambda)_{max}$ (Å^{-1})	0.595
Refinement	
$R[F^2 > 2\sigma(F^2)]$, $wR(F^2)$, S	0.066, 0.158, 1.08
No. of reflections	2328
No. of parameters	204
No. of restraints	1
H-atom treatment	H atoms treated by a mixture of independent and constrained refinement
$\Delta\rho_{max}$, $\Delta\rho_{min}$ (e Å^{-3})	0.25, −0.37
Absolute structure	Flack x determined using 771 quotients $[(I^+) - (I^-)]/[(I^+) + (I^-)]$ (Parsons *et al.*, 2013)
Absolute structure parameter	0.2 (7)

Computer programs: *APEX4* (Bruker, 2021), *SAINT* (Bruker, 2021), *SHELXT2018* (Sheldrick, 2015*a*) and *SHELXL2018* (Sheldrick, 2015*b*).

also contained a second substituent in the 3-position, such as 4-[(4-bromophenyl)amino]-3-(phenylselanyl)-2*H*-chromen-2-one (OFIHOE; Belladona *et al.*, 2023), but only three are directly comparable to **1**. These are 4-(propylamino)-2*H*-chromen-2-one (HIDYEB; Kumar *et al.*, 2018), 4-[(pyridin-3-ylmethyl)amino]-2*H*-chromen-2-one (TUWLUV; Ait-Ramdane-Terbouche *et al.*, 2020) and 4-(benzylamino)-2*H*-chromen-2-one (ZOKVIE; Campbell *et al.*, 1995). All three have structural parameters very similar to those of **1**, including essentially planar chromene portions and some localization of π-bonding in the lactone portion. The largest difference is seen for the exocyclic C—N—C angles which are around 123°.

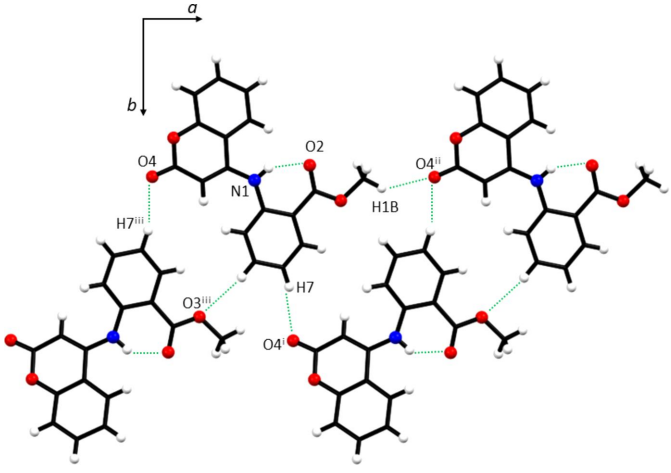

Figure 6
Supramolecular array of **1**. [Symmetry codes: (i) $x - \frac{1}{2}, -y + 2, z$; (ii) $x - 1, y, z$; (iii) $x + \frac{1}{2}, -y + 2, z$.]

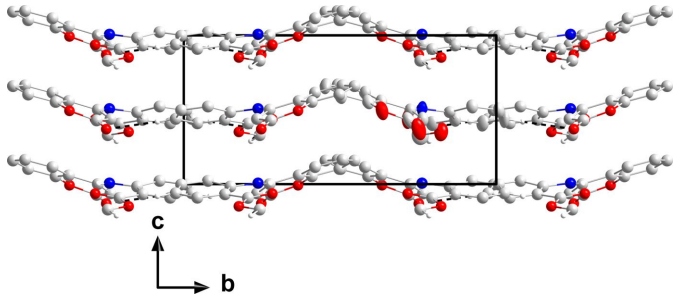

Figure 7
Packing viewed along the *a*-axis direction. The C—H···O hydrogen bonds are depicted by dashed lines and non-interacting H atoms have been omitted for clarity.

5. Synthesis and crystallization

The reaction was carried out according to the literature (Carneiro *et al.*, 2021) (Scheme 1). A mixture of **A** and the aniline **B** (2 equiv.) was heated in a 50 ml Becher at 453 K for 1 h. A solution comprised of 30 ml of hot methanol and 30 ml of aqueous NaOH (1 mol l^{-1}) was then added to the solid. This mixture was stirred for 30 min at 333 K and then filtered. The solid was washed with water, dried and used without further purification.

6. Refinement

Crystal data, data collection and structure refinement details are summarized in Table 2.

Acknowledgements

The authors would like to acknowledge LDRX (Laboratório Multiusuário de Difração de Raios-X da UFF) for the support with the X-ray diffraction facility (D8-Venture). The authors are also grateful to CAPLH/PUC-Rio for the use of the NMR facilities.

Funding information

Funding for this research was provided by: Coordenação de Aperfeiçoamento de Pessoal de Nível Superior (grant No. E-26/202.720/2018); Fundação Carlos Chagas Filho de Amparo à Pesquisa do Estado do Rio de Janeiro (grant No. E-26/201.314/2022); Conselho Nacional de Desenvolvimento Científico e Tecnológico (grant No. 304671/2020-7).

References

Ait-Ramdane-Terbouche, C., Abdeldjebar, H., Terbouche, A., Lakhdari, H., Bachari, K., Roisnel, T. & Hauchard, D. (2020). *J. Mol. Struct.* **1222**, 128918.

Annunziata, F., Pinna, C., Dallavalle, S., Tamborini, L. & Pinto, A. (2020). *Int. J. Mol. Sci.* **21**, 1–83.

Bansal, Y., Sethi, P. & Bansal, G. (2013). *Med. Chem. Res.* **22**, 3049–3060.

Belladona, A. L., Cardoso Dilelio, M., Cargnelutti, R., Barcellos, T., Cruz Silveira, C. & Schumacher, R. F. (2023). *ChemistrySelect*, **8**, 202300377.

Bor, T., Aljaloud, S. O., Gyawali, R. & Ibrahim, S. A. (2016). *Fruits, Vegetables, and Herbs: Bioactive Foods in Health Promotion*, edited by R. R. Watson & V. R. Preedy. pp. 551–578. New York: Academic Press.

Bruker (2021). *APEX4* and *SAINT*. Bruker AXS Inc., Madison, Wisconsin, USA.

Campbell, J. L. E., Barton, R. J., Gear, J. R., Conlin, G. M. & Robertson, B. E. (1995). *J. Chem. Crystallogr.* **25**, 245–248.

Cao, D., Liu, Z., Verwilst, P., Koo, S., Jangjili, P., Kim, J. S. & Lin, W. (2019). *Chem. Rev.* **119**, 10403–10519.

Carneiro, L. S. A., Almeida-Souza, F., Lopes, Y. S. C., Novas, R. C. V., Santos, K. B. A., Ligiero, C. B. P., Calabrese, K. D. S. & Buarque, C. D. (2021). *Bioorg. Chem.* **114**, 105141.

Emam, S. H., Hassan, R. A., Osman, E. O., Hamed, M. I. A., Abdou, A. M., Kandil, M. M., Elbaz, E. M. & Mikhail, D. S. (2023). *Drug Dev. Res.* **84**, 433–457.

Groom, C. R., Bruno, I. J., Lightfoot, M. P. & Ward, S. C. (2016). *Acta Cryst.* B**72**, 171–179.

Krause, L., Herbst-Irmer, R., Sheldrick, G. M. & Stalke, D. (2015). *J. Appl. Cryst.* **48**, 3–10.

Kumar, K., Ramulu, M. S. & Kumar, N. P. (2018). *New J. Chem.* **42**, 11276–11279.

Liu, Q. M., Zhang, Y. F., Gao, Y. Y., Liu, H., Cao, M. J., Yang, X. W., Su, W. J. & Liu, G. M. (2019). *Food Funct.* **10**, 6767–6778.

Parsons, S., Flack, H. D. & Wagner, T. (2013). *Acta Cryst.* B**69**, 249–259.

Regal, M. K. A., Shaban, S. S. & El–Metwally, S. A. (2020). *J. Heterocycl. Chem.* **57**, 1368–1378.

Rosa, W. C., Rocha, I. O., Schmitz, B. F., Martins, M. A. P., Zanatta, N., Tisoco, I., Iglesias, B. A. & Bonacorso, H. G. (2021). *J. Fluor. Chem.* **248**, 109822.

Sharapov, A. D., Fatykhov, R. F., Khalymbadzha, I. A., Zyryanov, G. V., Chupakhin, O. N. & Tsurkan, M. V. (2023). *Int. J. Mol. Sci.* **24**, 2839.

Sheldrick, G. M. (2015*a*). *Acta Cryst.* A**71**, 3–8.

Sheldrick, G. M. (2015*b*). *Acta Cryst.* C**71**, 3–8.

Xu, Z., Chen, Q., Zhang, Y. & Liang, C. (2021). *Fitoterapia*, **150**, 104863.

Yildirim, M., Poyraz, S. & Ersatir, M. (2023). *Med. Chem. Res.* **32**, 617–642.

supporting information

Acta Cryst. (2023). E**79**, 842-846 [https://doi.org/10.1107/S2056989023007351]

Synthesis, characterization and crystal structure of methyl 2-(2-oxo-2*H*-chromen-4-ylamino)benzoate

Henrique V. P. Hollauer, Rachel C. Vilas Novas, Guilherme P. Guedes, Camilla D. Buarque and Lívia B. L. Escobar

Computing details

Data collection: *APEX4* (Bruker, 2021); cell refinement: *SAINT* (Bruker, 2021); data reduction: *SAINT* (Bruker, 2021); program(s) used to solve structure: SHELXT2018 (Sheldrick, 2015*a*); program(s) used to refine structure: *SHELXL2018* (Sheldrick, 2015*b*).

Methyl 2-(2-oxo-2*H*-chromen-4-yl)benzoate

Crystal data

$C_{17}H_{13}NO_4$
M_r = 295.28
Orthorhombic, $Pca2_1$
a = 12.7698 (16) Å
b = 14.9212 (18) Å
c = 7.1087 (8) Å
V = 1354.5 (3) Å^3
Z = 4
$F(000)$ = 616
D_x = 1.448 Mg m^{-3}
Mo $K\alpha$ radiation, λ = 0.71073 Å
Cell parameters from 2328 reflections
θ = 2.1–25.0°
μ = 0.10 mm^{-1}
T = 298 K
Prismatic, yellow
0.39 × 0.08 × 0.06 mm

Data collection

Bruker D8 Venture diffractometer
φ and ω scans
Absorption correction: multi-scan (*SADABS*; Krause *et al.*, 2015)
T_{min} = 0.666, T_{max} = 0.745
35019 measured reflections
2328 independent reflections
2096 reflections with $I > 2\sigma(I)$
R_{int} = 0.102
θ_{max} = 25.0°, θ_{min} = 2.1°
h = −15→15
k = −17→17
l = −7→8

Refinement

Refinement on F^2
Least-squares matrix: full
$R[F^2 > 2\sigma(F^2)]$ = 0.066
$wR(F^2)$ = 0.158
S = 1.08
2328 reflections
204 parameters
1 restraint
Primary atom site location: dual
Secondary atom site location: difference Fourier map
Hydrogen site location: mixed
H atoms treated by a mixture of independent and constrained refinement
$w = 1/[\sigma^2(F_o^2) + (0.0648P)^2 + 1.5253P]$ where $P = (F_o^2 + 2F_c^2)/3$
$(\Delta/\sigma)_{max} < 0.001$
$\Delta\rho_{max}$ = 0.25 e Å^{-3}
$\Delta\rho_{min}$ = −0.37 e Å^{-3}

Absolute structure: Flack *x* determined using 771 quotients [(I+)-(I-)]/[(I+)+(I-)] (Parsons *et al.*, 2013)
Absolute structure parameter: 0.2 (7)

Special details

Geometry. All esds (except the esd in the dihedral angle between two l.s. planes) are estimated using the full covariance matrix. The cell esds are taken into account individually in the estimation of esds in distances, angles and torsion angles; correlations between esds in cell parameters are only used when they are defined by crystal symmetry. An approximate (isotropic) treatment of cell esds is used for estimating esds involving l.s. planes.

Fractional atomic coordinates and isotropic or equivalent isotropic displacement parameters (Å²)

	x	*y*	*z*	U_{iso}*/U_{eq}
O1	0.4084 (3)	0.8237 (3)	0.3512 (7)	0.0553 (12)
O2	0.5181 (3)	0.7166 (2)	0.4363 (8)	0.0536 (12)
O3	1.0000 (3)	0.6344 (3)	0.4928 (7)	0.0527 (12)
O4	1.0759 (3)	0.7520 (3)	0.3698 (9)	0.0669 (15)
N1	0.7132 (3)	0.7623 (3)	0.5069 (7)	0.0364 (11)
H1	0.664 (4)	0.725 (4)	0.502 (8)	0.032 (15)*
C1	0.3280 (5)	0.7569 (5)	0.3295 (12)	0.067 (2)
H1A	0.349617	0.713581	0.237447	0.101*
H1B	0.264282	0.785039	0.288804	0.101*
H1C	0.316334	0.727407	0.447724	0.101*
C2	0.5005 (4)	0.7946 (4)	0.4076 (9)	0.0405 (13)
C3	0.5768 (4)	0.8683 (3)	0.4321 (8)	0.0367 (13)
C4	0.6811 (4)	0.8507 (3)	0.4842 (8)	0.0326 (11)
C5	0.7468 (4)	0.9226 (3)	0.5221 (8)	0.0387 (13)
H5	0.814613	0.912215	0.564520	0.046*
C6	0.7126 (5)	1.0084 (4)	0.4974 (10)	0.0477 (15)
H6	0.758040	1.055801	0.520819	0.057*
C7	0.6125 (5)	1.0258 (3)	0.4388 (11)	0.0539 (17)
H7	0.590562	1.084558	0.419550	0.065*
C8	0.5454 (4)	0.9566 (4)	0.4089 (10)	0.0476 (15)
H8	0.476977	0.968658	0.372170	0.057*
C9	0.8095 (4)	0.7251 (3)	0.5005 (8)	0.0325 (11)
C10	0.8978 (4)	0.7656 (3)	0.4380 (9)	0.0385 (13)
H10	0.894045	0.825120	0.399951	0.046*
C11	0.9952 (4)	0.7211 (4)	0.4284 (10)	0.0469 (15)
C12	0.9119 (4)	0.5900 (4)	0.5527 (9)	0.0401 (13)
C13	0.8153 (4)	0.6322 (3)	0.5592 (8)	0.0342 (12)
C14	0.7308 (4)	0.5799 (3)	0.6151 (8)	0.0371 (13)
H14	0.664447	0.605621	0.619064	0.045*
C15	0.7421 (6)	0.4924 (4)	0.6640 (9)	0.0467 (14)
H15	0.684223	0.458872	0.700802	0.056*
C16	0.8405 (5)	0.4536 (4)	0.6587 (10)	0.0549 (17)
H16	0.848964	0.394016	0.694065	0.066*
C17	0.9249 (5)	0.5021 (4)	0.6022 (11)	0.058 (2)
H17	0.990900	0.475834	0.597178	0.069*

Atomic displacement parameters (Å²)

	U^{11}	U^{22}	U^{33}	U^{12}	U^{13}	U^{23}
O1	0.033 (2)	0.047 (2)	0.086 (3)	0.0037 (19)	−0.006 (2)	0.004 (2)
O2	0.034 (2)	0.034 (2)	0.093 (4)	−0.0002 (17)	0.001 (2)	0.001 (2)
O3	0.034 (2)	0.039 (2)	0.085 (3)	0.0077 (16)	−0.006 (2)	−0.011 (2)
O4	0.031 (2)	0.053 (3)	0.117 (4)	−0.009 (2)	0.014 (2)	−0.020 (3)
N1	0.028 (2)	0.024 (2)	0.057 (3)	0.0006 (18)	0.001 (2)	0.004 (2)
C1	0.034 (3)	0.073 (5)	0.095 (6)	−0.006 (3)	−0.002 (4)	0.000 (4)
C2	0.028 (3)	0.038 (3)	0.055 (4)	0.008 (2)	0.008 (3)	−0.001 (3)
C3	0.032 (3)	0.031 (3)	0.046 (3)	0.006 (2)	0.006 (2)	−0.002 (2)
C4	0.035 (3)	0.032 (2)	0.030 (3)	0.005 (2)	0.003 (2)	0.000 (2)
C5	0.035 (3)	0.034 (3)	0.047 (3)	0.000 (2)	−0.002 (3)	−0.002 (3)
C6	0.054 (4)	0.031 (3)	0.058 (4)	−0.004 (2)	0.004 (3)	−0.004 (3)
C7	0.056 (4)	0.025 (3)	0.081 (5)	0.011 (3)	0.005 (4)	0.001 (3)
C8	0.038 (3)	0.038 (3)	0.066 (4)	0.014 (2)	0.003 (3)	0.004 (3)
C9	0.032 (3)	0.028 (2)	0.037 (3)	0.002 (2)	−0.003 (2)	−0.003 (2)
C10	0.035 (3)	0.029 (3)	0.051 (3)	−0.001 (2)	−0.002 (3)	−0.003 (2)
C11	0.031 (3)	0.042 (3)	0.068 (4)	−0.001 (2)	−0.001 (3)	−0.021 (3)
C12	0.034 (3)	0.034 (3)	0.052 (3)	0.003 (2)	−0.009 (3)	−0.007 (3)
C13	0.035 (3)	0.028 (3)	0.040 (3)	0.005 (2)	−0.006 (2)	−0.005 (2)
C14	0.037 (3)	0.029 (3)	0.045 (3)	0.006 (2)	−0.001 (2)	−0.001 (2)
C15	0.057 (4)	0.035 (3)	0.048 (4)	−0.005 (3)	−0.001 (3)	0.002 (3)
C16	0.069 (4)	0.032 (3)	0.064 (4)	0.006 (3)	−0.018 (4)	0.004 (3)
C17	0.046 (3)	0.041 (4)	0.087 (5)	0.021 (3)	−0.024 (4)	−0.007 (3)

Geometric parameters (Å, º)

O1—C2	1.316 (7)	C6—H6	0.9300
O1—C1	1.440 (8)	C7—C8	1.358 (8)
O2—C2	1.203 (6)	C7—H7	0.9300
O3—C12	1.373 (7)	C8—H8	0.9300
O3—C11	1.374 (7)	C9—C10	1.353 (7)
O4—C11	1.204 (7)	C9—C13	1.450 (7)
N1—C9	1.351 (6)	C10—C11	1.412 (7)
N1—C4	1.391 (6)	C10—H10	0.9300
N1—H1	0.84 (6)	C12—C17	1.367 (8)
C1—H1A	0.9600	C12—C13	1.385 (7)
C1—H1B	0.9600	C13—C14	1.390 (7)
C1—H1C	0.9600	C14—C15	1.359 (7)
C2—C3	1.479 (7)	C14—H14	0.9300
C3—C8	1.387 (7)	C15—C16	1.385 (10)
C3—C4	1.407 (7)	C15—H15	0.9300
C4—C5	1.388 (7)	C16—C17	1.359 (10)
C5—C6	1.363 (8)	C16—H16	0.9300
C5—H5	0.9300	C17—H17	0.9300
C6—C7	1.370 (9)		

C2—O1—C1	116.2 (5)	C7—C8—H8	119.3
C12—O3—C11	121.5 (4)	C3—C8—H8	119.3
C9—N1—C4	130.9 (4)	N1—C9—C10	125.8 (5)
C9—N1—H1	114 (4)	N1—C9—C13	115.5 (4)
C4—N1—H1	114 (4)	C10—C9—C13	118.6 (4)
O1—C1—H1A	109.5	C9—C10—C11	122.7 (5)
O1—C1—H1B	109.5	C9—C10—H10	118.7
H1A—C1—H1B	109.5	C11—C10—H10	118.7
O1—C1—H1C	109.5	O4—C11—O3	116.0 (5)
H1A—C1—H1C	109.5	O4—C11—C10	126.3 (6)
H1B—C1—H1C	109.5	O3—C11—C10	117.7 (5)
O2—C2—O1	122.5 (5)	C17—C12—O3	116.3 (5)
O2—C2—C3	125.2 (5)	C17—C12—C13	122.4 (6)
O1—C2—C3	112.3 (4)	O3—C12—C13	121.3 (5)
C8—C3—C4	118.8 (5)	C12—C13—C14	116.5 (5)
C8—C3—C2	120.1 (5)	C12—C13—C9	118.1 (5)
C4—C3—C2	121.1 (4)	C14—C13—C9	125.4 (5)
C5—C4—N1	122.2 (5)	C15—C14—C13	121.9 (6)
C5—C4—C3	118.7 (5)	C15—C14—H14	119.0
N1—C4—C3	119.0 (5)	C13—C14—H14	119.0
C6—C5—C4	120.4 (5)	C14—C15—C16	119.4 (6)
C6—C5—H5	119.8	C14—C15—H15	120.3
C4—C5—H5	119.8	C16—C15—H15	120.3
C5—C6—C7	121.1 (5)	C17—C16—C15	120.3 (6)
C5—C6—H6	119.5	C17—C16—H16	119.8
C7—C6—H6	119.5	C15—C16—H16	119.8
C8—C7—C6	119.4 (5)	C16—C17—C12	119.4 (6)
C8—C7—H7	120.3	C16—C17—H17	120.3
C6—C7—H7	120.3	C12—C17—H17	120.3
C7—C8—C3	121.5 (5)		

C1—O1—C2—O2	1.4 (10)	C13—C9—C10—C11	−0.2 (9)
C1—O1—C2—C3	−178.0 (6)	C12—O3—C11—O4	−176.1 (6)
O2—C2—C3—C8	−174.9 (7)	C12—O3—C11—C10	4.4 (9)
O1—C2—C3—C8	4.5 (8)	C9—C10—C11—O4	177.8 (7)
O2—C2—C3—C4	3.2 (9)	C9—C10—C11—O3	−2.7 (9)
O1—C2—C3—C4	−177.3 (5)	C11—O3—C12—C17	175.9 (6)
C9—N1—C4—C5	−26.1 (9)	C11—O3—C12—C13	−3.2 (8)
C9—N1—C4—C3	157.9 (6)	C17—C12—C13—C14	−1.4 (9)
C8—C3—C4—C5	4.0 (8)	O3—C12—C13—C14	177.6 (6)
C2—C3—C4—C5	−174.2 (6)	C17—C12—C13—C9	−178.9 (6)
C8—C3—C4—N1	−179.7 (6)	O3—C12—C13—C9	0.1 (8)
C2—C3—C4—N1	2.1 (8)	N1—C9—C13—C12	179.0 (5)
N1—C4—C5—C6	179.8 (6)	C10—C9—C13—C12	1.6 (8)
C3—C4—C5—C6	−4.2 (9)	N1—C9—C13—C14	1.7 (8)
C4—C5—C6—C7	1.4 (10)	C10—C9—C13—C14	−175.7 (5)
C5—C6—C7—C8	1.6 (11)	C12—C13—C14—C15	1.1 (8)
C6—C7—C8—C3	−1.6 (11)	C9—C13—C14—C15	178.4 (6)

C4—C3—C8—C7	−1.2 (10)	C13—C14—C15—C16	0.1 (9)
C2—C3—C8—C7	177.0 (7)	C14—C15—C16—C17	−1.1 (10)
C4—N1—C9—C10	−11.9 (10)	C15—C16—C17—C12	0.8 (10)
C4—N1—C9—C13	171.0 (6)	O3—C12—C17—C16	−178.6 (6)
N1—C9—C10—C11	−177.3 (6)	C13—C12—C17—C16	0.5 (10)

Hydrogen-bond geometry (Å, º)

D—H···*A*	*D*—H	H···*A*	*D*···*A*	*D*—H···*A*
C1—H1*B*···O4^{i}	0.96	2.52	3.232 (8)	131
C7—H7···O4^{ii}	0.93	2.47	3.387 (6)	167
N1—H1···O2	0.84 (6)	1.92 (6)	2.631 (6)	141 (5)

Symmetry codes: (i) *x*−1, *y*, *z*; (ii) *x*−1/2, −*y*+2, *z*.

Journal of Molecular Structure 1306 (2024) 137811

Contents lists available at ScienceDirect

Journal of Molecular Structure

journal homepage: www.elsevier.com/locate/molstr

Synthesis, crystal structure and magnetic properties of two 1D coordination polymers containing Co^{2+} and Cu^{2+} ions and 1,3,5-tris(4-carboxylphenyl) benzene

Henrique V.P. Hollauer [a], Gabriel S. de Araújo [a], Guilherme P. Guedes [b], Henrique C.S. Junior [b], Sonia Letichevsky [c], Luis Ghivelder [d], Stéphane Soriano [e], Odivaldo Cambraia [b], Lívia B. L. Escobar [a,*]

[a] Departamento de Química, Pontifícia Universidade Católica do Rio de Janeiro, Rio de Janeiro-RJ, 22451-900, Brazil
[b] Instituto de Química, Universidade Federal Fluminense, Niterói-RJ, 24020-141, Brazil
[c] Departamento de Engenharia Química e de Materiais, Pontifícia Universidade Católica do Rio de Janeiro, Rio de Janeiro-RJ, 22451-900, Brazil
[d] Instituto de Física, Universidade Federal do Rio de Janeiro, Rio de Janeiro, Rio de Janeiro, 21941-909, Brazil
[e] Instituto de Física, Universidade Federal Fluminense, Niterói-RJ, 24210-346, Brazil

ARTICLE INFO

Keywords:
Coordination polymers
Magnetic properties

ABSTRACT

Two 1D coordination polymers, $\{[Co(H_3BTB)_2(phen)](NO_3)_2\}_n$ (**1**) and $\{[Cu(HBTB)_2(phen)]\ DMF\}_n$ (**2**), were synthesized through a slow diffusion reaction between the metal ions Co^{2+} or Cu^{2+}, 1,3,5-tris(4-carboxylphenyl) benzene (H_3BTB) and 1,10-phenanthroline (phen). Single-crystal X-ray diffraction revealed that both metal centers are involved in a distorted octahedral environment. As expected for a Cu^{2+} ion with a d^9 configuration, a pronounced *Jahn-Teller* distortion is observed. FTIR, powder XRD, and thermogravimetric analysis were employed for the chemical characterization of the two complexes. CASSCF-NEVPT2 was used to calculate the axial magnetic anisotropy (D) for complex **1**, and the results were almost perfectly consistent with the experimental measurements. The *AC* magnetic susceptibility measurements revealed field-induced single-ion magnet (SIM) behavior at low temperatures for **1**. EPR studies of complex **2** indicated that the Cu^{2+} ions are essentially isolated.

1. Introduction

Coordination polymers (CPs) are materials that have recently received notable attention due to their reported applications in different areas, such as catalysis, luminescent materials, gas adsorption, magnetism, and so on [1–3]. These compounds consist of uni- or polynuclear complexes with different organic ligands formed by covalent bonds that generate one-, two, or three-dimensional structures [2,3].

One of the most common ligands used to produce CPs is the polycarboxylic acid ligand. These molecules are interesting for developing this type of material because they have high structural stability, the ability to propagate magnetic interactions, several coordination sites, and the possibility of forming highly porous materials. These properties are crucial for good gas adsorption [4,5].

1,3,5-Tris(4-carboxylphenyl)benzene (H_3BTB) is a polycarboxylic acid of interest due to its six coordination sites and high electronic delocalization ability, and is well suited to synthesize many coordination polymers such as metal-organic frameworks (MOFs) due to its large size and high structure variety, being able to form different types of networks [6,7]. In 2019, Sapianik and coworkers reported interesting work on the preparation of MOFs containing the H_3BTB ligand, pivalic acid, and the metal ions Zn^{2+} and Co^{2+}. The layered compounds demonstrate permanent porosity with a BET surface area of up to 688 $m^2 \cdot g^{-1}$ and the possibility of selective gas adsorption (CO_2 over N_2 and CH_4) [8]. Moreover, H_3BTB has great potential as a classic π-conjugated organic lumiphore [9].

MOFs present several fascinating applications. For instance, modified MOFs with magnetic properties provide robust platforms for solving the pollution of water bodies caused by adsorbents. In the work published by Wang and coworkers in 2020 [10], they used a MOF formed by a very similar H_3BTB ligand and Co^{2+} to adhere to the Fe_3O_4 surface by m-phenylenediamine. The material called Fe_3O_4@PmPD–[Co-BT] had

* Corresponding author.
E-mail address: liviablescobar@puc-rio.br (L.B.L. Escobar).

https://doi.org/10.1016/j.molstruc.2024.137811
Received 28 December 2023; Received in revised form 1 February 2024; Accepted 15 February 2024
Available online 20 February 2024

notable adsorption performance for the CR dye, and the adsorption capacity could reach 347.8 mg g^{-1} at room temperature [10].

Many variables can affect the structure and properties of coordination polymers, and the insertion of auxiliary ligands has been the topic of many investigations [11]. Thus, the use of N-donor ligands such as 1, 10-phenanthroline can generate different topologies [7]. Recently, Coban published an article reporting the crystal structure and luminescence properties of a *3D* Ho(III)-based polymer [12]. Each Ho(III) ion in this polymer is octacoordinated to six carboxylic oxygen atoms from BTB^{3-} and two nitrogen atoms from the phen ligand, forming a distorted square antiprismatic coordination geometry. Moreover, the complex is a promising material for luminescent probes [12].

Recently, the design of CPs with molecular nanomagnet behavior has received a lot of interest due to their potential applications in quantum computing, molecular spintronics, etc. [13]. In addition to lanthanide Single Ions Magnets (SIMs), SIMs with *3d* metal centers also have aroused growing interest. In the last decade, a large number of *3d* SIMs with different metal centers was reported. Among all these SIMs, the Co^{2+} complexes are of special interest. For this Kramers ion, slow magnetic relaxation can be observed under a DC field, due to its orbital contribution to the magnetic moment, resulting in high magnetic anisotropy with various geometries [15,16].

An interesting work published recently by Wakizaka and coworkers shows the results of the first example of single ion magnet in Zn^{2+} metal–organic frameworks (MOFs) and hybrid organic–inorganic perovskites (HOIPs) doped with Co^{2+} ions. The doped Co^{2+} sites in the MOFs perform as SIM with a positive D term of zero-field splitting. The longest magnetic relaxation time measured is 150 ms (0.2 mol% Co) at 1.8 K under a static field of 0.1 T [14].

In this work, we synthesized two one-dimensional CPs with Co^{2+} and Cu^{2+} ions containing both 1,3,5-tris(4-carboxylphenyl)benzene (H_3BTB) and 1,10-phenanthroline ligands and studied their magnetic properties.

2. Experimental

2.1. Synthesis

Complexes **1** and **2** were synthesized through slow diffusion.

$\{[Co(H_3BTB)_2(phen)](NO_3)_2\}_n$ (**1**): 5 mL of distilled water containing cobalt nitrate hexahydrate (13.6 mg, 0.06 mmol) was added to a 5 mL solution of DMF containing H_3BTB (50.0 mg, 0.11 mmol) and phenanthroline (10.3 mg, 0.06 mmol). Dark-pink crystals suitable for single-crystal X-ray analysis were formed a few days after slow evaporation at room temperature. Yield: 32.65 %. IR (cm^{-1}): υ(C═O) 1674;υ (C═C) 1642, 1596, 1562, 1514; υ (C—N)1641; τ(CCCC) 844, 774.

$\{[Cu(HBTB)_2(phen)]\ DMF\}_n$ (**2**): Similarly to complex **1**, for complex **2**, 5 mL of distilled water containing copper(II) chloride hexahydrate (9.4 mg, 0.06 mmol) was added to a 5 mL solution of DMF containing H_3BTB (50.0 mg, 0.11 mmol) and phenanthroline (10.3 mg, 0.06 mmol). Blue crystals suitable for single-crystal X-ray analysis were formed a few days after slow evaporation at room temperature. Yield: 50.49 %. IR (cm^{-1}): υ(C═O) 1670;υ (C═C) 1639, 1547, 1567, 1517, 1421, υ(C—N) 1641; τ(CCCC) 844, 774.

2.2. Instrumentation

FTIR analyses were performed in ATR mode using 32 scans and a resolution of 4 cm^{-1} using an Alpha II spectrometer (Bruker). Thermogravimetry was conducted with a Perkin-Elmer Pyris 1 TGA analyzer under a nitrogen atmosphere at 25–800 °C and a heating rate of 10 °C min^{-1}.

Powder X-ray diffraction data for all the samples were collected on a Bruker D8 Discover instrument equipped with a copper tube, nickel filter, and Lynxeye detector. The scans were obtained in the 2θ range 5 to 60°, with a step of 0.02° and 0.5 s per step. A beam knife was used to reduce air scattering.

Single-crystal X-ray diffraction data for compounds **1** and **2** were collected on a Bruker D8 Venture diffractometer with Mo Kα (λ = 0.71073 Å) radiation at 298 K. Data collection and cell refinement were performed with Bruker Instrument Service v4.2.2 and APEX4, [15], respectively. Data reduction was carried out using SAINT [16]. Empirical multiscan absorption correction using equivalent reflections was performed with the SADABS program [17]. All the crystal structures were solved and refined using the SHELXS and SHELXL packages [18]. The structures were drawn using the ORTEP-3 for Windows [19] and Mercury programs [20]. Summaries of the crystal data, data collection, and refinement for compounds **1** and **2** are listed in Table 1. The selected bond lengths and bond angles are summarized in Table S1.

CCDC 2321446 and 2321447 contains the supplementary crystallographic data for this paper. These data can be obtained free of charge from The Cambridge Crystallographic Data Centre via www.ccdc.cam.ac.uk/data_request/cif.

Magnetic field measurements were performed using a vibrating sample magnetometer (VSM) and an AC Measurement System (ACMS) operating in accordance with the Quantum Design Physical Properties Measurement System (PPMS). The data were corrected based on the diamagnetic contributions of both the sample holder and the sample. The Magprop routine of the Dave program [21] was employed for the static magnetic data fitting process.

The electronic paramagnetic resonance (EPR) spectrum of **2** was recorded in the solid-state (300 K) on a Bruker EMX-Plus spectrometer with an X-band cavity (9.5 GHz) and a microwave power of 10 mW. The spectrum was simulated using the EasySpin [22] MATLAB routine.

2.3. Computational details

Quantum mechanical studies of compounds **1** and **2** were performed using the ORCA package [23–25]. The molecular frameworks used for theoretical calculations are based on the crystal structure solved by single-crystal X-ray diffraction, with only hydrogen atoms reoptimized using the PBEh-3c [26] compound method. To reduce computational costs during CASSCF calculations, the molecular framework in compound **1** used a simplified version of the ligands without changing the

Table 1
Crystal data and refinement results for complexes **1** and **2**.

	$\{[Co(H_3BTB)_2(phen)](NO_3)_2\}_n$	$\{[Cu(HBTB)_2(phen)]DMF\}_n$
Formula	$C_{66}H_{44}CoN_4O_{18}$	$C_{72}H_{54}CuN_4O_{14}$
Formula weight	1239.98	1262.73
Crystal system	Monoclinic	Monoclinic
Space group	C2/c	C2/c
a (Å)	18.2202(7)	18.3706(10)
b (Å)	11.0533(4)	11.0279(6)
c (Å)	31.7162(10)	31.8192(18)
α (°)	90	90
β (°)	97.1750(10)	98.864(2)
Y (°)	90	90
V (Å^3)	6337.4(4)	6369.24
Z	4	4
Crystal size (mm)	0.632×0.576×0.410	0.249×0.201×0.103
Dcalc (g cm^{-3})	1.295	1.317
μ(Mo Kα) (cm^{-1})	0.344	0.413
T_{min}/T_{max}	0.805/0.868	0.905/0.958
Measured reflections	198,860	160,529
Unique reflections	6503	7319
Observed reflections	5978	5877
No. parameters	440	417
R ($[F^2 > 2\sigma(F^2)]$)	0.053	0.0517
w*R*	0.152	0.1727
S	1.05	1.203
CCDC No.	2321446	2321447

immediate coordination environment of the cobalt ion (Figure S7).

Broken symmetry calculations for compound **2** were performed using density functional theory with the UKS TPSS/Def2-TZVP [27,28] level. All magnetic exchange interactions were evaluated based on the isotropic Heisenberg-Dirac-van Vleck (HDvV) Hamiltonian [29] for dimeric interactions (Eq. (1)) [30], and the effective exchange coupling constant (J) was obtained from Eq. (2), as proposed by Soda et al. [31].

$$\widehat{H} = -J_{AB}S_AS_B \tag{1}$$

$$J_{AB} = -\frac{(E_{HS} - E_{BS})}{\langle S^2\rangle_{HS} - \langle S^2\rangle_{BS}} \tag{2}$$

Electronic and magnetic features were evaluated using TPSS/Def2-TZVP [32] as the initial orbital guess and the State-Averaged Complete Active Self-Consistent Field (SA-CASSCF) [33] with the Def2-TZVP basis set with the Resolution of Identity (RI) Coulomb integral approximation scheme and the *N*-Electron Valence State Perturbation Theory (NEVPT2) [34] as the perturbational treatment. The SA-CASSCF calculation was performed on 10 quartets and 40 doublet states, with an active space containing the 7 *d* valence electrons from the Co^{2+} ion. Spin-orbit coupling (SOC) contributions to zero-field splitting (ZFS) were calculated using SA-CASSCF+NEVPT2 wavefunctions by applying the quasidegenerate perturbation theory (QDPT) [35]. Axial and rhombic ZFS parameters D and E were obtained using Effective Spin Hamiltonian Theory [36]. The reference axis that diagonalizes the ZFS parameters was chosen to fulfill the condition that $0 \leq E/D \leq 1/3$ [37]. Crystal field (CF) parameters were obtained with the application of the Ab Initio Ligand-Field Theory (AILFT) implemented by Neese et al. [38] in the ORCA package.

3. Results and discussion

3.1. Crystal structures

Powder X-ray diffraction patterns for compounds **1** and **2** were compared with the simulated patterns predicted from the crystal structure. The experimental and simulated powder XRD patterns corresponded well to the peak positions and relative intensities, confirming the crystalline phase purity of the compounds (see the SI for details, Figures S1 and S2).

Complexes **1** and **2** are isostructural compounds crystalizing in a monoclinic crystal system with space group C2/c. The asymmetric units of these complexes are shown in Figures S3 and S4. A representative fragment of the crystal structure of polymers **1** and **2** is shown in Fig. 1a. Both metal ions present a slightly distorted octahedral environment (Fig. 1b) as indicated by continuous shape analysis [39]. They are coordinated to two nitrogen atoms (N1 and N2) from the phen ligand to two oxygen atoms (O2 and $O2^{i}$) in the equatorial position and to two oxygen atoms ($O3^{i}$ and $O3^{ii}$) from the carboxylic ligand in the axial position. In the equatorial plane, the bond distances are M-N1 = 2.115 (3) Å and M-O2 = 2.027(3) Å for **1** and M-N1 = 2.014(3) Å and M-O2 = 1.928(3) Å for **2**. In the axial positions, the bond distances are M-O3 = 2.156(3) Å for **1** and 2.477(3) Å for **2**. It is possible to note the pronounced Jahn-Teller distortion in **2**, as expected for the d^9 configuration. Due to the longer bond distances in the axial positions, both metal centers are involved in an elongated octahedral geometry.

Fig. 2 shows the extension of the polymeric chain along the crystallographic *c* axis. The 1D coordination polymer is formed through the connection of the H_3BTB or $HBTB^{2-}$ anion in **1** and **2**, respectively, which are coordinated with the metal ions via a bridging mechanism. The phen moiety exhibited its usual coordination mode, bidentate chelation. The distance between the connected metal ions along the chain is 16.249(8) Å for **1** and 16.265(8) Å for **2**.

The shortest intermolecular distance between the metal centers is 10.655(8) Å. The equatorial angles around the metal ions are N1-M-$N1^{i}$: 78.79(7)°, N1-M-O1: 91.65(7)° and $O1^{i}$-M-O1: 97.77(7)° for **1**, and N1-M-$N1^{i}$: 82.32(9)°, N1-M-O1: 89.86(9)° and $O1^{i}$-O1: 97.98(9)° for compound **2**. The angle involved in the axial bond $O3^{i}$-M-O3 is 170.94(9)° for **1** and 164.36(9)° for **2**. π−π stacking between the aromatic ring of H_3BTB (1) or the $HBTB^{2-}$ anion (2) builds the supramolecular array, with distances between the rings of approximately 3.71(8)Å. The uncoordinated carboxylic moieties from neighboring chains form intermolecular hydrogen bonds between the hydrogen atoms from O5 and O6, as demonstrated in Fig. 3, along the crystallographic axes *b* and *c*.

3.2. Theoretical calculation

3.2.1. Electronic structure

The SA-CASSCF calculation for complex **1** revealed that the ground state of the molecule is a high spin quartet described by the combination of three main electronic configurations: 36.6 % $(d_{xy})^2(d_{yz})^2(d_{xz})^1(d_{x2-y2})^1(d_{z2})^1$, 32.3 % $(d_{xy})^1(d_{yz})^2(d_{xz})^2(d_{x2-y2})^1(d_{z2})^1$, and 18.1 % $(d_{xy})^2(d_{yz})^1(d_{xz})^2(d_{x2-y2})^1(d_{z2})^1$, followed by two nonnegligible, less than 5 %, contributions confirming the multiconfigurational character of this system. The perturbatively corrected relative ligand-field splitting energies of the *3d* orbitals described by the ab initio ligand-field are (d_{yz}) 0.0 cm^{-1}, (d_{xz}) 99.4 cm^{-1}, (d_{xy}) 587.8 cm^{-1}, (d_{z2}) 6462.0 cm^{-1}, and (d_{x2-y2}) 10,057.4 cm^{-1}. The first electronic doublet state appears well separated from the quartet state by 9254.5 cm^{-1}, ruling out spin-

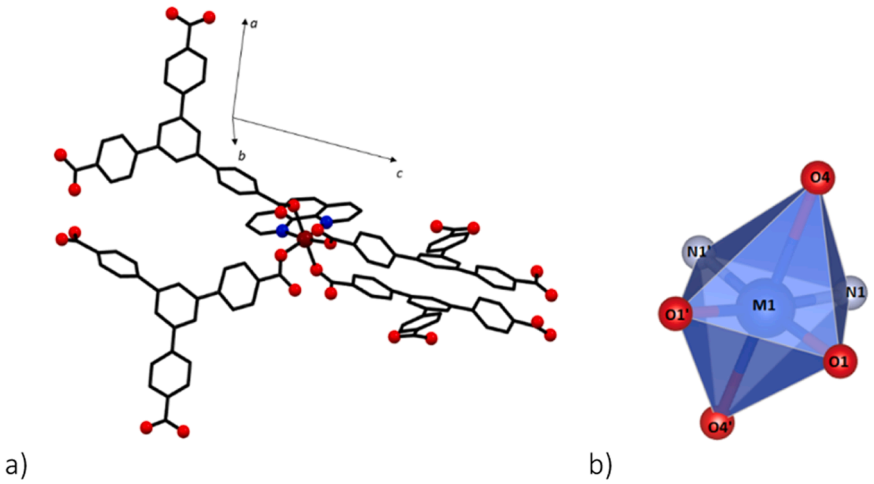

Fig. 1. a) Fragment of the coordination polymers **1** and **2**. For clarity, hydrogen atoms were left out. b) Polyhedral representation of the coordination environment of metal ions in **1** and **2**.

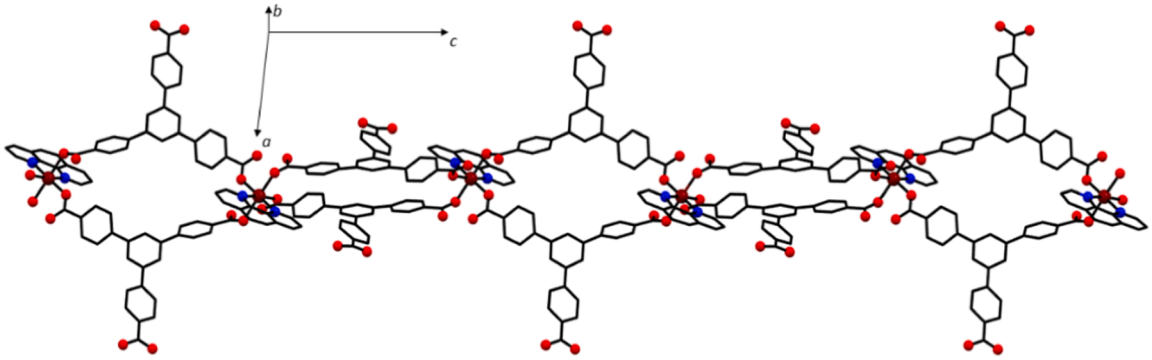

Fig. 2. Extension of the polymeric chain along the crystallographic *c* axis.

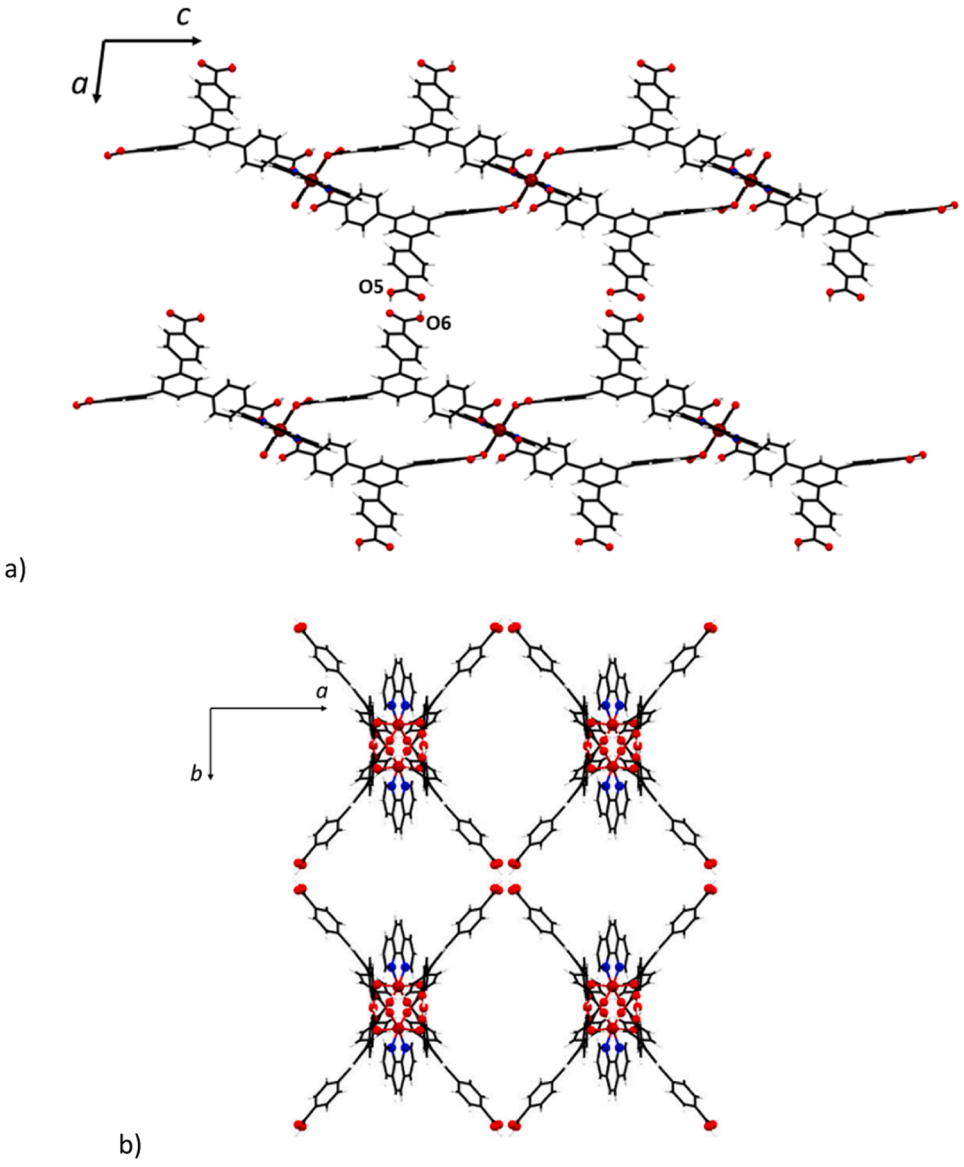

Fig. 3. Representations of the supramolecular interactions through the crystallographic *b axis* a) and *c axis b)*.

crossover. A comparison between the pure SA-CASSCF transition energies and the perturbatively corrected NEVPT2 energies showed that the average correction for the first 10 electronic states was |2132.64| cm^{-1}. This is considerable and indicates that dynamic correlation is a relevant property for describing the electronic state's energies correctly.

3.2.2. Anisotropy, zero-field splitting ab initio calculations and broken symmetry

Since most intermolecular distances separating Co^{2+} ions are significant in complex **1** (Figure S5), with the shortest distance being ~ 10 Å, magnetic exchange interactions are expected to be negligible and are not considered in our computational simulations.

The axial and rhombic anisotropic components D and E obtained by SA-CASSCF+NEVPT2 for **1** using effective Hamiltonian theory (EHT) indicate the absence of an easy magnetization axis. $\boldsymbol{D} = +73.34\ cm^{-1}$ and the relation $\mathbf{E}/\boldsymbol{D} = 0.12$, indicating the formation of an easy plane. The easy plane assumption is supported by **g-tensor** decomposition, which gives $\mathbf{g_x} = 2.02$, $\mathbf{g_y} = 2.53$, $\mathbf{g_z} = 2.71$, and $\mathbf{g_{iso}} = 2.42$. In the same manner, the lowest Kramers doublet appears as an admixture of the effective $|\pm3/2>$ and $|\pm1/2>$ pseudospins, with $|\pm1/2>$ dominating with a total weight of ~56 %, as shown in Scheme 1 below.

For complex **2**, the chance of meaningful magnetic coupling between Cu^{2+} ions was evaluated using the broken-symmetry procedure through the two shortest possible interaction paths of 10.71 and 16.26 Å (Figure S6). In both cases, the computational magnetic coupling constant (J) was observed to be antiferromagnetic and less than $-0.2\ cm^{-1}$ ($-0.19\ cm^{-1}$ and $-0.13\ cm^{-1}$, respectively). As expected, the spin density is strongly localized over the copper(II) ions, and the spin density mostly reflects the d_{yz} orbital for the paths analyzed.

3.3. FTIR

FTIR spectra of H_3BTB, phen, and complexes **1** and **2** were measured in the 4000–400 cm^{-1} range (Figure S7). The presence of a DMF molecule in the crystal lattice of complex **2** can be evidenced by the band at 2975 cm^{-1} (υ_{C-H}). The strong band at 1686 cm^{-1} ($\upsilon_{C=O}$) attributed to the H_3BTB ligand was shifted to 1674 cm^{-1} and 1670 cm^{-1} in **1** and **2**, respectively [12]. The $\upsilon_{CC/CN}$ modes for the free 1,10-phenanthroline ligand at 1644 cm^{-1} and 1505 cm^{-1} appear at 1642 cm^{-1} and 1562 cm^{-1} for **1**, and at 1639 cm^{-1} and 1547 cm^{-1} for **2** [40]. Moreover, its skeletal vibrational peak is found at approximately 1490 cm^{-1}. The alterations in the main vibrational modes of H_3BTB and phen ligands point to their association with metal centers.

3.4. TGA

Thermogravimetric analysis (TGA) was performed on polycrystalline samples of complexes **1** and **2** under a dynamic nitrogen atmosphere (Figures S8 and S9). Figure S3 shows that, for compound 1, three weight loss events occurred. The first one corresponds to the loss of the guest NO_3^- ion from 88 to 99 °C, and the following steps suggest the decomposition of the framework from 331 to 485 °C. Like in complex **1**, the weight loss of **2** is divided into three steps with increasing temperature. In the first step, the weight loss is 7.4 % from 100 to 230 °C, which can be attributed to the loss of the lattice guest DMF molecule. The other two steps correspond to consecutive weight losses of 54.2 % at approximately 300 °C and 28.3 % at 365 to 540 °C, indicating the total collapse of the framework.

3.5. Magnetic properties

The static magnetic properties of compound **1** were investigated in the temperature range of 3K-320 K. The thermal dependence of the $\chi_M T$ product, χ_M is the molar magnetic susceptibility, is shown in Fig. 4. At 320 K, the $\chi_M T$ value of **1** is approximately 2.2 $cm^3\ mol^{-1}\ K$, which is greater than the expected value for uncoupled spin-only contributions (1.88 $cm^3\ mol^{-1}$), indicating the presence of an orbital part in the magnetic moment. Upon cooling, $\chi_M T$ decreases continuously to 1.27 $cm^3\ mol^{-1}\ K$ at 3 K, which can result from antiferromagnetic interactions and/or zero-field splitting (ZFS). To reproduce the magnetic data, only the axial term of the crystal field was considered in the spin Hamiltonian (Eq. 3). Furthermore, the contribution of the magnetic interactions within the compound was included through a mean field approximation.

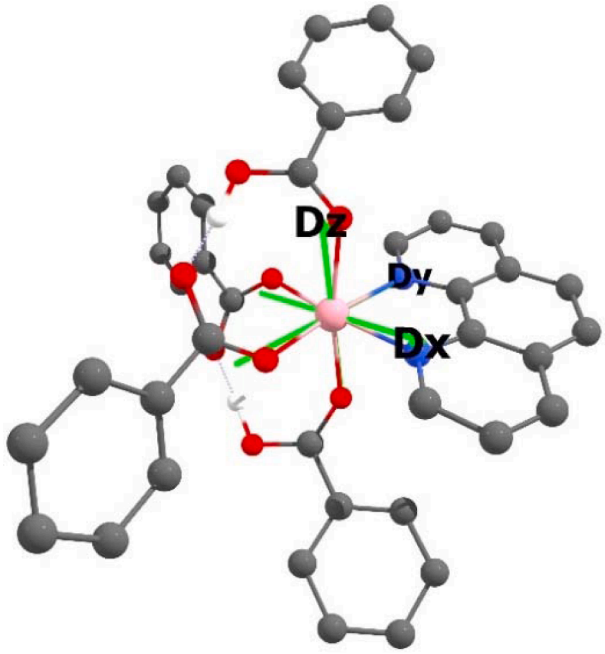

Lowest Kramers Doublet

Weight	Spin	Ms
0.018643	3/2	3/2
0.012496	3/2	3/2
0.313272	3/2	1/2
0.028369	3/2	1/2
0.143811	3/2	-1/2
0.113723	3/2	-1/2
0.273453	3/2	-3/2
0.062776	3/2	-3/2
0.015305	3/2	-3/2

Scheme 1. Complex **1**: Molecular frame relative to the d-tensor eigenframe and description of the lowest Kramers doublet by relative weights and pseudospins (Ms).

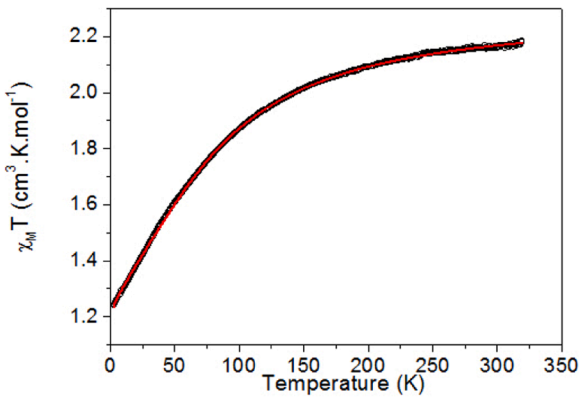

Fig. 4. Thermal dependence of the $\chi_M T$ product for **1**. The red solid line corresponds to the best fit (see text).

$$\hat{H} = \mu_B g \vec{B} \cdot \hat{S} + D\hat{H}_z^2 - zJ'\langle S_z \rangle \hat{H}_z \quad (3)$$

The best fit was achieved for the following parameters: gx = gy = 2.04(1), gz = 2.50(1), D = 74.7(3) cm^{-1} and zJ'= −0.05(1) cm^{-1}. The axial crystal field parameter corresponds to an easy-plane magnetic configuration ($D > 0$) and its value lies within the observed range for octahedral Co^{2+} ions [41] The obtained data agrees with other Co^{2+} Field-induced Single Ion Magnet reported in the literature [42]. In Rey's work, the cobalt complex was obtained using the flexible ligand di (4-pyridyl) sulfide and presented a weak magnetic intermolecular interaction with D = 54.0 cm^{-1} [42].These parameters are in perfect agreement with those obtained from the CASSCF calculations. The mean field parameter confirmed a weak antiferromagnetic interaction within the compound, which was expected from the long distances between the metal centers. This suggests that the magnetic behavior of the compound is mainly governed by the magnetic response of single Co^{2+} ions.

Due to its potential as a single-ion magnet (SIM), the dynamic magnetic response of **1** was studied by measuring the frequency and temperature dependence of the in-phase and out-of-phase magnetic susceptibilities. As commonly observed in cobalt-based SIMs, quantum tunneling of magnetization (QTM) may occur at low temperatures [43]. This relaxation process can be hampered by applying a static magnetic field. Therefore, to infer the best applied field, the frequency-dependent magnetic susceptibilities were measured for different static magnetic fields at 3 K (Figure S10). An optimum magnetic field was obtained for 2 kOe. Under that magnetic field, a clear frequency dependence of the in-phase and out-of-phase magnetic susceptibilities was measured for different temperatures (Fig. 5). The semicircular shape of the Cole–Cole plots (Figure S11) is a signature of a single relaxation time for each temperature, as corroborated by the small values of α which is the width of the relaxation time distribution (Table S2). Hence, the in-phase and out-of-phase data were fitted concurrently by an extended Debye model. The best relaxation times obtained are shown in Table S2 and were used to construct an Arrhenius plot (Fig. 6). From the curvature of this plot, it appears that several relaxation processes occur in the compound. By considering only the high-temperature relaxation times, the effective energy barrier for magnetization reversal (U_{eff}) can be estimated by fitting the data to the Arrhenius law, which gives U_{eff} = 12.1(3) K and $\tau_0 = 5.52(4) \times 10^{-7}$ s (Fig. 6), similar to other Co^{2+} SIM such as the one related by García-López et al., where utilizing the tridentate ligand bppCOOH they obtained a complex with an energy barrier of 15.9 K and a relaxation time of 2.7 × 10^{-6} s [44]. This energy barrier is notably much lower than the activation barriers extracted from DC measurements (~2D) and ab initio calculations. The Orbach process involves transitions between real magnetic states, and no such levels exist below 150 cm^{-1}; consequently, relaxation does not occur via the Orbach process. Therefore, the relaxation time data were fitted to Eq. 4, which considers the direct and Raman processes. As shown in Figures 6 and S12, the fit is in perfect agreement with the experimental data for the following parameters: A = 5600(100) s^{-1}K^{-1}, C = 730(20) s^{-1}K^{-n}, and n = 3.25(2).

$$\tau^{-1} = AT + CT^n \quad (4)$$

A lower n exponent than the expected value for a Kramer ion (n = 9)

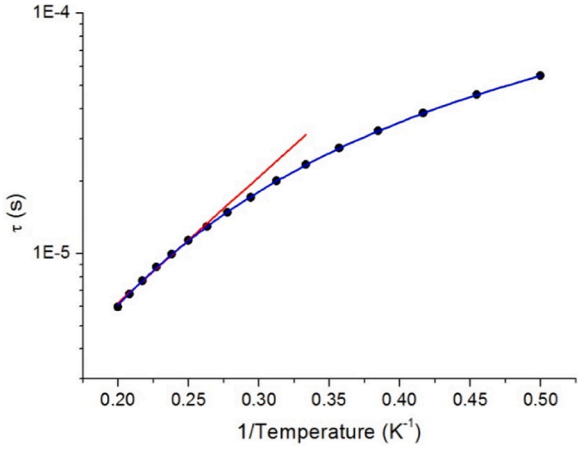

Fig. 6. Arrhenius plot for **1** at 2 kOe. The red solid line corresponds to the best fit from Arrhenius's law for the highest temperatures. The blue solid line corresponds to the best fit from Eq. 4.

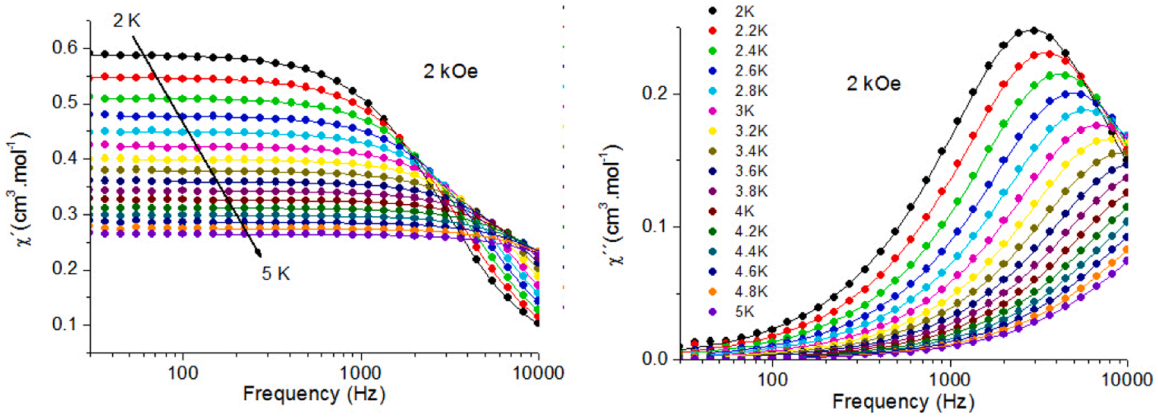

Fig. 5. Frequency dependence at different temperatures of the in-phase (a) and out-of-phase (b) ac magnetic susceptibilities for **1** under a static magnetic field of 2 kOe at different temperatures. The solid lines correspond to the best fit by an extended Debye model (see text).

[45] is commonly observed in octahedral cobalt-based compounds with SIM behavior, suggesting the contribution of acoustic and optical Raman processes in **1** [43,46–50].

3.6. EPR studies

X-band EPR spectroscopy was performed for complex **2** in the solid-state at room temperature (300 K). The *g* tensor reflects the local symmetry of the system. The sample gives two *g*-values (namely, $g_{\parallel} = 2.26$ and $g_{\perp} = 2.085$) in the axial spectrum. This value of *g* is typical for the $d_{x^2-y^2}$ orbital of the unpaired electron ground state and is associated with the N_2O_2 ligand set in the xy Cu^{2+} ion plane [51]. The region parallel to the spectrum exhibits signals due to hyperfine interactions, as shown in the inset of Fig. 7, between unpaired electrons and the Cu nucleus with a nuclear spin of 3/2. The hyperfine constant obtained by fitting using the easy spin MATLAB routine is 163.10^{-4} cm^{-1}. It is difficult to resolve the hyperfine interactions in the powder EPR spectrum, suggesting that the Cu^{2+} centers are isolated [52].

Additionally, the experimental EPR spectrum of complex **2** could be reproduced without considering any magnetic coupling constant (*J*). This is further evidence that the metal centers in both complexes are essentially isolated, as proposed by the small *J* obtained from the CASSCF calculations and magnetic susceptibility measurements.

4. Conclusion

We have successfully developed two new 1D coordination polymers with polycarboxylate coordinates in monodentate bridge mode with metal centers. Co^{2+} and Cu^{2+} are involved in distorted octahedral environments. Even though complexes 1 and 2 exhibit thermal stability, their surface area was not investigated due to the poor solvent loss. Complex 1 exhibits slow relaxation of the magnetization under a dc magnetic field with a large axial zero-field splitting parameter, $D = 74.7$ (3) cm^{-1} corroborated by magnetic susceptibility measurements and the CASSCF calculations. EPR measurements confirmed that the metal centers in both complexes are essentially isolated as suggested by the theoretical calculations and the magnetic susceptibility measurements. The production of other derivatives is in progress in our laboratory. New synthetic methodologies will be employed to synthesize highly porous magnetic materials.

CRediT authorship contribution statement

Henrique V.P. Hollauer: Writing – original draft, Methodology, Conceptualization. **Gabriel S. de Araújo:** Methodology, Conceptualization. **Guilherme P. Guedes:** Visualization, Investigation. **Henrique C.S. Junior:** Formal analysis. **Sonia Letichevsky:** Investigation. **Luis Ghivelder:** Investigation. **Stéphane Soriano:** Investigation. **Odivaldo Cambraia:** Investigation. **Lívia B.L. Escobar:** Supervision, Project administration, Writing – review & editing.

Declaration of competing interest

The authors declare the following financial interests/personal relationships which may be considered as potential competing interests: Guilherme P. Guedes, Sonia Letichevsky, Luis Ghivelder reports financial support was provided by Carlos Chagas Filho Foundation for Research Support of Rio de Janeiro State. Guilherme P. Guedes reports financial support was provided by National Council for Scientific and Technological Development. Livia B.L. Escobar reports financial support was provided by Pontifical Catholic University of Rio de Janeiro Department of Chemistry. If there are other authors, they declare that they have no known competing financial interests or personal relationships that could have appeared to influence the work reported in this paper.

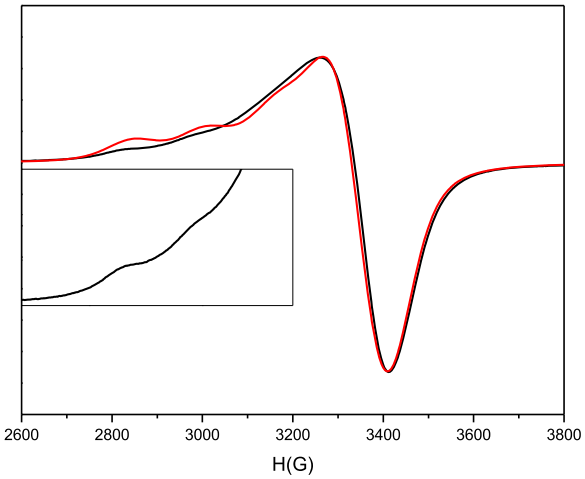

Fig. 7. Powder EPR spectra (in black) recorded in derivative mode at 9.39 GHz and $T = 300$ K for compound **2**. The calculated spectrum is shown as a red line.

Data availability

Data will be made available on request.

Acknowledgments

The authors thank the Brazilian agencies CNPq, CAPES, FAPERJ, and LDRX-UFF for the use of the laboratory facilities. This study was financed in part by the Coordenação de Aperfeiçoamento de Pessoal de Nível Superior - Brasil (CAPES/PNPD) - Finance Code 001. Lívia B. L. Escobar Thanks PUC-Rio for the Research productivity incentive grant. The authors are thankful for the financial support from Fundação Carlos Chagas de Amparo à Pesquisa do Estado do Rio de Janeiro-FAPERJ (project numbers E-26/202.720/2018 and E-26/201.314/2022) and Conselho Nacional de Desenvolvimento Científico e Tecnológico-CNPq (project number 304671/2020-7). DFT calculations were performed using the Lobo Carneiro supercomputer from Núcleo Avançado de Computação de Alto Desempenho (NACAD) under Project ID a20006 and the National Laboratory for Scientific Computing (LNCC/MCTI, Brazil) to provide HPC resources for the SDumont supercomputer, which contributed to the research results reported within this paper. URL: http://sdumont.lncc.br. Sonia Letichevsky thanks Faperj for grant E-26/010.000982/2019. We also thank Professor Nicolás Rey from Pontifícia Universidade Católica do Rio de Janeiro (PUC-Rio) for the thermogravimetric measurements.

Supplementary materials

Supplementary material associated with this article can be found, in the online version, at doi:10.1016/j.molstruc.2024.137811.

References

[1] D. Davarcı, C. Duyar, Y. Zorlu, 3D Ag(I) coordination polymer constructed from a flexible pyridyloxycyclotetraphoshazene linker: synthesis, crystal structure and dye adsorption properties, Polyhedron 231 (2023) 2–9, https://doi.org/10.1016/j.poly.2022.116250.

[2] M. Parsaei, K. Akhbari, J. White, Synthesis, characterization and comprehensive study of a 3D Co(II) coordination polymer antibacterial activity, J. Mol. Struct. (2023) 1283, https://doi.org/10.1016/j.molstruc.2023.135224.

[3] J.-Z.G. Xiu-Qi KANG, W.A.N.G. Jia-Hao, Syntheses, crystal structures, and catalytic properties of three zinc(II), nickel(II) and cobalt(II) coordination polymers constructed from 4, 4′-(pyridin-3, 5-diyl)dibenzoic acid, Chinese J. Inorg. Chem. 39 (2023) 2385–2392, https://doi.org/10.11862/CJIC.2023.190.

[4] F.F. Wu, Y.Q. Wu, Z.X. Wang, X. He, M.X. Li, Structural variation of hydroxide-metal clusters and three Co(II)/Zn(II) coordination polymers assembled by tripodal

3,5-bis(4-carboxybenzyloxy)benzoic acid, Inorg. Chem. Commun. (2022) 146, https://doi.org/10.1016/j.inoche.2022.110202.
[5] L. ling Liang, Y. qi Hu, J. she Zhao, Two uranium coordination polymers constructed by a polycarboxylic acid: structural variation, photoluminescent and photocatalysis properties, J. Solid State Chem. 282 (2020), https://doi.org/10.1016/j.jssc.2019.121085.
[6] Z.Q. Liu, Y. Zhao, Y. Deng, X. Du Zhang, Y.S. Kang, Q.Y. Lu, W.Y. Sun, Selectively sensing and adsorption properties of nickel(II) and cadmium(II) architectures with rigid 1H-imidazol-4-yl containing ligands and 1,3,5-tri(4-carboxyphenyl)benzene, Sensors Actuat. B 250 (2017) 179–188, https://doi.org/10.1016/j.snb.2017.04.151.
[7] D. Mal, R. Sen, P. Brandao, F. Shi, R.A.S. Ferreira, Z. Lin, Auxiliary ligand-assisted structural diversities of two coordination polymers with 2-hydroxyquinoline-4-carboxylic acid, Inorg. Chem. Commun. 40 (2014) 92–96, https://doi.org/10.1016/j.inoche.2013.11.038.
[8] A.A. Sapianik, M.A. Kiskin, K.A. Kovalenko, D.G. Samsonenko, D.N. Dybtsev, N. Audebrand, Y. Sun, V.P. Fedin, Rational synthesis and dimensionality tuning of MOFs from preorganized heterometallic molecular complexes, Dalt. Trans. 48 (2019) 3676–3686, https://doi.org/10.1039/C8DT05136D.
[9] H. Zhang, C. Lin, T. Sheng, S. Hu, C. Zhuo, R. Fu, Y. Wen, H. Li, S. Su, X. Wu, A luminescent metal-organic framework thermometer with intrinsic dual emission from organic lumophores, Chemistry 22 (2016) 4460–4468, https://doi.org/10.1002/chem.201504432.
[10] L. Wang, Z. Lu, C. Fan, Z. Zong, B. Zhu, C. Bi, X. Zhang, Y. Fan, One water-stable magnetic coordination polymer material (Fe3O4@PmPD-[Co-BT]) as an efficient adsorbent for rapid dye removal, New J. Chem. 44 (2020) 20626–20633, https://doi.org/10.1039/d0nj04646a.
[11] L. Liu, Y. Ran, M. Cao, X. Zhao, Y. Mu, Effect of solvent/auxiliary ligand on the structures of Cd(II) coordination polymers based on ligand 5-(2-benzothiazolyl) isophthalic acid, Polyhedron 199 (2021) 115103, https://doi.org/10.1016/j.poly.2021.115103.
[12] M.B. Coban, A new 3D HoIII-organic framework constructed from 1,3,5-tris(4-carboxyphenyl)benzene and 1,10-phenanthroline: crystal structure, morphological and solid state luminescence properties, J. Solid State Chem. 317 (2023) 123651, https://doi.org/10.1016/j.jssc.2022.123651.
[13] D. Shao, S.Y. She, L.F. Shen, X. Yang, Z. Tian, Field-induced single-ion magnet behavior in a hydrogen-bonded supramolecular cobalt(II) complex, Polyhedron (2022) 213, https://doi.org/10.1016/j.poly.2021.115614.
[14] M. Wakizaka, R. Ishikawa, H. Tanaka, S. Gupta, S. Takaishi, M. Yamashita, Creation of a field-induced Co(II) single-ion magnet by doping into a Zn(II) diamagnetic metal–organic framework, Small 19 (2023), https://doi.org/10.1002/smll.202301966.
[15] Bruker, APEX2, (2007).
[16] Bruker, S.A.I.N.T., (2013).
[17] G.M. Sheldrick, SADABS (1996).
[18] G.M. Sheldrick, SHELXL-97 A Program for Crystal Structure Refinement, 1997.
[19] L.J. Farrugia, ORTEP-3 for Windows - a version of ORTEP-III with a Graphical User Interface (GUI), J. Appl. Cryst. 30 (1997) 565.
[20] C.F. Macrae, I.J. Bruno, J.A. Chisholm, P.R. Edgington, P. McCabe, E. Pidcock, L. Rodriguez-Monge, R. Taylor, J. Van De Streek, P.A. Wood, Mercury CSD 2.0 - New features for the visualization and investigation of crystal structures, J. Appl. Crystallogr. 41 (2008) 466–470, https://doi.org/10.1107/S0021889807067908.
[21] L.R.K.R.T. Azuah, Y. Qiu, P.L.W. Tregenna-Piggott, C.M. Brown, J.R.D. Copley, R. M. Dimeo, DAVE: a comprehensive software suite for the reduction, visualization, and analysis of low energy neutron spectroscopic data, J. Res. Natl. Inst. Stan. Technol. 114 (2009) 341.
[22] S. Stoll, A. Schweiger, EasySpin, a comprehensive software package for spectral simulation and analysis in EPR, J. Magn. Reson. 178 (2006) 42–55, https://doi.org/10.1016/j.jmr.2005.08.013.
[23] F. Neese, The ORCA program system, Wiley Interdiscip. Rev. Comput. Mol. Sci. 2 (2012) 73–78, https://doi.org/10.1002/wcms.81.
[24] F. Neese, Software update: the ORCA program system, version 4.0, WIREs Comput. Mol. Sci. 8 (2018) e1327, https://doi.org/10.1002/wcms.1327.
[25] F. Neese, F. Wennmohs, U. Becker, C. Riplinger, The ORCA quantum chemistry program package, J. Chem. Phys. 152 (2020) 224108, https://doi.org/10.1063/5.0004608.
[26] S. Grimme, J.G. Brandenburg, C. Bannwarth, A. Hansen, Consistent structures and interactions by density functional theory with small atomic orbital basis sets, J. Chem. Phys. 143 (2015) 54107, https://doi.org/10.1063/1.4927476.
[27] J. Tao, J.P. Perdew, V.N. Staroverov, G.E. Scuseria, Climbing the density functional ladder: non-empirical meta-generalized gradient approximation designed for molecules and solids, Phys. Rev. Lett. 91 (2003) 146401, https://doi.org/10.1103/PhysRevLett.91.146401.
[28] F. Weigend, R. Ahlrichs, Balanced basis sets of split valence, triple zeta valence and quadruple zeta valence quality for H to Rn: design and assessment of accuracy, Phys. Chem. Chem. Phys. 7 (2005) 3297, https://doi.org/10.1039/b508541a.
[29] W. Heisenberg, Zur theorie des ferromagnetismus, Z. Phys. 49 (1928) 619–636, https://doi.org/10.1007/BF01328601.
[30] O. Kahn, Molecular Magnetism, VCH Publishers, Inc., Ney York, 1993.
[31] T. Soda, Y. Kitagawa, T. Onishi, Y. Takano, Y. Shigeta, H. Nagao, Y. Yoshioka, K. Yamaguchi, Ab initio computations of effective exchange integrals for H–H, H–He–H and Mn2O2 complex: comparison of broken-symmetry approaches, Chem. Phys. Lett. 319 (2000) 223–230, https://doi.org/10.1016/S0009-2614(00)00166-4.
[32] S. Grimme, L. Goerigk, R.F. Fink, Spin-component-scaled electron correlation methods, WIREs Comput. Mol. Sci. 2 (2012) 886–906, https://doi.org/10.1002/wcms.1110.
[33] B.O. Roos, P.R. Taylor, P.E.M. Siegbahn, P.E.M. Sigbahn, P.E.M. Si≐gbahn, A complete active space SCF method (CASSCF) using a density matrix formulated super-CI approach, Chem. Phys. 48 (1980) 157–173, https://doi.org/10.1016/0301-0104(80)80045-0.
[34] C. Angeli, R. Cimiraglia, S. Evangelisti, T. Leininger, J.P. Malrieu, Introduction of n-electron valence states for multireference perturbation theory, J. Chem. Phys. 114 (2001) 10252, https://doi.org/10.1063/1.1361246.
[35] H. Nakano, R. Uchiyama, K. Hirao, Quasi-degenerate perturbation theory with general multiconfiguration self-consistent field reference functions, J. Comput. Chem. 23 (2002) 1166–1175, https://doi.org/10.1002/jcc.10050.
[36] R. Maurice, R. Broer, N. Guihéry, C. de Graaf, Zero-field splitting in transition metal complexes: ab initio calculations, effective hamiltonians, model hamiltonians, and crystal-field models. Handbook of Relativistic Quantum Chemistry, Springer, Berlin Heidelberg, Berlin, Heidelberg, 2017, pp. 765–796.
[37] J.A. McCleverty, T.J. Meyer, Comprehensive Coordination Chemistry II, Elsevier Pergamon, 2004, https://doi.org/10.1016/C2009-1-28216-5.
[38] D.M.P. Mingos, P. (Peter) Day, J.P. Dahl, M. Atanasov, Molecular Electronic Structures of Transition Metal Complexes II, Springer, 2012.
[39] D. Llunell, M.; Casanova, D.; Cirera, J.; Alemany, P.; Alvarez, S.; Pinsky, M.;. Avnir, SHAPE: Program for the Stereochemical Analysis of Molecular Fragments by Means of Continuous Shape Measures and Associated Tools, (2013).
[40] F.J. Teixeira, L.S. Flores, T. Valverde, L.B.L. Escobar, M.S. Reis, C.C. Corrêa, Synthesis and magnetic properties of two cobalt-coordination polymers containing 1,10-phenanthroline and alkyl dicarboxylates ligands, J. Mol. Struct. 1261 (2022) 132820, https://doi.org/10.1016/j.molstruc.2022.132820.
[41] J. Titiš, R. Boča, Magnetostructural D correlations in hexacoordinated cobalt(II) complexes, Inorg. Chem. 50 (2011) 11838–11845, https://doi.org/10.1021/ic202108j.
[42] N.V. Reis, M.V. Marinho, T.R.G. Simões, K.C. Metz, R.C.A. Vaz, W.X.C. Oliveira, C. L.M. Pereira, W.P. Barros, C.B. Pinheiro, S.O.K. Giese, D.L. Hughes, K.R. Pirota, W. C. Nunes, H.O. Stumpf, Structural versatility driven by the flexible di(4-pyridyl) sulfide ligand: from cobalt(II) single-ion magnets to sheet-like copper(II) weak antiferromagnets, Polyhedron 171 (2019) 203–211, https://doi.org/10.1016/j.poly.2019.07.005.
[43] P.K. Sahu, R. Kharel, S. Shome, S. Goswami, S. Konar, Understanding the unceasing evolution of Co(II) based single-ion magnets, Coord. Chem. Rev. 475 (2023) 214871, https://doi.org/10.1016/j.ccr.2022.214871.
[44] V. García-López, F.J. Orts-Mula, M. Palacios-Corella, J.M. Clemente-Juan, M. Clemente-León, E. Coronado, Field-induced slow relaxation of magnetization in a mononuclear Co(II) complex of 2,6-bis(pyrazol-1-yl)pyridine functionalized with a carboxylic acid, Polyhedron 150 (2018) 54–60, https://doi.org/10.1016/j.poly.2018.05.006.
[45] A. Abragam, B. Bleaney, Electron Paramagnetic Resonance of Transition Ions, 1970. https://doi.org/10.1017/CBO9781107415324.004.
[46] L. Chen, J. Zhou, H.H. Cui, A.H. Yuan, Z. Wang, Y.Q. Zhang, Z.W. Ouyang, Y. Song, Slow magnetic relaxation influenced by change of symmetry from ideal: C i to D 3d in cobalt(II)-based single-ion magnets, Dalt. Trans. 47 (2018) 2506–2510, https://doi.org/10.1039/c7dt04651k.
[47] S. Roy, I. Oyarzabal, J. Vallejo, J. Cano, E. Colacio, A. Bauza, A. Frontera, A. M. Kirillov, M.G.B. Drew, S. Das, Two polymorphic forms of a six-coordinate mononuclear cobalt(II) complex with easy-plane anisotropy: structural features, theoretical calculations, and field-induced slow relaxation of the magnetization, Inorg. Chem. 55 (2016) 8502–8513, https://doi.org/10.1021/acs.inorgchem.6b01087.
[48] A. Landart-Gereka, M.M. Quesada-Moreno, I.F. Díaz-Ortega, H. Nojiri, M. Ozerov, J. Krzystek, M.A. Palacios, E. Colacio, Large easy-axis magnetic anisotropy in a series of trigonal prismatic mononuclear cobalt(ii) complexes with zero-field hidden single-molecule magnet behaviour: the important role of the distortion of the coordination sphere and intermolecular interactions, Inorg. Chem. Front. 9 (2022) 2810–2831, https://doi.org/10.1039/d2qi00275b.
[49] K.N.S.A. Singh, Optical-acoustic two-phonon relaxation in spin systems, Phys. Status Solidi 95 (1979) 273–277.
[50] K.N. Shrivastava, Theory of spin–lattice relaxation, Phys. Status Solidi 117 (1983) 437–458.
[51] K. Das, S. Goswami, B.B. Beyene, A.W. Yibeltal, E. Garribba, A. Frontera, A. Datta, EPR, DFT and electrochemical interpretation of a Cu(II) derivative incorporating a Schiff base precursor, Polyhedron 159 (2019) 323–329, https://doi.org/10.1016/j.poly.2018.11.058.
[52] R.P. Sharma, A. Saini, D. Monga, P. Venugopalan, J. Jezierska, A. Ozarowski, V. Ferretti, Influence of nitrogen donor ligands on the coordination modes of copper(II) 2-nitrobenzoate complexes: structures, DFT calculations and magnetic properties, New J. Chem. 38 (2014) 437–447, https://doi.org/10.1039/c3nj00736g.